Computational Fluid Dynamics Validation of Rooftop Wind Regime in Complex Urban Environment

by

Sarah Jamal Mattar

A thesis submitted in partial fulfillment of the requirements for the degree of

Master of Science

Department of Mechanical Engineering
University of Alberta

Abstract

This thesis presents a validation methodology for Computational Fluid Dynamics (CFD) assessments of rooftop wind regime in urban environments. A case study is carried out at the Donadeo Innovation Centre for Engineering (DICE) building at the University of Alberta campus. A numerical assessment of rooftop wind regime around buildings of the University of Alberta North campus has been performed by using 3D steady Reynolds-averaged Navier-Stokes equations, on a large-scale high-resolution grid using the ANSYS CFX. Four anemometers were set up on the roof of the DICE building and the computer software LabVIEW was used for data acquisition. Six months of data were collected and analyzed using different methods of data extraction and comparison. Four in-flow directions and three free-stream wind speeds were simulated, and the results of the assessment showed that the CFD simulation results are much more sensitive to upstream geometry modelling, when compared to downstream, even in cases of areas of low roughness lengths. A wind resource assessment was also conducted, and the effect of averaging period on the average wind power density and turbulence intensity was studied. It was found that changing averaging period does not influence the average wind power density, but the turbulence intensity decreased with decreasing averaging period.

Preface

The CFD model used in this thesis and described in Chapter 3 was created by Dr. Mireille T. Fogaing at the University of Alberta. The analysis in Chapter 4 and conclusions in Chapter 5 are my original work, as well as the literature review in Chapter 2.

Table of Contents

List of Tables

List of Figures

1. Introduction

Over the past 200 years, our world has grown drastically, and faster than anyone could have imagined. The Earth's population grew from less than one billion people in the 1800's, to over seven billion people today, and is expected to reach 9 billion by 2040 [1][2]. While this remarkable and rapid increase in our population has helped revolutionize our world – from modern medicine, advancements in science and technology to space exploration – the increase of people has created an increase in the demand of one crucial commodity to facilitate this revolution, and that is energy. In fact, the global energy demand is forecasted to increase by 25% from 2014 to 2040 [2].

The energy industry has been heavily reliant on fossil fuels over the past century, and though this has been highly beneficial to us, the world is now faced with a pair of dilemmas: depleting resources and climate change. As the demand continues to grow, the world is coming to terms with the need of cleaner resources as consequences that come with burning fossil fuels have become detrimental, such as increased greenhouse gas emissions, impacts on health and wildlife, and environmental pollution. Because of this, the global energy industry is shifting towards the use of renewable and sustainable fuels. To reinforce this move to cleaner energy sources, the Paris Climate Agreement was created by the United Nations Framework Convention on Climate Change (UNFCCC). The Paris Agreement's long-term goal is "Holding the increase in the global average temperature to well below 2°C above pre-industrial levels and pursuing efforts to limit the temperature increase to 1.5°C above pre-industrial levels, recognizing that this would significantly reduce the risks and impacts of climate change." The agreement was signed and came into effect in December 2015, with 195 countries pledging to reduce their carbon output as soon as possible [3].

In this fashion, many provincial governments in Canada have created policies to reinforce this switch to sustainable energy, by providing grants, rebates, and green energy incentives to micro-generators. Homeowners and small businesses that generate their own electricity through renewable sources, i.e., biomass, solar, wind, etc. can all connect to the provincial grids and feed any excess electricity they do not use and earn credits for future electricity consumption [4]–[7]. This has become an attractive selling point to many, and has encouraged small-scale renewable projects to be set up all over the country. In Alberta alone, the number of micro-generation sites has reached 3,794 by February 2019, and the installed capacity has grown over five fold in the past four years, reaching 48,738 kW [8].

While solar energy has been the main source of small-scale renewable energy generation, extensive research has gone into the development of many renewable resources, and a new focus in recent years has been

urban wind energy. Large scale wind power has gained popularity in the last few decades, since it is clean, renewable, and has minimal land impact as the turbines have a small footprint. Wind power is present today in more than 90 countries, with a total global installed capacity of 591 GW by the end of 2018 [9]. Canada specifically, is eighth in the world for installed capacity, at 13GW by the end of 2018, accounting for six percent of the country's electricity demand [4]. In fact, according to a study by Lu et al. [10], a network of land-based 2.5 MW turbines sited at 100 m hub height, restricted to non-forested, ice-free, non-urban areas and operating at as little as 20% of their rated capacity could supply 2,470 EJ, over 40 times the current worldwide consumption of electricity, and greater than 5 times the total global use of energy in all forms.

Urban wind power generation is still not as widespread, since urban wind power potential is difficult to assess. The urban landscape can cause wind concentration, and with the combination of buildings or other roughness elements, the wind is unevenly distributed geographically. The primary challenge for understanding the urban flow field is related to the turbulence, characterized by massive flow separation and recirculation due to the considerable directional variation of the wind around bluff bodies and roughness elements. These areas of high turbulence and recirculation cause the wind turbines which are mostly installed on the rooftops of buildings to experience multidirectional incident wind flow, which makes it difficult to capture these fluctuations and in turn, generate power. However, the concentration of wind flow through the narrow gaps within urban environments and with the combination of the building heights could potentially increase the wind power density by $3-8$ times compared to rural environments, surpassing the highest wind power standards from class 7 (> 800 W/m^2 at 50 m high) [11]. Because of these challenges, it is crucial to conduct accurate wind resource assessments in order to set the urban wind turbines in appropriate locations where optimized local wind speed increases due to the flow around built obstacles. Wind resource assessments for urban environments could also be used for many other applications, such as building planning, ventilation and exhaust design, urban wind energy harvesting from small wind turbines, design and placement of solar modules and panels, and comfort of pedestrians around the buildings.

1.1 Motivation

With all this in mind, the University of Alberta's Energy Management and Sustainable Operations (ESMO) unit within Facilities and Operations (FO) created the *Envision: Intelligent Energy Reduction* program which consists of a 5-step program for energy and emission reduction and management [12]:

1. Energy Efficiency and Reduction by Design
2. Recommissioning and Retrofitting
3. Continuous System Optimization
4. Greening the Supply
5. Education and Behavior Change

As part of the Continuous System Optimization strategy, three technologies in particular are being explored for implementation: demand-based ventilation (DBV) laboratory control, occupancy-based space ventilation, and energy analytics. Labs consume significant amounts of energy, typically twice the amount of energy as an office/classroom space. DBV control technology is an integrated sensing, control, and optimization solution that reduces building energy and operating expenses while maintaining indoor environmental quality. The system continuously monitors and analyses the facility's air, then dynamically reduces air change rates when the air is clean, often the majority of the time, and raises the rates when pollutants are sensed to maintain indoor environmental quality [12]. A computational fluid dynamics (CFD) model and analysis of campus to understand the behavior and patterns of the wind flow around any target buildings, is crucial for the implementation of these applications, and gives insight into the required equipment improvements and recommissioning. This model can also be used to study the prospect of greening the supply, as a wind resource assessment could show potential hotspots for wind energy production, and ideal locations for solar panel installation.

In addition to heating, ventilation, and air conditioning (HVAC) efficiency, the constant revival and renewal of campus by renovating existing buildings and adding extensions, or by the addition of new towers, offices, and labs can change the air flow around the campus and trigger the appearance of recirculation zones and flow separation in areas that did not exist before. This can change the wind profile around the university campus, which can alter the quality of air that is being drawn into fresh air intakes, as there is a possibility that the exhaust air being expelled from a building is being rejected into zones of recirculation – preventing it from completely exiting the turbulent layer above the buildings. Identifying these areas, if any, allows for the proper adjustments and modifications of the HVAC design, to prevent this from happening.

While the motivation for urban wind assessment and modelling is plentiful, for the purposes of this thesis, the experimental measurement campaign was carried out to provide data and a framework for the validation of a CFD model of the University of Alberta North Campus. This model can be used for wind turbine location siting for urban wind power generation, improving efficiency of HVAC systems, building and urban planning, and improving design of building exhaust stacks for better dispersion, to name a few.

1.2 Thesis Overview

Chapter 2 provides the background information necessary for understanding the work contained in the primary results chapters. This includes discussions about boundary layer, turbulence, and computational fluid dynamics. A review of the relevant literature is also presented. Chapter 3 outlines the details of the experimental measurement campaign and the CFD model used in this study. A proposed validation framework is also presented. Chapter 4 analyzes the results of the CFD simulations and the measurement campaign and applies the proposed validation framework. Chapter 5 summarizes the present thesis and states its contributions. The thesis is concluded with a discussion about future work.

2. Background

2.1 Atmospheric Boundary Layer

There is great interest in urban wind power production since it would cut down on the transportation of energy costs – infrastructure, maintenance, etc. – but the fact of the matter is that because of the urban boundary layer, the concept of urban wind power production is good in theory, but still has a long way to go to become a competitive power production method. Because of the presence of heavily congested areas and the presence of densely populated areas with many buildings, the wind regime in urban settings is affected and altered in comparison to than that in open, rural areas. Understanding this urban wind regime is one of the main barriers and obstacles in the way of successful and profitable urban wind power production. To understand the urban wind regime, one must first study the atmospheric boundary layer, and assess the changes that are introduced with the introduction of urbanization such as, homes, offices, and high rise buildings.

The atmospheric boundary layer (ABL), also known as the planetary boundary layer, is the lower part of the troposphere, the region in which "weather" as we know it occurs, and the region of the atmosphere we live in, and by this, is the lowest layer of the atmosphere as a whole [13], [14]. A boundary layer (BL) is defined as the part of the troposphere that is directly influenced by the presence of the Earth's surface, and responds to surface forces (i.e. frictional drag, evaporation, heat transfer, etc.) with a timescale of an hour or less [15]. The ABL is the part of the troposphere that is influenced by contact with the planetary surface. The height of the ABL depends on the strength of the atmospheric mixing generated by the surface. Typically, its depth varies according to a diurnal and seasonal cycle. During the day, solar radiation generates strong thermal atmospheric mixing as a result of convection currents that extend the ABL up to $\sim 1-2$ km, while at night the cooling of the surface relative to the atmosphere causes a downward flux of heat, suppressing atmospheric mixing, and the ABL contracts to < 100 m. The same thermal processes contribute to a greater mean ABL depth during the summer compared to winter [16].

The ABL consists of three vertical layers. The lowermost layer, the roughness sublayer, is only a few millimeters thick and starts from the ground and extends to approximately ten times the roughness length. The roughness length, z_0, is a parameter used to characterize the surface roughness. The next layer is the surface layer (or Prandtl or constant flux layer), which can be up to 100 m deep, which is usually only about 10% of the whole ABL depth. In this layer, the turbulent vertical fluxes of momentum, heat and moisture deviate less than 10% from their surface values and are taken as constant, and where the influence of the

Coriolis force is negligible. The third and topmost layer is the Ekman layer, which usually takes up about 90% of the ABL [13], [14]. Here the Coriolis force is important and causes a change of the wind direction with height. The balance of the forces involved in this layer present the Coriolis force, pressure gradient force and the frictional forces. A graphical depiction of ABL is shown in Figure 2-1 below. An equilibrium between the pressure force and the frictional forces is usually observed in the surface layer, and an equilibrium between, pressure, friction and Coriolis forces is observed in the Ekman layer [13].

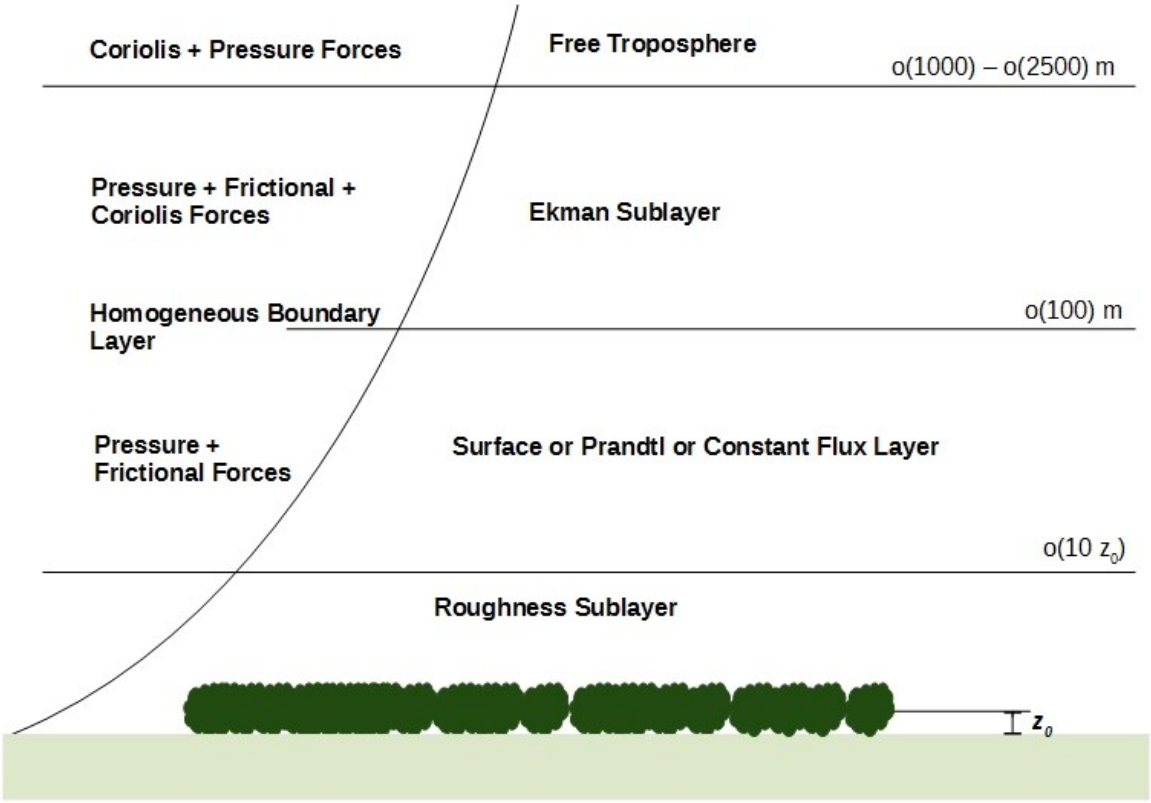

Figure 2-1: Atmospheric Boundary Layer. Adapted from [13].

2.2 Urban Boundary Layer

In the built environment however, the heights of the layers and the layers themselves are altered due to the presence of buildings and vegetation. A new sublayer within the ABL is introduced, called the urban boundary layer (UBL), existing in the surface layer. According to Emeis [13], urban surfaces are characterized by large roughness elements, wide-spread sealed areas, reduced moisture availability at the surface and increased possibilities for heat storage. This leads to higher turbulence intensities in the UBL and to stronger sensible heat fluxes from the urban surface into the UBL. Both these facts induce a greater depth of the boundary layer. The structure of the UBL is shown in Figure 2-2 below. The figure shows the

lower part is the urban canopy layer which extends from the ground to H, the average height of the buildings, followed by the wake layer where the wind flow is still affected by the presence of buildings. The extension of the wake layer is about two to five times the mean building height and, together with the urban canopy layer, they form the urban roughness sublayer within which complex vertical exchange induced by vertical motions can occur [13]. The atmospheric pressure differences upstream and downstream of the buildings, $p+$ and $p-$, respectively, are also shown in Figure 2-2.

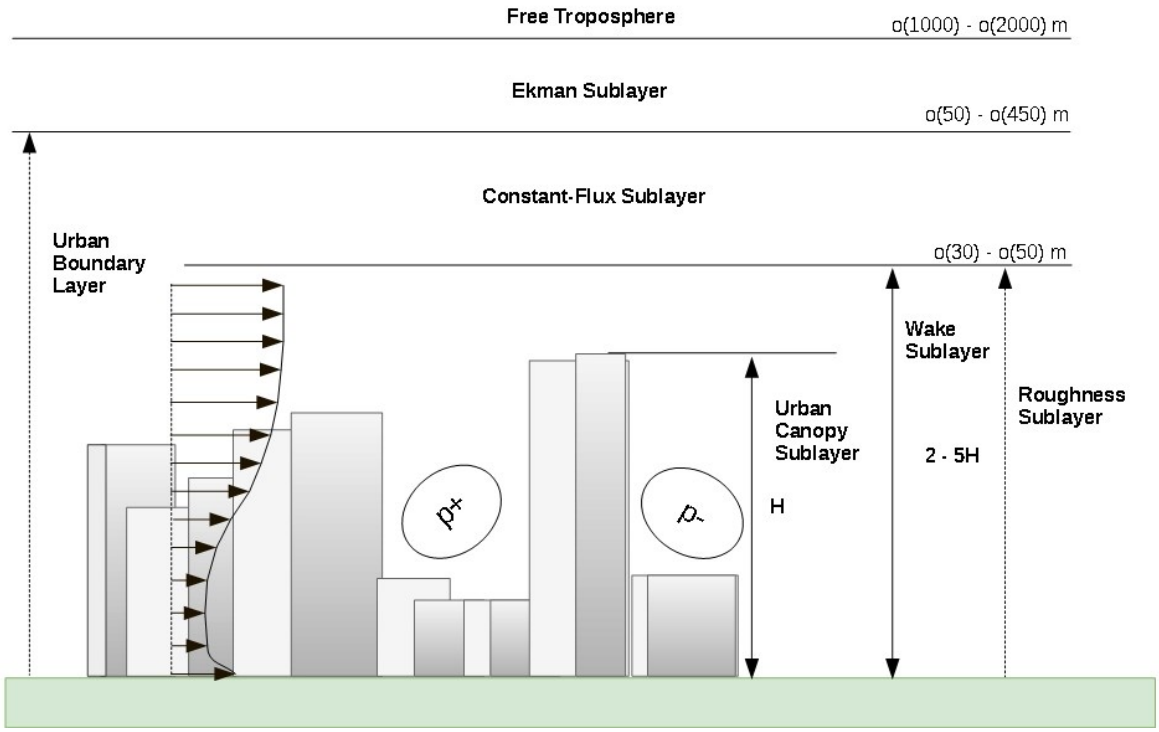

Figure 2-2: Modified Atmospheric Boundary Layer with Urban Boundary Layer. Adapted from [13].

The movement of the air and wind in the ABL occurs in both time and space. The spatial variations are dependent on the height above ground level and the local geographical conditions. The variations in time, however, are dependent on several different timescales. Diurnal variations of temperature near the ground are not evident at higher altitudes. These variations are one of the key characteristics of boundary layers over the ground. They are not caused by direct heating and forced mixing of the air in the boundary layer from solar radiation; instead, the ground absorbs this radiation – on the order of 90% absorptivity – and in turn warms up and cools down in response to the solar energy. This forces changes in the boundary layer [15]. The ABL can experience three types of boundary layer classifications in terms of temperature

distribution throughout the day: convective boundary layer or mixed layer (ML), residual layer (RL) and nocturnal or stable boundary layer (SBL).

A ML is characterized by intense mixing in a statically unstable situation where thermals, or large eddies, of warm air begin rising from the ground, which causes much of the turbulence in the boundary layer. The ML forms during the day about half an hour after sunrise, when the sun starts heating the ground. The heat stored in the ground is transmitted to the air it is in direct contact with. It results in a vertical motion of the air by natural convection. Frictional drag on the air flowing over the ground causes wind shears to develop, which contribute to the turbulence generation. The ML reaches its maximum depth in late afternoon [15].

The RL starts forming half an hour before sunset when the thermals are no longer formed, which allows the turbulence to decay. The RL is neutrally stratified, resulting in turbulence that is nearly of equal intensity in all directions. This resulting layer of air is sometimes called the residual layer because its initial mean state variables and concentration variables are the same as those of the recently-decayed mixed layer [15].

Throughout the night, the bottom portion of the RL is transformed into the SBL, which is characterized by statically stable air with weaker, sporadic turbulence [15]. Generally, winds near the ground are calmer at night and turbulence decreases. However, under certain conditions, air a bit farther from the ground can accelerate to form what is called nocturnal jet, which enhances wind shear and thus increasing turbulence at that level. This results in turbulence that occurs in short bursts and cause mixing throughout this layer.

Another side-effect of the built environment is urban heat islands (UHI). UHI are thermally-driven secondary circulations over cities. During the night, the surface loses the heat it had gained from solar radiation during the day to the atmosphere above. Once the surface has cooled, there is a downward flux of heat from the warm atmosphere above, causing the UBL to contract. When compared to their rural counterparts, urban landscapes are slow to warm during the day due to shading from building and high thermal mass of the materials present, and are slow to release the accumulated heat at night back into the atmosphere [16]. This slower cooling of the urban surface and the persisting upward heat fluxes at night prevent the formation of a stable nocturnal boundary layer [13].

2.3 Urban Boundary Layer Profile

Since the majority of small scale (or urban) wind turbines are installed on the roofs of buildings, the region of interest when studying the urban wind profile is the UBL. This is the only layer where the forces due to the turbulent viscosity of the air dominate [13]. Within this layer, vertical wind gradients are present; indicating that the wind speed is a function of height. The wind profile in this region is governed by the logarithmic law, shown in equation (2.1) below [17]:

$$u(z) = \frac{u_*}{\kappa}\, ln\left(\frac{z-d}{z_0}\right) \tag{2.1}$$

where u_* is the friction velocity, $u_* = \left[\overline{u'w'}^2 + \overline{v'w'}^2\right]^{\frac{1}{4}} = \sqrt{\frac{\tau_w}{\rho}}$, $u', v',$ and w' are the fluctuations of the East-West, North-South, and vertical wind components, respectively, τ_w is the wall stress, κ is von Karman's constant, $\kappa \approx 0.4$, z_0 is the roughness length, d is displacement height and $u(z)$ is the average wind speed at height z above ground [18].

The roughness length, z_0, is a parameter used to describe the roughness characteristics of the terrain. Table 2-1 below shows examples of roughness lengths for different terrain types. The displacement height, d, in the log law is to account for the 'zero-plane displacement.' Over the earth's surface, the ground experiences a 'no slip condition' due to the surface friction, and the velocity of the wind at the ground is effectively slowed to zero. This is the zero-plane. Theoretically, the wind speed at a height of z_0 should be zero. When flow passes over buildings, vegetation, or any other porous medium, the wind profile will be changed and shifted up, and the new zero-plane will be displaced to the top of the vegetation or other roughness elements altering the flow profile [14].

Table 2-1: Surface Roughness lengths for various terrain types. Source: Micallef et al. [19].

Terrain	Roughness Length (m)
Cities, forests	0.7
Suburbs, wooded countryside	0.3
Villages, countryside with trees	0.1
Open farmland, few trees and buildings	0.03
Flat grassy planes	0.01
Flat desert, rough seas	0.001

Alternative models have been recommended to account for the discrepancies in the application of the log-law in the built environment within the surface roughness layer.

MacDonald [20] defined a new exponential law for the wind speed below H, the height of the roughness elements, for buildings that are in an urban cube array and are sufficiently spaced out, shown in equation (2.2):

$$u(z) = U_H \exp\left[a\left(\frac{z}{H} - 1\right)\right] \tag{2.2}$$

Where U_H is the mean wind speed at height H, a is the attenuation coefficient, which depends on building morphology, and $a \approx 9.6\lambda_f$ for an array of cube shaped buildings. Here, λ_f is the frontal area density, which is the ratio of frontal area of each obstacle exposed to the wind and the underlying surface area of these obstacles.

Jiang et al. [21] expanded on MacDonald's exponential law and introduced a correction factor σ_h, to account for the variations in building heights:

$$u(z) = U_H \exp\left[a(1 - \sigma_h)\left(\frac{z}{H} - 1\right)\right] \tag{2.3}$$

And,

$$\sigma_h = \sqrt{\frac{1}{n}\sum_{i=1}^{n}\left(\frac{h_i - H}{H}\right)^2} \tag{2.4}$$

Where σ_h represents the degree of variation in building heights, n is the total number of buildings, h_i is the height of each building and H is the average height of the buildings.

This factor was introduced by studying the systematic influence of spacing, height and layout of the building arrays, without considering building shape. Three types of building arrays were simulated and studied: an array of identical cubes with varying λ_f, an array of cubes with varying heights, and a staggered array of identical cubes. It was found that MacDonald's exponential law was acceptable in the cases of varying staggering and varying λ_f, but could not accurately represent the flow with the case of varying building heights, and so introduced the factor σ_h, which takes into account these height differences.

Jian-Zhong et al. [22] studied equation (2.1) and proposed the introduction of a new wake factor, α, so that the impacts of the wake diffusion and interactions between the wake and the roughness elements can be analyzed separately. The modified log-law hence becomes:

$$u(z) = \frac{u_* \alpha}{\kappa} \, ln \left(\frac{z - d}{z_0} \right) \tag{2.5}$$

From a series of wind tunnel experiments carried out over uniform square arrays with different packing densities, this wake factor was shown to depend on λ_f, and is defined as follows:

$$\alpha = \begin{cases} 1.02 + 5.12\lambda_f, & \lambda_f < 0.07 \\ 1.45 - 1.39\lambda_f, & \lambda_f \geq 0.07 \end{cases} \tag{2.6}$$

The authors also defined an expression for the non-dimensional roughness height:

$$\frac{z_0}{H} = \left(1 - \frac{d}{H}\right) \exp\left[-\left(\frac{0.5\alpha^2}{\kappa^2} C_D \lambda_f \right) \right] \tag{2.7}$$

Where C_D is the coefficient of the drag caused by the obstacles.

2.4 Governing Equations of Fluid Flow

Fluid flow is governed by three fundamental conservation laws: conservation of mass, conservation of momentum and conservation of energy. They are the mathematical statements of three of the most important fundamental physical principles upon which all of fluid dynamics is based: mass is conserved, momentum is conserved ($F = ma$, Newton's second law), and energy is conserved.

These conservation laws contain thermodynamic variables, which, in turn, are governed by equations of state. In the context of this thesis, the flow will be assumed to be independent of temperature (i.e. no heat transfer) and incompressible, and as such, the energy equation as well as the equation of state will not be used. For the conservation of mass, the continuity equation is the governing equation that represents this physical principle. The continuity equation reads [15]:

$$\frac{\partial \rho}{\partial t} + \nabla \cdot (\rho \vec{u}) = 0 \tag{2.8}$$

The conservation of momentum (i.e. Newton's second law) is shown in the momentum equation below:

$$\frac{\partial u_i}{\partial t} + u_j \frac{\partial u_i}{\partial x_j} = -\delta_{i3} g - 2\varepsilon_{ijk} \Omega_j u_k - \frac{1}{\rho} \frac{\partial p}{\partial x_i} + \frac{1}{\rho} \frac{\partial \tau_{ij}}{\partial x_j} \tag{2.9}$$

Where u_i represents the fluid velocity in the three (i, j, k) Cartesian directions and x_i denotes these directions, ρ is the density, g is the gravitational constant (9.81 m/s), p the pressure, Ω is the angular velocity of the Earth's rotation (7.27×10^{-5} s^{-1}), and τ represents the viscous stresses on the fluid element.

There are certain assumptions that we can make to simplify the governing equations:

- Incompressible flow (density of air constant, $Ma < 0.3$)
- No Coriolis effects (target area is within the UBL, $Ek = 1.73 > 1$)
- Newtonian fluid (fluid is air, so viscosity is assumed constant and isotropic)
- Steady state (discussed in further detail in section 3.2)

The equations then simplify to:

$$\frac{\partial u_i}{\partial x_i} = 0 \tag{2.10}$$

$$u_j \frac{\partial u_i}{\partial x_j} = -\delta_{i3} g - \frac{1}{\rho}\frac{\partial p}{\partial x_i} + \nu \frac{\partial^2 u_i}{\partial x_j^2} \tag{2.11}$$

To ensure that the work in this thesis can be assumed to be independent of temperature, a measure of the ratio of the buoyancy production to the mechanical or shear production/loss term, called the Richardson number was calculated. This number measures the limit at which the mechanical turbulence is equal to the thermal turbulence, when the shear is the dominant force in the atmosphere. A simple form of the Richardson number, called the bulk Richardson number was used. The bulk Richardson number is defined as [13]:

$$Ri_b = \frac{g\Delta\Theta_v \Delta z}{\Theta_v[\Delta u^2 + \Delta v^2]} \tag{2.12}$$

Where Δz is a chosen height interval and $\Delta\Theta_v$ is the virtual potential temperature difference within this height interval, and Δu and Δv are the East-West and North-South velocity differences in the interval, respectively. The virtual potential temperature is the temperature that dry air must have to equal the density of moist air at the same pressure. This means that variations of virtual temperature can be studied in place of variations in density [15]. The virtual potential temperature is defined as:

$$\Theta_v = \Theta(1 + 0.609q) \tag{2.13}$$

Where q is the specific humidity, and Θ is the potential temperature, $\Theta = T\left(\frac{P_o}{P}\right)^{0.286}$, and P is air pressure, T is temperature, and P_o is a reference pressure usually set to 100 kPa.

Detailed calculations of the bulk Richardson number can be found in Appendix A.

2.5 Turbulence

To accurately assess the wind profile within the urban boundary layer (UBL), one must also understand the turbulent processes occurring within the boundary layer and the turbulent nature of the flow. From the previous section we can see that a large part of the structure of the UBL can be attributed to mixing of the flow and areas of recirculation. This mixing can be attributed to the turbulent nature of the boundary layer flow in an urban environment. Turbulence is so prevalent in our world and in our environment that according to Tennekes & Lumley, in fluid dynamics we are used to seeing with the naked eye, laminar flow is the exception and not the rule [23].

Despite its ubiquity, there is presently neither a precise definition of turbulence, nor a universal approach to the solution of turbulent problems. There are however, common characteristics that all turbulent flows exhibit that have been observed and classified. They are as follows [23]:

1. *Irregularity*

   Turbulent flows are stochastic. Stochastic fluctuations of the velocity field appear in both time and space. Two identical velocity fields cannot be reproduced or repeated even under exactly the same initial and boundary conditions. This means that a turbulent velocity field is unpredictable and a deterministic approach for its analysis cannot be employed. Instead, statistical methods are often relied on for ergodic systems (systems whose mean properties converge to a single value over long enough time). Statistical properties can be predictable, and are determined by the boundary and initial conditions.

2. *Large Reynolds Number*

   Turbulence exists if the Reynolds number is large enough, when inertial forces dominate over viscous forces. Turbulence often originates from the instabilities within laminar flows if the Reynolds number becomes sufficiently large. The instabilities are caused by the complex interactions between the viscous and the non-linear inertial aspects of the flow. The mathematical models available are insufficient to solve these interactions as they are so complex, and so all theoretical approaches to solve the turbulent problems are trial-and-error, and again we must rely on statistical methods.

3. *Diffusivity*

   Turbulent diffusivity (macroscopic transport independent of mean flow transport) causes rapid mixing and increases rates of momentum, heat, and mass transfer within the flow. The diffusivity of turbulence

is an important feature for the applications of turbulence, such as the prevention of boundary layer separation on airfoils at large angles of attack, and the resistance of flow in pipelines.

4. *Three-dimensional vorticity fluctuations*

Turbulence is rotational and three dimensional. It is characterized by high levels of fluctuating vorticity, and vorticity dynamics play an essential role in the description of turbulent flows, as this is the feature that distinguishes turbulence from other random two dimensional velocity fluctuations. Vortex stretching and rotation are important mechanisms in the maintenance of vorticity. They are inherently three dimensional (which can be demonstrated by the mathematics of the vorticity equation) and arise from the physics of vortex dynamics.

5. *Dissipation*

Turbulent flows are always dissipative. The turbulence energy cascade extracts kinetic energy from the mean flow and breaks it into turbulence kinetic energy, progressively dissipating this kinetic energy to the smallest scales of fluctuation where it is dissipated by viscosity; this cascade is orders of magnitude more effective at dissipating kinetic energy than is seen in steady laminar flows. This means that turbulence needs a continuous source of energy to make up for the losses from the mean flow; otherwise it will decay and die out. This distinction is important for comparing turbulent flows with random waves, such as acoustic noise. Although waves are dispersive, they are not dissipative, as they have no (or very minor) viscous losses. The vortex stretching and dissipation of turbulence gives rise to the existence of the energy cascade, which is the transfer of energy from large eddies to smaller nearby eddies.

6. *Turbulent flows are flows*

This is to state that turbulence is not a characteristic of the fluid itself, but a characteristic of the fluid flow. If the Reynolds number of a fluid flow is high enough, regardless of the molecular properties of the fluid, the flow will experience turbulence. The molecular properties and the initial and boundary conditions of the fluid flow will however affect the other characteristics of flow, such as the vorticity fluctuations and the rate of turbulent dissipation.

7. *Continuum*

The final characteristic of turbulence is that it is a continuum phenomenon, meaning that it is governed by the equations of fluid mechanics.

There are two main sources of turbulence in the atmosphere, thermal turbulence, and mechanical turbulence. Thermal turbulence is caused by the same mechanism that causes the expansion of the mixed layer, as discussed in the previous section. When the sun shines, it heats up different parts of the ground differently, which causes the hotter air to rise. This process of thermals, or eddies, both large and small, gaining altitude at an uneven rate is the thermal turbulence.

Mechanical turbulence is caused by the fact that the ground experiences strong shear since the velocity is almost zero near the ground, and increases as we get further away. This generates shear in the flow and the flow starts to 'tumble' over, which results in mechanical turbulence. These two different mechanisms produce the same outcome of turbulent flow, which can be analyzed in many ways.

2.5.1 Statistical Analysis of Turbulence

As mentioned earlier, there is no general approach to the solution of a turbulent problem [23]. The equations of motion that govern fluid flow have been greatly analyzed, but it is still difficult to make accurate quantitative predictions without relying on empirical data. There are several statistical methods available for the analysis of turbulent flows, such as Reynolds averaging, which is used in this study (discussed in section 2.5.2. However, this often leads to an issue known as the 'closure problem' of turbulence theory. Statistical studies of the equations of motion usually leads to situations where the number of unknowns is greater than the number of equations, and the researcher is often required to make assumptions to make the two equal. To achieve the required closure, more equations must be introduced so that there are a sufficient number of equations for all the unknowns. The equations that are used to close the system are defined by the turbulence model that was used. This will be discussed in further detail in section 3.2. There are a number of statistical parameters that can be used to characterize the wind for resource assessments. A summary of these parameters can be found in Table 2-2.

Table 2-2: Statistical parameters used for the characterization of wind. Source: Emeis [13].

Parameter	Description
Mean wind speed	Indicates the overall wind potential at a given site, expected wind speed for a given time interval (first central moment)
Wind speed fluctuation	Deviation of the momentary wind speed from the mean wind speed for a given time interval
Variance	Indicates the mean amplitude of temporal or spatial wind fluctuations, expected fluctuation in a given time interval (second central moment)
Standard deviation	Indicates the mean amplitude of temporal or spatial wind fluctuations (square root of the variance)
Turbulence intensity	Standard deviation normalized by a mean wind speed
Probability density function (PDF)	Indicates the probability with which the occurrence a certain wind speed or wind speed fluctuation can be expected

2.5.1.1 Time series decomposition of velocity

Wind fluctuates randomly in magnitude and direction; and the longitudinal component can be decomposed as shown in equation (2.14) below:

$$u(t) = \bar{u} + u'(t) \tag{2.14}$$

Where $\bar{u}$ is the mean value of the wind over an average time, and $u'(t)$ is its fluctuation around the average. The same decomposition applies to the lateral and vertical components of the wind, $v(t)$ and $w(t)$, respectively. This way of splitting the time series is called the Reynolds decomposition [14].

Ideally, the velocity can be recorded continuously and the mean can be evaluated through integration. However, in practice, the measured velocity records are a series of discrete points, u_i. The Reynolds decomposition of the velocity becomes:

$$u_i = \bar{u} + u_i' \tag{2.15}$$

An overbar is used to denote a time average over the time interval, t to $t + T$, where T, is much longer than any turbulence time scale, but much shorter than the time-scale for mean flow unsteadiness, e.g. wave or tidal fluctuation. According to Versteeg [24], T should approach infinity for the principle of Reynolds decomposition to be valid, but considering T larger than the time scale of the slowest variation of the considered flow system is satisfactory. This definition of the mean of a flow property is adequate for steady mean flows. However, for time-dependent flows the mean of a property at time *t* is taken to be the average of the instantaneous values of the property over a large number of repeated identical experiments: the so-called 'ensemble average', which is the ergodic hypothesis [24].

All fluctuating components have a zero mean over each averaging period, while within this period these fluctuating components can have important effects on the flow.

2.5.1.2 Variance, Standard Deviation and Turbulence Intensity

One statistical measure of the dispersion of data about the mean is the variance, σ^2, defined by:

$$\sigma^2 = \frac{1}{N}\sum_{i=1}^{N}(u_i - \bar{u})^2 \tag{2.16}$$

Where *N* is the number of data points. The standard deviation is defined as the square root of the variance, σ, which is also a measure of the strength of the turbulence, u_{rms}.

A frequently used variable to characterize turbulence in the wind is turbulence intensity. Turbulence intensity is defined as the normalization of the standard deviation with the characteristic mean wind speed over a time period, T [13]. It is defined as:

$$I_u = \frac{u_{rms}}{U} = \frac{\sigma}{U} \tag{2.17}$$

The same applies for the turbulence intensity of the other components of the wind speed, I_v and I_w.

The sampling period, T, should be sufficiently large that any increase would not alter the value of I. The most frequently used averaging period in wind engineering is 10 min, while classical boundary layer meteorology most often uses 30 min [13]. An example of a typical turbulence intensity plot is given in Figure 2-3.

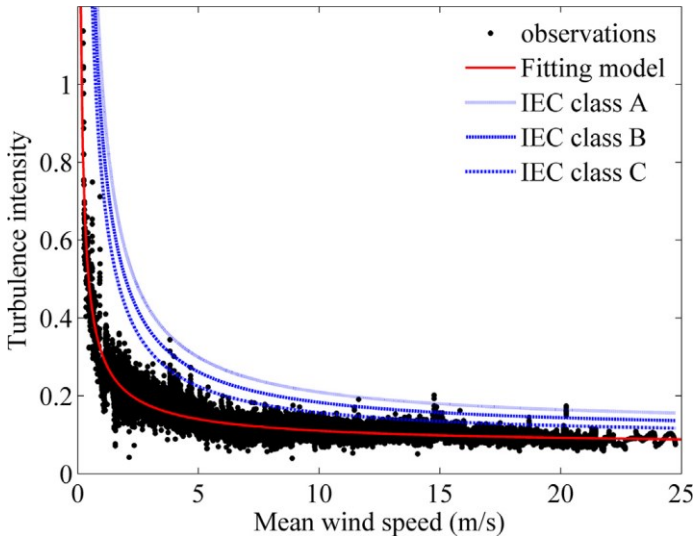

Figure 2-3: Example of TI vs. mean wind speed plot. Taken with permission from Ren et al. [25].

2.5.1.3 Probability Density Function

Probability density functions (PDFs) can indicate the probability with which the occurrence a certain wind speed or wind speed fluctuation can be expected. This is especially useful when characterizing a site for potential wind power production.

For instance, to determine the average power output from any turbine and to undertake load analysis, it is necessary to know the probability of the wind speed. Probability distribution is a technique which determines the probability of each data point in the data set. This probability can be viewed as either the

PDF, $p(u)$, which measures the occurrence of a particular wind speed or the cumulative probability, $C(u)$, which gives the probability that the wind speed is less than u [13], [26].

The PDF and the cumulative probability are related by:

$$\frac{dC}{du} = p \tag{2.18}$$

There are two commonly used probability distribution functions for wind energy applications; the Weibull and Rayleigh distributions. Weibull probability distribution is governed by two parameters, the scale factor, λ (proportional to the mean wind speed of the whole time series), and form factor, k, also called the shape factor, which describes the shape of the distribution [26]. The cumulative probability of the Weibull distribution is described by the following equation:

$$C(u) = 1 - \exp\left[-\left(\frac{u}{\lambda}\right)^k\right] \tag{2.19}$$

The respective PDF is then found by taking the derivative of cumulative probability with respect to u, and is given by:

$$p(u) = \left(\frac{k}{\lambda}\right)\left(\frac{u}{\lambda}\right)^{k-1} \exp\left[-\left(\frac{u}{\lambda}\right)^k\right] \tag{2.20}$$

Where u is wind speed, k is the shape factor, and λ is the scale factor (in $\mathrm{m/s}$).

When the shape factor, $k = 2$, we get a special case of the Weibull distribution, called the Rayleigh distribution. This distribution is commonly used for approximating the wind speed probability distribution. Figure 2-4 shows the effects of changing the scale parameter and the shape parameter on the Weibull distribution.

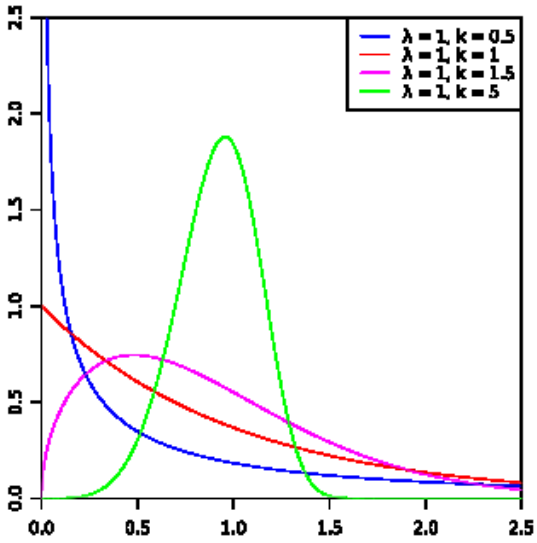

Figure 2-4: Weibull distributions with different scale and shape parameters. Source: [27].

2.5.2 Reynolds-Averaged Navier-Stokes (RANS) Equations

As we are interested in the mean behavior of the flow, equations (2.10) and (2.11) will be rewritten in their time-averaged form using Reynolds decomposition. This considerably simplifies the algebra involved without detracting from the main messages. The equations become [24]:

$$\frac{\partial \bar{u}_i}{\partial x_i} = 0 \tag{2.21}$$

$$\bar{u}_j \frac{\partial \bar{u}_i}{\partial x_j} = -\delta_{i3} g - \frac{1}{\rho}\frac{\partial \bar{p}}{\partial x_i} + \nu \frac{\partial^2 \bar{u}_i}{\partial x_j^2} - \frac{\partial \overline{u_i' u_j'}}{\partial x_j} \tag{2.22}$$

Note that the Reynolds averaging process introduced a new turbulent term in the momentum equation, called the Reynolds stresses. The bar over this term means that it is time-averaged. These terms are associated with convective momentum transfer due to turbulent eddies. The system of equations consisting of (2.21) and (2.22) involves more unknowns that the number of equations. This is the closure problem, touched on briefly in the previous section, and it can be tackled with the help of a turbulence model. Turbulence models help predict the Reynolds stresses and the scalar transport terms and close the system of mean flow equations [24]. A summary of the most common RANS turbulence models can be found in section 2.5.2.

2.6 Wind Power

The energy that is available in the wind is the kinetic energy of the moving air over the earth's surface [28]. To convert this energy into forms useful for us, like mechanical energy or electrical energy, this moving air must be decelerated, usually by a machine which converts this kinetic energy.

The kinetic energy in a stream of air of mass m, moving with velocity u, is defined as:

$$E = \frac{1}{2}mu^2 \tag{2.23}$$

If this volume of air was incident on a wind turbine with cross-sectional area A, the kinetic energy available for the turbine is:

$$E = \frac{1}{2}\rho_a V u^2 \tag{2.24}$$

Where ρ_a is the density of the air and V is the volume of the incident air.

This volume of air interacting with the rotor (or blades) of the wind turbine per unit time has a cross-sectional area equal to that of the rotor (A) and thickness equal to the wind velocity (u). Then, energy per unit time, or power, can be expressed as:

$$P = \frac{1}{2}\rho_a A u^3 \tag{2.25}$$

The wind power density (WPD), defined as the power of the wind per unit area, is a commonly used parameter in wind resource studies and is often used to classify locations in terms of their potential to harvest energy, ranging from Class 1 (very low WPD) to Class 7 (high WPD) [29]. The WPD can be expressed as [30]:

$$WPD = \frac{1}{2}\rho u^3 \tag{2.26}$$

From equations (2.25) and (2.26), we can see that the prominent deciding factor for the available power in the wind is its velocity. When the velocity is doubled, the available power increases by eight times, which means that for the same power output, the rotor area can be reduced by a factor of eight, if the wind turbine is placed at a site with twice the wind speed [28]. It is clear that proper site selection plays a massive role in the success of a wind power project. This highlights how critical the urban roughness is and why currently wind power is only commercially exploited in areas of low roughness.

2.7 Computational Fluid Dynamics (CFD)

Computational fluid dynamics (CFD) is the analysis of systems involving fluid flow, heat transfer and associated phenomena such as chemical reactions by means of computer-based simulation [24]. Some of the many advantages of CFD over experiment-based approaches to fluid systems design are:

- Substantial reduction of lead times and costs of new designs
- Ability to study systems where controlled experiments are difficult or impossible to perform
- Ability to study systems under hazardous conditions at and beyond their normal performance limits
- Practically unlimited level of detail of results

There are also several limitations and difficulties associated with CFD:

- Always an idealization of reality (geometric simplifications, assumptions for flow, boundary conditions etc.)
- Solutions are approximate
- Solutions are iterative, meaning errors could arise at each time step
- Turbulence can be modelled only with high degree of approximation
- CFD simulations require a great deal of computational power and time to solve

The costs of an experiment are roughly proportional to the number of data points and the number of experimental layouts tested, in terms of facility hire and/or person-hour costs [24]. CFD codes, however, can produce extremely large volumes of results at low added expense, and it is very cheap to perform parametric studies. CFD codes are structured around the numerical algorithms that can tackle fluid flow problems. In order to provide easy access to their solving power all commercial CFD packages include sophisticated user interfaces to input problem parameters and to examine the results. The process of carrying out a CFD simulation can be split into three stages and is as follows [24]:

1. Pre-processing

This stage consists of the modelling of a flow problem to a CFD problem to be processed by a CFD solver. The user activities at the pre-processing stage involve:

- Definition of the geometry of the region of interest: the computational domain
- Grid generation – the sub-division of the domain into a number of smaller, non-overlapping sub-domains: a grid (or mesh) of cells (or control volumes or elements)

- Definition of fluid properties and selection of boundary conditions that accurately represent the physical and chemical phenomena to be modelled

When the computational domain is defined, is it divided into cells that make up the mesh. The solution to the flow problem is defined at the nodes of each cell. The accuracy of the solution is dependent on the number of cells in the grid. Generally, the greater the number of cells, and in turn, the finer the grid, the more accurate the solution. However, the smaller the size of the grid, the more processing time and computing power is needed. It is thus up to the user for the construction of a suitable grid, which finds a reasonable compromise between the desired accuracy and the solution cost. An ideal mesh is usually non-uniform, i.e. finer in areas where large variations occur, and coarser in areas of relatively little change. The underlying physical phenomena are complex and non-linear so an iterative solution approach is required. ANSYS CFX, the CFD program used in this study, uses a Multigrid (MG) accelerated Incomplete Lower Upper (ILU) factorization technique for solving the discrete system of linearized equations. It is an iterative solver whereby the exact solution of the equations is approached during the course of several iterations [31].

2. Solver/Processing

Once a suitable grid has been constructed, it is imported to a solver. There are several numerical solution techniques: the finite difference method, the finite element method, the finite volume method and spectral methods. The ANSYS CFX solver, implements a hybrid finite element and finite volume approach for the solution of the governing equations. The numerical solution method consists of the following:

- Integration of the governing equations of fluid flow over all the (finite) control volumes of the domain
- Discretization – conversion of the resulting integral equations into a system of algebraic equations
- Solution of the algebraic equations by an iterative method

Integrating over the control volumes is a distinguishing feature of the finite volume method from all other CFD techniques. The result expresses the exact conservation of relevant properties within each cell. This correlation between the numerical method and the core physical conservation principle forms one of the main attractions of the finite volume method. Conservation of a general flow variable can be defined as the balance between all the processes within a control volume tending to increase or decrease it.

3. Post-processing

The final stage of a CFD simulation involves the visualization of the result using visualization and analysis tools that the CFD package is equipped with, such as:

- Domain geometry and grid display
- Vector plots
- Line and shaded contour plots
- 2D and 3D surface plots
- Particle tracking
- View manipulation (translation, rotation, scaling etc.)

The user's final goal of the simulation and requirements will dictate how the results should be analyzed or manipulated.

2.7.1 Modelling Turbulence

Turbulence in the flow causes the appearance of eddies with a wide range of length and time scales that interact in a dynamically complex way. A substantial amount of research effort is dedicated to the development of numerical methods to capture the important effects due to turbulence. The methods can be grouped into three categories [24]:

- Direct numerical simulation (DNS)

DNS methods compute the mean flow and all turbulent fluctuations. The full unsteady Navier-Stokes equations are solved on spatial grids fine enough to resolve the Kolmogorov length scale, at which energy dissipation takes place, and with time steps small enough to resolve the fastest fluctuations. This is the most computationally demanding method and so is not used for industrial flow computations.

- Large eddy simulation (LES)

LES is an intermediate form of turbulence calculations which resolves the behavior of the larger eddies. This method spatially filters the unsteady Navier-Stokes equations before solving, and passes the larger eddies and rejects the smaller eddies. While the computational demands for this method are large, due to the unsteady flow equations, this technique is more widely being applied for CFD problems with complex geometry [24].

- Reynolds Averaged Navier-Stokes (RANS)

This method focuses on the mean flow, and the effects of turbulence on the mean flow properties. The Navier-Stokes equations are first time averaged to exclude any effects from the turbulent fluctuations. This

averaging process introduces extra terms which are then modelled with classical turbulence models. The most common RANS turbulence models are classified on the basis of the number of additional transport equations that need to be solved along with the RANS flow equations and are presented in Table 2-3 below.

Table 2-3: Some common RANS turbulence models and the number of corresponding transport equations.

Number of Extra Transport Equations	**Model Name**
Zero	Mixing length model
One	Spalart–Allmaras model
Two	k–ε model
	k–ω model
	Algebraic stress model
Seven	Reynolds stress model

These models form the basis of standard turbulence calculation procedures in currently available commercial CFD codes. The RANS model provides reasonably accurate results while requiring modest computational power. A detailed review of the different turbulent models will not be done here, but more information about them can be found in Versteeg and Malalasekera [24].

While LES and DNS can provide higher accuracy results, they need much higher computational capabilities, and so the RANS approach is currently widely used for engineering flow calculations [24], and was used for this project.

The Menter Shear Stress Transport (SST) $k-\omega$ turbulence model was chosen in this study, because it was found to be the most accurate of six turbulence models when compared with wind tunnel measurements of the flow over a rectangular building [32]. The SST model was created because it was noted that the results of the $k-\varepsilon$ are much less sensitive to the arbitrary values in the free stream, but its performance is unsatisfactory for boundary layers with adverse pressure gradients. Menter then suggested a hybrid model using a transformation of the $k-\varepsilon$ into a $k-\omega$ model in the near-wall region and the standard $k-\varepsilon$ model in the fully turbulent region far from the wall.

The SST model uses the well-known Boussinesq approximation to deal with Reynolds stresses. This simplification assumes an analogy between the viscous term and the Reynolds stress term as follows:

$$\tau_{ij} = -\rho\overline{u_i'u_j'} = 2\mu_t S_{ij} - \frac{2}{3}\rho k\delta_{ij} = \mu_t\left(\frac{\partial \bar{u}_i}{\partial x_j} + \frac{\partial \bar{u}_j}{\partial x_i}\right) - \frac{2}{3}\rho k\delta_{ij} \tag{2.27}$$

Where k is the turbulent kinetic energy per unit mass, $k = \frac{1}{2}(\overline{u'^2} + \overline{v'^2} + \overline{w'^2})$, μ_t is the eddy viscosity, $\mu_t = \rho k/\omega$, and δ_{ij} is the Kronecker delta ($\delta_{ij} = 1$ if $i = j$ and $\delta_{ij} = 0$ if $i \neq j$).

The two equations presented by this model to close the problem are the transport equations for k and ω. The turbulent kinetic energy equation is:

$$\frac{\partial(\rho k)}{\partial t} + \frac{\partial(\rho k u_i)}{\partial x_i} = \frac{\partial}{\partial x_i}\left[\left(\mu + \frac{\mu_t}{\sigma_k}\right)\frac{\partial k}{\partial x_j}\right] + P_k - \beta^* \rho k \omega \tag{2.28}$$

Where P_k is the rate of production of turbulent kinetic energy, and is:

$$P_k = \left(2\mu_t S_{ij} \cdot S_{ij} - \frac{2}{3}\rho k \frac{\partial \bar{u}_i}{\partial x_j}\delta_{ij}\right) \tag{2.29}$$

And the equation for specific dissipation rate, ω, is:

$$\frac{\partial(\rho\omega)}{\partial t} + \frac{\partial(\rho\omega u_i)}{\partial x_i} = \frac{\partial}{\partial x_i}\left[\left(\mu + \frac{\mu_t}{\sigma_{\omega,1}}\right)\frac{\partial \omega}{\partial x_j}\right] + \gamma_2\left(2\rho S_{ij} \cdot S_{ij} - \frac{2}{3}\rho\omega\frac{\partial \bar{u}_i}{\partial x_j}\delta_{ij}\right) - \beta_2\rho\omega^2 + \frac{2\rho}{\sigma_{\omega,2}}\frac{\partial k}{\partial x_k}\frac{\partial \omega}{\partial x_k} \tag{2.30}$$

The model constants are as follows:

$\sigma_k = 1.0$, $\sigma_{\omega,1} = 2.0$, $\sigma_{\omega,2} = 1.17$, $\gamma_2 = 0.44$, $\beta^* = 0.09$, and $\beta_2 = 0.083$.

2.7.2 Discretization Methods

Finding an analytical solution to the Navier-Stokes equations is a difficult task partly due to the interdependence of the variables. In order to solve these equations, CFD codes must first break down each part of the modelled environment into many control volumes (CVs) and solve the discretized transport equations presented in the previous section in each CV. This is known as discretization. There are three discretization methods used by commercial CFD codes: the finite difference method (FDM), the finite element method (FEM), and the finite volume method (FVM). The discretization methods describe how the mathematical solution of the governing equations is applied, after the model has been converted from 3D geometry to a mathematical model. It is inherently linked to the mesh, which breaks down the geometry into CVs.

The ANSYS CFX code used in this study applies a hybrid finite element/finite volume discretization method. A comprehensive description of the mathematics involved in each discretization method is not

presented here as it is not required for the scope of this project. However, the main characteristics, advantages, and disadvantages of each method are outlined below.

Finite Difference Method

Characteristics:
- Domain discretization: domain is represented by a set of points. Results are obtained at those points.
- Equation discretization: begin with conservation equation in differential form. Algebraic approximation of the equation is obtained by substituting differential operators with finite differences.
- Applying the approximate equation to each point results in a system of algebraic equations.

Advantages:
- Most straightforward discretization process (in simple geometries).
- Easiest to code (in simple geometries).

Disadvantages:
- Doesn't handle curved boundaries and complex geometries well.
- Based on derivative approximation and, therefore, typically less accurate than FEM, FVM.

Finite Element Method

Characteristics:
- Domain discretization: domain is divided in a set of elements. Results are obtained at nodes on the corners or along the edges of the elements.
- Equation discretization: conservation equation is first expressed using the Method of Weighted Residuals, dependent variables are approximated by a series of interpolation polynomials (shape functions). Shape functions, multiplied by weight functions, are integrated over each element and these integrals are zeroed to make solution satisfy the governing equations.
- The small systems of equations obtained in each element are assembled into a large global system of algebraic equations.

Advantages:
- For linear PDEs, solution often can be proven mathematically to be exact at the nodes.
- Best for complex geometries and local grid refinement.
- Method of choice in solid mechanics.

Disadvantages:
- Usually less efficient than FDM, FVM in heat and flow simulations.
- Hard to interpret intermediate results physically after discretization.

Finite Volume Method

Characteristics:
- Domain discretization: domain is divided in a set of CVs. Results are obtained at the center of each CV.
- Equation discretization: begin with conservation equation in integral form. Algebraic approximation of the equation is obtained by using linear interpolation functions. These functions are integrated over each CV, producing a balance of fluxes in and out of the CV.
- The approximate balance (conservation) equations in each CV result in a system of algebraic equations.

Advantages:
- Terms in the discretized formulation have direct physical interpretation.
- Usually most efficient for heat and flow simulations.

Disadvantages:
- Only suitable for flux calculations (no solid mechanics).
- Doesn't converge as well as FEM for highly nonlinear problems.

2.7.3 Challenges with CFD Studies

As with any computer software, CFD solvers have their limitations. The results of a CFD code are only as good as their underlying physical and chemical models, and the skill set of the user. When setting up and analyzing any CFD simulation, there are many decisions that must be made by the user, like how many dimensions a problem should be modeled in, whether the flow is time dependent, whether or not to exclude pressure variations, etc. Incorrect decisions will lead to errors in the results. The two aspects that characterize a successful result are convergence and grid independence. The solution algorithm is iterative in nature, and in a converged solution the residuals, which are a measure of the overall conservation of the flow properties, are very small. While the true definition of an error is the difference between a measured or simulated value and the true value, there are well known CFD euphemisms for the word 'error', such as numerical errors, or numerical flow. Numerical errors, such as numerical or artificial diffusion is another limitation of CFD software that arises from the truncation error of the computer. Errors can also be introduced through the use of an inadequate grid. To eliminate errors due to coarseness of a grid, a grid dependence study must be performed, which is a procedure of successive refinement of an initially coarse grid until certain key results do not change. The simulation is then said to be grid independent [24].

2.8 Review of Relevant Literature

In order to validate the CFD model, a validation framework must be created. To create the framework, a review of existing best practice guidelines and CFD validation studies was first carried out.

Validation studies require high-quality full-scale or reduced-scale measurements, which should satisfy important quality criteria so experiments remain crucial for computational wind engineering [33]. Studies often utilize wind data from databases or weather stations for the validation data, despite the fact that these measurements are often not representative of the conditions being assessed due to their distance to the area of evaluation, and as such, there is a degree of error that is introduced with the extrapolation that is required [34]. The most accurate results are obtained by conducting both a measurement campaign at the target location under consideration, and running CFD simulations [35].

Blocken et al. [36] carried out a case study on the wind comfort of pedestrians in and around the Amsterdam ArenA. The upper deck of the arena experiences uncomfortable wind speeds and with the potential erection of new skyscrapers surrounding the arena, the effects of the variation in the wind concentration and speed were analyzed. This study used 3D steady RANS CFD simulations combined with the Dutch wind nuisance standard to assess the wind comfort of pedestrians around the football stadium before and after the addition of the high rise buildings. The results were compared with those found by a simplified procedure for the transformation of wind statistics to the building site. The study used a nearby meteorological station for wind data that is representative of the target location. Hourly wind speed data of the potential wind speed over the course of roughly 30 years were used and this statistical data were then transformed to a reference free-stream wind speed at the building site. Full scale wind speed measurements were taken at the arena for a three month period from four 3D ultrasonic anemometers on mobile posts at 20 locations on the deck. A reference free-stream wind speed measurement was taken by a 3D ultrasonic anemometer at the highest building next to the arena. All measurements were taken at 5 Hz and only values with sufficiently stable wind direction (i.e. invariant for at least an hour) were retained for validation. Validity of the model was determined by calculating the 'amplification factor' of the wind speed – the ratio between the measured wind speed at the anemometer locations on deck to the reference wind speed atop the highest tower, and compared to the corresponding amplification factor from the CFD validation. The measurements were grouped in intervals of $\pm 5°$ for each cardinal and inter-cardinal wind direction. The average standard deviation between the numerical and experimental amplification factors was 12% and the simulation was found to have a good agreement with the full scale measurements. The authors found that the wind comfort at the deck was slightly improved with the addition of new high-rise buildings. However, the wind comfort

at the streets and squares is significantly reduced near the new high-rise building tower and the stadium entrance.

Kalmikov et al. [37] conducted a case study to assess the wind power potential at the MIT campus and to determine the optimal location for wind turbine installation. For this study, two meteorological towers were installed at proposed turbine locations. The first tower was equipped with three 3-cup anemometers, each at 15, 20 and 26 m and with weather vane sensors at 15 and 20 m. The second tower was equipped with four 3-cup anemometers, two at 20 m and two at 34 m with a single vane sensor at each height. Both towers were equipped with ground-level temperature sensors. Data were collected as 10 minute averages and measurements were taken over the span of five and three months for the first and second towers, respectively. Three methods were used for data analysis, namely, direct statistical analysis, long-term normalization using advanced measure-correlate-predict methods, and computational fluid dynamics (CFD). The reference free-stream wind speed measurements were taken from a weather station situated on the highest building on campus, sufficiently elevated above the surrounding ground and building roughness. A method of climatology assimilation was used to allow the extension of resource assessment procedure from single measurement point into three dimensional space for the validation of the CFD model. The simulated results of the second tower were extrapolated and the extrapolated measurements for the first tower were compared with the data measured directly at that location. The ratios of mean wind speed and power densities between both sites were then determined for the measured data as 1.10 and 1.42, respectively, and as 1.11 and 1.35 for the simulated ratios between the assimilation point (tower 1) and the control point (tower 2) and the model was deemed to be valid.

Blocken et al. conducted another study on pedestrian wind comfort and safety with CFD and introduced a decision framework for this type of analysis [38]. The authors described three main cases for which wind comfort and wind safety studies are required. The complete framework can be found in [38]. The cases are as follows:

- Case 1: new developments within an existing urban configuration, for which on-site measurements are available or will be conducted;
- Case 2: new developments within an existing urban configuration, for which no on-site measurements are available or will be conducted;
- Case 3: development of a new urban configuration, for which – evidently – no on-site measurements are available during the design stage.

A case study was then conducted corresponding to Case 1 and a validation process was outlined, seen below in Figure 2-5.

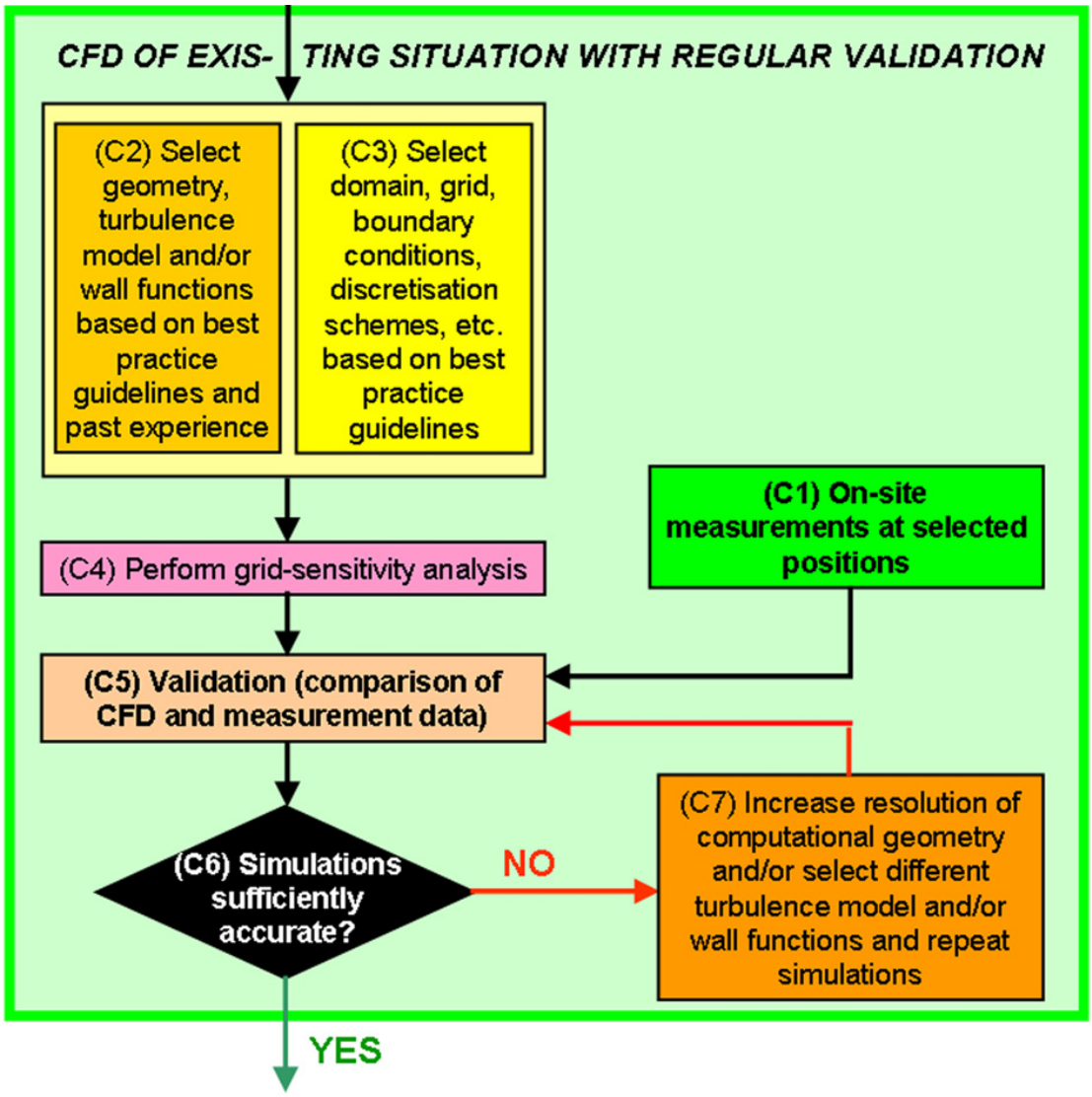

Figure 2-5: Flowchart illustrating the framework for CFD assessments and validation process. Taken with permission from Blocken et al. [38].

CFD simulations of the Eindhoven University campus were preformed using ANSYS FLUENT and solved the 3D steady RANS equations. On-site wind speed measurements were performed using three 3D ultrasonic anemometers on campus for six months. One of the three measurement locations was used as a reference free-stream in the study, and all measurements were taken frequency of at least 1 Hz, and were averaged over 10 minutes to provide values for mean wind speed, direction, and turbulence intensity. Only data within an interval of $\pm 5°$ were attributed to one of 12 wind directions ($0° - 330°$ in $30°$ increments). The measured mean wind speed values were converted to wind speed ratios by division by the measured reference wind speed and the simulated wind speed ratios are obtained by division of the simulated mean

wind speed by the simulated reference wind speed. The average deviations of the measurements were determined and they were found to be 25% and 11% for the two locations and were said to be fair and good agreements, respectively, and the overall average deviation between simulated and measured wind speed was 14% on average, which is considered a good agreement. The differences between the simulated and measured local wind directions for the two measurement locations for the 12 reference wind directions were found and the deviations were $21°$ and $22°$, which were considered good agreements. The study was performed in conjunction with the Dutch wind standard for wind comfort and safety which imposes a maximum allowed exceedance probability of the mean wind speed threshold depending on the intended use of the area in question. The exceedance probability was found by calculating a wind speed ratio from the CFD simulation at the reference height, converting the threshold wind at the pedestrian level the threshold at the reference height using the aerodynamic roughness length, and finally determining the percentage of time that the threshold value for the hourly mean wind speed at the reference height is exceeded.

Tabrizi et al. [39] studied the wind conditions of a rooftop of a tall building in order to gain insight and provide guidance in micro-siting wind turbines. A model using ANSYS CFX was created of the target location (a warehouse in Western Australia) and its surroundings and the simulation solved the 3D steady RANS equations and was carried out in conjunction with the wind resource assessment software WAsP, which used wind measurements from a meteorological station located $18\ \mathrm{km}$ away for roughly 6 months to generate a regional wind atlas for the 8 dominant wind directions, $200\ \mathrm{m}$ above the ground. A 3D ultrasonic anemometer was installed at the warehouse to collect wind data that were used for the validation of the simulations. The measurements were taken at $10\ \mathrm{Hz}$ for the same 6 month duration as the met station. A test case was first simulated of flow around a rectangular obstacle. The results were then compared against well-known CEDVAL wind tunnel datasets from Hamburg University. The simulation was then validated using a validation metric, a hit-rate. The validation metric hit rate, q, which is the ratio between the simulated and experimental values of interest, is calculated after achieving the numerical results available at all experimental measurement positions. A hit rate of $q \geq 0.66$, for all components of velocity was required to pass the validation test. The hit rates of the longitudinal, lateral, and vertical components of velocity were 73%, 82% and 79%, respectively, and the simulation was declared valid. The authors then simulated the model of the warehouse for the eight dominant wind directions and determined the differences between the experimental and numerical wind speeds for measurements considered neutrally stable and for the whole dataset, which they found to be at wind speeds greater than $4\ \mathrm{m/s}$. It was determined that the assumption of neutral stability in the CFX software does not significantly limit the software's capabilities and is a promising tool to predict wind speeds above rooftops of buildings in urban environments. The study found that the ideal location for the installation of a wind turbine is in the middle

of the roof of the warehouse, if it is placed on a sufficiently high mast to avoid the turbulent layer and instead it can capture the increased wind speeds from the slight inclination angle of the roof and the machine will likely experience less fatigue due to vertical loads and have a greater lifetime.

The authors continued their work and studied the effects of sampling rate and averaging period on turbulence measurements from the same monitoring system on the roof of a warehouse in Western Australia [40]. Two years of 10 Hz data were reduced to a representative 10 day dataset to decrease processing time and data storage and transfer. Tabrizi et al. then calculated the turbulence intensity and power spectral density from the representative dataset. The data were further filtered to produce multiple datasets for analysis. First, with three sampling rates: 1, 4 and 10 Hz, with an averaging period of 10 minutes, and second, with three averaging periods: 10, 5 and 1 min, sampled at 10 Hz. The effect of sampling periods appeared to be minor: only slight differences are found in the mean turbulence intensity for the wind components, with a maximum relative percentage difference equal to 4.34% observed between 10 and 1 Hz datasets (under slightly unstable conditions). In contrast, decreasing the averaging periods led to a decrease in the value of the calculated turbulence intensity. The authors reported a maximum relative percentage difference reduction from 29% to 22% of the longitudinal component of the mean turbulence, between 10 and 1 minute averaging periods.

Blocken et al. [41] conducted a case study which presents a CFD study with field measurement validation for natural complex terrain which consists of an irregular succession of hills and valleys surrounding a narrow entrance channel in Galicia, Spain. The aims of the study were the evaluation of the accuracy of steady 3D RANS simulations with a revised k–ε model for calculating mean wind-velocity patterns over this type of terrain, and to provide mean velocity data that can be used as input for real-time ship manoeuvring simulations to evaluate accessing the LNG terminal with larger LNG carriers. The study focuses on high wind speed conditions, for which the atmospheric boundary layer exhibits neutral stratification. The simulations are performed with 3D steady RANS and the realisable k–ε model for 12 wind directions. Measurements were taken using five 2D ultrasonic anemometers for four weeks. One anemometer was used as a reference free-stream measurement and all measurements were taken at a frequency of 1 min. The data were then averaged into 10-minute data. Two criteria were imposed on the experimental data for validation; the reference wind speed must be greater than 7 m/s to exclude thermal effects, and only data within a $\pm 5°$ interval were attributed to a given direction. Only wind directions that had more than 20 10-minute averaged data points were then used to determine mean values and corresponding standard deviations of wind speed and direction for validation. For validation of the CFD model, two wind speed ratios were defined: a wind speed ratio at the measurement positions divided by the reference wind speed, and the wind speed ratio at the height of the reference velocity measurements. The

numerical values were within $10-20\%$ of the experimental measurements, indicating a good agreement, and the same was the case for the simulated and measured wind directions. The numerical values showed deviations from the measurement values that are generally less than $30°$. The results showed that for wind directions $60°$ and $90°$, the funneling effect leads to an increase of wind speed in the channel compared to the wind speed over open sea. For the other wind directions, the topography led to a reduction of the wind speed in the channel, but also to strong wind speed gradients along the channel axis which greatly affects a ships' maneuverability. The study showed that the 3D steady RANS approach with the realizable $k-\varepsilon$ model can provide an accurate assessment of the complex mean wind-flow patterns and the funneling effect by the natural complex topography on the wind.

Dhunny et al. [42] compared the results from two computational fluid dynamics solvers, WindSim and OpenFOAM for the wind flow around the University of Mauritius campus for different wind directions. WindSim and OpenFOAM both solved the 3D steady RANS equations and were validated using on-site wind speed measurements from four cup anemometers setup around campus at different locations and different heights for a period of one year. The anemometers collected data at a rate of one measurement every $10\ \mathrm{s}$, and the data were averaged in 10 minute intervals and filtered for missing data, sensor malfunction, or other errors. The information for the CFD models such as reference wind speed, predominant wind direction, etc. was obtained from the closest available weather station and used for the simulations. Six different wind directions were analyzed and for validation, the velocity data were carefully assessed for selection of only data points where the atmospheric conditions were neutrally stratified. The data showed that the OpenFOAM results show a fair agreement and have a lower overall RMS error in comparison to the WindSim results. The differences in results were attributed to the differences in the meshing of the two solvers, as the gridding capabilities of WindSim are inferior to that generated in OpenFOAM.

Yan et al. [43] presented a framework for wind resource assessment which includes on-site measurement, CFD simulations and statistical analysis, shown in Figure 2-6.

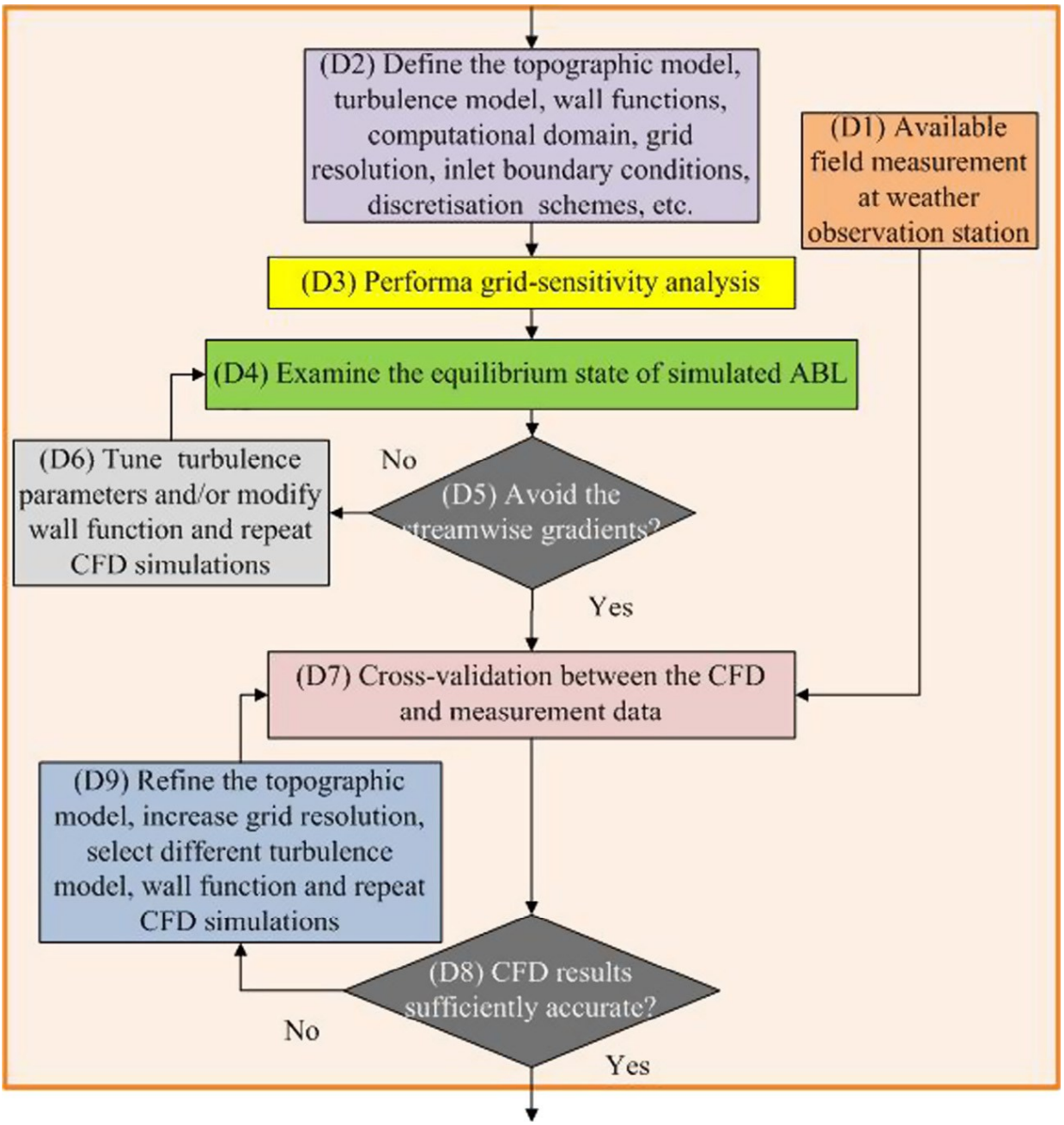

Figure 2-6: Validation methodology for CFD simulations. Taken with permission from Yan et al. [43].

The authors also presented a case study in which the framework was used. An island in Hong Kong with complex terrain was studied for potential wind power exploitation. One cup anemometer was measuring at a rate of one measurement per 1 min for six years. The measurements were divided into 16 wind directions, with groups of 22.5°. The measurements were used in conjunction with an ANSYS FLUENT model solving the 3D steady RANS equations using the RNG $k-\varepsilon$ turbulence model. Wind tunnel measurements were

also taken for the 16 wind directions of a topographic model of the island in a re-circulating wind tunnel with a sampling frequency of 2000 Hz. To validate the CFD model, a correction factors were created, the ratio of the wind velocity over standard terrain from wind atlas data and the velocity at the measurement site. A good agreement between the correction factors for the three measurement techniques was found, and the profiles of the mean wind speed in the wind tunnel tests were compared to and the CFD for different wind directions and the average deviation between measurements was found to be less than 8%, proving validity. The authors then conducted the wind potential assessment with statistical analysis. A Weibull distribution function, probability density function, and wind power density were calculated and it was determined the most attractive region for wind turbine installations are mainly around the crests of the mountains, where maximum and average wind energy densities of this area are $210\ \mathrm{W/m^2}$ and $93\ \mathrm{W/m^2}$, respectively.

Yang et al. [44] conducted a study at the National Taipei University of Technology campus in Taiwan to assess the distributions of power density and turbulence intensity with CFD software ANSYS FLUENT and field measurements to evaluate the wind resources available in a densely urbanized environment. The procedure followed in this study is presented in Figure 2-7. The climate data were obtained from a meteorological station using an anemometer and weather vane to measure the wind velocity and direction to generate data for a wind atlas specific to the region, and on-site measurements were obtained using four 3D ultrasonic anemometer and three thermal flow velocity probes to measure turbulence intensity levels. The equipment was used to monitor 10 points of interest on the target building on campus. These experimental results were then utilized to validate those generated by the CFD software to accurately assess the potential wind power and turbulence levels for suitable mounting sites of micro-turbines. The CFD model solved the steady 3D RANS equations using the realizable $k-\varepsilon$ turbulence model. The standard deviations of the velocity magnitude, wind direction and turbulence intensity varied between 0.05 and $0.84\ \mathrm{m/s}$, $1.7°$ and $16.8°$ and 0.03% and 0.92%, respectively. The wind power density was also used to assess the available wind power. It was found that the numerical velocities at the locations in the windward region agree well with the measured data, and the corresponding discrepancies are less than 10% while the velocities in the leeward region result in differences up to around 20%.

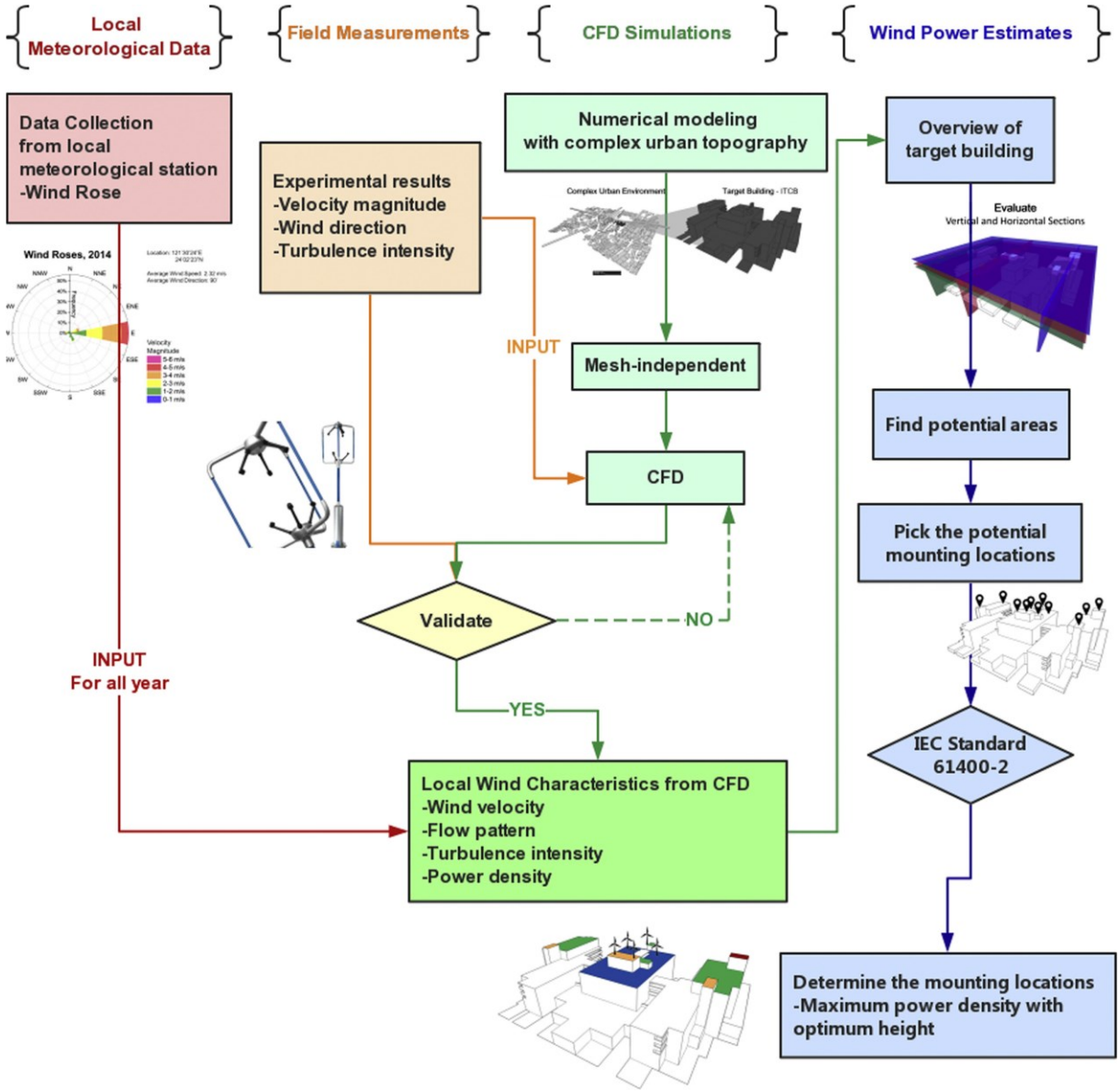

Figure 2-7: Wind resource assessment and validation technique. Taken with permission from Yang et al. [44].

Dhunny et al. [45] validated the average wind power estimated by the CFD software WindSim using on-site measurements from nine meteorological stations around a highly complex terrain at several heights. The authors modelled the island of Mauritius and conducted steady 3D RANS simulations using various turbulence models. Measurements around the island were taken at a frequency of three hours for two years. The authors used the method of hit rate (HR) for validation and found that the models were validated with a HR of above 88%, and concluded that the CDS scheme with the RNG $k-\varepsilon$ model using the fine mesh size yielded the highest HR and the least RMS error of 13.6. The study concluded that the wind power

potential of Mauritius is focused in the SE coast, lower central plateau and the SW regions and are viable for proper wind farming throughout the year, with wind power potentials of $1700 - 1900\ \mathrm{MWh/m^2/year}$, $1500 - 1800\ \mathrm{MWh/m^2/year}$, and $1900 - 2500\ \mathrm{MWh/m^2/year}$, all at 110 m, respectively.

Liu et al. [46] used data from a meteorological station to conduct a CFD study on the wind distribution in an urban configuration, namely, the Tianjin University campus in Tianjin, China. Two models of the campus were created, a detailed full-scale model, which encompassed the entire 10 km region between the meteorological station and the target building, and a simplified full-scale model, which had the same domain as the detailed model, but only the building structures in the urban configuration site concerned. The authors used ANSYS FLUENT to run their simulations, which solved the 3D RANS equations with a realizable $k - \varepsilon$ turbulence model. To validate the model, seven micro weather stations were set up on four buildings on the campus. Measurements were taken for 13 months at a frequency of one measurement per minute. The measurements were then averaged hourly for consistency and comparison with the met station. The average velocities over the area of interest in the detailed and simplified models were $1.28\ \mathrm{m/s}$ and $1.32\ \mathrm{m/s}$, respectively, which is a deviation of 5.5%. This difference implies that the roughness length imposed in the simplified model cannot fully capture the effects of the building structures. However, as the wind fields in the areas in captured by both models – i.e. the target building and its immediate surroundings – the authors concluded that the flow field inside the urban configuration was affected primarily by the surrounding building structures rather than the entire encompassing urban architecture. The simulated wind speeds and directions were then compared to the measurements. The hourly comparisons showed that average relative error for the numerical wind speed and the on-site measurements were 31.6% and 40.8% for the detailed and simplified models, respectively. The deviations in wind direction were 9.4% and 10.7% for the detailed and simplified, respectively. Although the deviations are large, the numerical wind speeds were within the actual variations of the measured wind speed, and the instability of the measured data could be accounted to the siting of the met stations within the recirculation zone, so the model was considered valid by the authors.

Wang et al. [47] performed a CFD study on the wind turbulence characteristics over a target building on the Inner Mongolia University of Technology campus in China to determine the installation height and location of roof mounting wind turbine, as a recommended practice for micrositing roof mounting wind turbines (RMWT) in urban environment, and the results are validated by wind LiDAR measurements. Results from this investigation suggest that the optimum installation height ranges from 1.51 to 1.79 times the height of building and the best locations are at the forefront where the wind acceleration reaches the maximum, as the wind direction varies. The CFD simulations were run on ANSYS FLUENT and the simulations solved the steady RANS equations with the realizable $k - \varepsilon$ turbulence model. The LiDAR

was setup on the target building to test the vertical wind profile, taking measurements at 10 heights from 10 m to 38 m. The LiDAR measured the horizontal wind velocity, horizontal wind speed standard deviation, wind direction, and turbulence intensity every 10 minutes for two weeks, and was used to validate the CFD. The authors used two wind directions to validate, 180° and 270°, and found that the numerical normalized velocity and turbulence intensity both agree with the observed measurements. They also used the method of hit rate (HR) for validation, and calculated HR's of 90% and 75% for the normalized velocity and turbulence intensity, respectively, which were both above the 66% required for validation. Wang et al. then created a RMWT micro-siting method, and found that the optimum installation height region is from $1.51H_A$ to $1.79H_A$, where H_A is the height of the building, and the best locations are at the forefront points in different wind directions.

Tang et al. [48] introduced a method for combining on-site measurements and CFD simulations for complex terrain site assessment. The method is a coupled approach to microscale wind resource assessment and was designed to reproduce the spatial variability distribution, as well as the dynamic wind velocity estimation of any desired positions within the concerned region. The procedure can be summarized in four main steps:

A. On-site measurement analysis: One year of data from masts are statistically analyzed, to obtain the velocity probability density distribution, the dominating wind direction, etc.
B. CFD simulation for complex terrain: High-resolution geographic information system (GIS) data for the complex terrain are used to run improved CFD simulations of wind flow with inflows from different directions.
C. Data fusion for wind resource assessment: On-site measurement data are compounded with implicit correlation information supplied by the CFD simulations. The measurement-CFD coupled dynamic velocity estimation (CFD-DVE) method is adopted to estimate the dynamic velocities at the desired position according to the CFD simulation and wind records of one single mast. Then, the CFD based weight refinement integration (CFD-WRI) method is adopted to integrate the velocity estimations from multiple masts from Mast 1 to Mast M (M is the number of masts).
D. Spatial and temporal information are calculated for any desired points within the wind farm. Wind energy distribution map and dynamic velocity estimation for desired positions are acquired.

A detailed description of the CFD-DVE and CFD-WRI methods can be found in [48]. A case study was carried out using this methodology at a proposed wind farm in Heibei province, China. The proposed farm has a complicated irregular shape with hilly terrain and spans across about 10 km (North-South) by 15 km (East-West), including a few hills with the largest elevation difference of 1270 m. Three wind meteorological masts were used to record one year of wind data. The data were sampled every 10 min and

was found to obey Weibull distributions with similar shape parameters and scale parameters. OpenFOAM was then used to run the steady RANS simulations of the proposed site for 24 different directions. Masts 1 and 3 were used for real-time estimation of the wind velocity at Mast 2 using both methods and the measurements from Mast 2 were used as validation for the estimates. The bias error (BE), the root-mean-square error (RMSE), the mean absolute error (MAE) and the standard deviation of the errors (STDE) of the estimations for the whole year were compared. It was found that the CFD-WRI method leads to smaller BE, RMSE, MAE and STDE in estimating the wind velocity magnitude, when compared to the inverse distance weighting (IDW) method found in literature. The annual wind energy distribution (AED) and annual wind energy production (AEP) were also assessed using both the proposed method and the IDW method. The estimated AED of each position is determined by hourly wind velocities estimated via the CFD-DVE method and integrated via the CFD-WRI method adopting the CFD simulations and the wind records from Mast 1 and Mast 3. Similarly, the estimated AEP is calculated. The relative errors were -2.84% and $+7.06\%$ for AED and AEP, respectively, when measurements at Mast 2 are taken as a validation of the CFD-WRI method. The authors' results show that a CFD-measurement coupled method has conducted dynamic velocity estimations at a desired position, with better statistical indicators than those from a single mast or the IDW method.

The high cost of wind measurement campaigns are an important barrier to the development of this subsector (urban wind) of wind energy [34]. One of the most important barriers for the study of wind in urban environments is the lack of adequate wind data measurements and CFD models are frequently used to fill this gap [34]. The main advantage of simulation studies compared to observational studies is the possibility to perform comparative analyses based on different scenarios [49]. The main drawback of simulation approaches, however, is the necessity of applying several simplifications, as the underlying physics of the urban microclimate is very complex. Therefore, careful validation of the simulations is very important [49].

3. Methodology

This section outlines the approach used for the validation of a CFD model of the University of Alberta North Campus. The proposed validation methodology, ANSYS CFX model creation, equipment, measurement campaign setup, and data processing are discussed.

3.1 Proposed CFD Validation Framework

While many of the studies presented in the previous chapter conduct validation and apply similar techniques, only a few outline and describe the validation process that took place. The hit-rate method has been used a few times in the presented studies, where a validation metric, q, is calculated after having all the results available at all measurement positions. The hit-rate is defined as:

$$q = \frac{1}{n}\sum_{i=1}^{n} N_i \tag{3.1}$$

and

$$N_i = \begin{cases} 1, & \frac{P_i - O_i}{O_i} \leq RD \text{ or } |P_i - O_i| \leq AD, \\ 0, & \text{elsewhere} \end{cases} \tag{3.2}$$

where n is the total number of points, O_i and P_i are measurement data and simulation data, respectively. RD and AD stand for a relative deviation and an absolute deviation, and these values are $RD = 0.25$ for all variables and $AD = 0.05$ for normalized velocities. A value of $q > 66\%$ is required for each quantity that has to be evaluated to pass the validation test.

Franke et al. [50] tested this validation metric, by assessing the validity of turbulent flow around five different geometries, and determining the hit rate for each velocity component, using the open source CFD software OpenFOAM. Three different grids were employed for each of the five test cases, and the influence of the boundary and numerical approximations of the convective and advective terms were tested. The authors found that the validation metric was not sensitive to these physical and numerical parameters, and that even an incorrect physical assumption could lead to successful validation, raising the question of whether the hit rate validation method is too robust to represent substantial changes in the simulation, and whether the criterion of $q \geq 0.66$ is too weak.

The framework presented by Blocken et al. [38], which was discussed earlier, and shown in Figure 2-5, gave an overview of the steps involved in running a CFD study, but did not offer any guidance on the best

method to assess the results of each step. The authors also state that “the definition of sufficiently accurate depends to some extent on the judgement and expectations of the modeller” [38], but offer no assistance on how to reach the decision of whether or not the simulation is accurate. As this validation technique is based on best practice guidelines, it was adapted and further expanded, to present a more detailed validation procedure and offer some insight on possible comparison methods for CFD and measured values.

The proposed validation framework is given in Figure 3-1.

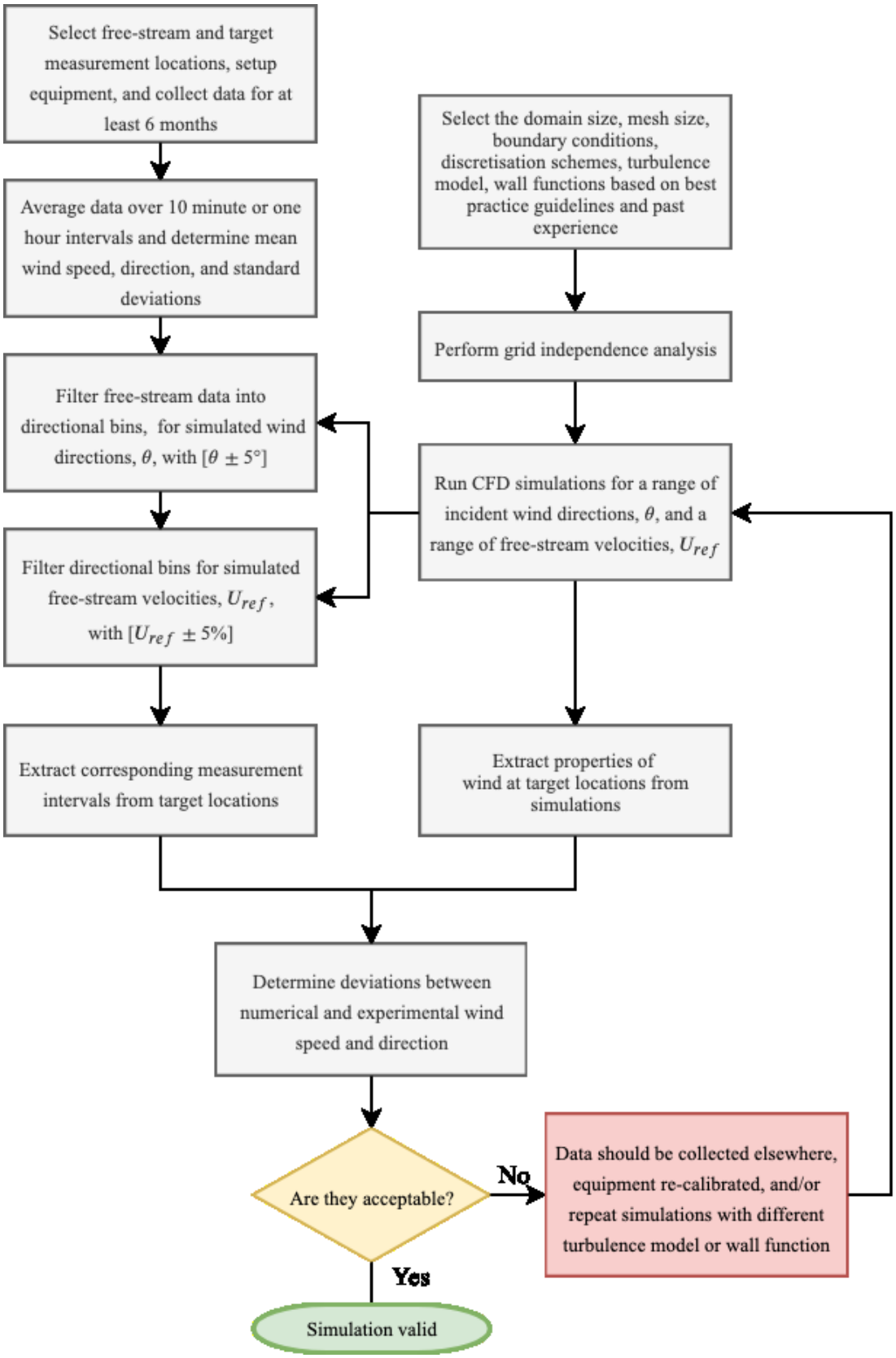

Figure 3-1: Proposed urban CFD validation methodology.

First, measurement locations should be chosen to accurately represent the CFD model. Free, unobstructed locations should be selected to ensure the most accurate data collection. Depending on the intended use of the CFD model, the locations should be chosen in areas of great interest, i.e., a proposed turbine location, pedestrian walkways, near air intakes/exhausts, etc. Measurement equipment should be set up and data should be collected for at least 6 months to ensure that there is some seasonal variability captured in the data set. The type of measurement devices used should depend on the type of analysis that is intended. If an in depth wind resource assessment is to be conducted, including turbulence measurements, an ultrasonic anemometer should be chosen to allow for fine temporal resolution, 15 Hz or better, otherwise, a vane or cup anemometer with lower temporal resolution, around 1 Hz or better, will be sufficient.

When all computational parameters, such as the geometry complexity and size, the choice of the turbulence model, type of wall functions, and boundary conditions are chosen, an initial simulation should be performed and a grid independence analysis conducted. The grid should be systematically coarsened or refined, and simulations on these new grids are performed. The results of each simulation are compared until there are no significant changes and grid independence has been reached. The most efficient grid is the coarsest one that still provides grid independent results. When grid independence has been reached, the simulations should be run for a range of different incident wind directions, θ, and a range of free stream velocities, U_{ref}.

When the data have been collected, they should be averaged over 10 minute intervals, and the mean direction and speed calculated, along with their standard deviations. The averaged free stream data should then be sorted into directional bins. The directional bins should correspond to the simulated incident wind directions, and should only allow measured wind directions in the range of $\theta \pm 5°$, to ensure accurate comparisons to the CFD. Each directional bin is then filtered, and data points are sorted by wind speed, filtering for the same simulated free stream velocities, within the allowable range $U_{ref} \pm 5\%$.

Once the free stream data have been filtered, the data from the measurement positions with the same date and time ID as the binned free stream data are filtered and placed in their corresponding bins. In other words, if in the free stream bin for North (0°) wind at $5\ \mathrm{m/s}$, there exists a data point for April 1st at 1 AM, the data points for this same date and time at all measurement locations should be filtered and placed into bins for the same wind conditions (North at $5\ \mathrm{m/s}$).

The simulated wind speed and direction at the same locations as the measurement equipment are then extracted from the CFD and the error between the simulated and measured data can be determined.

When deciding if the errors are acceptable, there are many parameters to take into consideration. The applications of the model, the allowable error for the given application (e.g. working threshold for equipment, tolerances, etc.), the most important parameter(s) (e.g. wind speed, direction, turbulence intensity, etc.), are all questions that the modeler must ask themselves, in order to come to a decision.

3.2 CFD Model

The CFD geometry and grid used in this study was created by Dr. Fogaing, a member of the research group. The work done on this model was presented previously [51]. The following section reviews the main aspects of the model creation and its features.

The commercial CFD code ANSYS CFX was used for the numerical modelling of the wind flow over the University of Alberta campus. The ANSYS CFX solver engine uses a parallel, implicitly coupled multigrid solver that is tuned for industrial CFD applications. The discretization of Navier-Stokes equations are based on a hybrid finite-element/finite volume approach, and the advection fluxes are evaluated using high-resolution scheme which is second-order accurate and bounded [51].

All the buildings in Figure 3-2 are modelled precisely, taking into account their geometric complexities for accurately modelling the wind flow over the campus. To generate the geometry, a free and open-source platform called 3D Warehouse, available via the 3D modelling computer program SketchUp [52], was utilized for its massive open source library of three-dimensional models.

Some accurate models of the University of Alberta Campus obtained by photogrammetry were already available on SketchUp [52], and were thus utilized to generate fast and accurate geometries for CFD analysis. These models were imported into SolidWorks and edited, such as the trimming of excessive dimensions which have negligible effect on the CFD analysis, like stair rails or window details. For the others buildings not available online, architectural plans from the University were necessary for the designs.

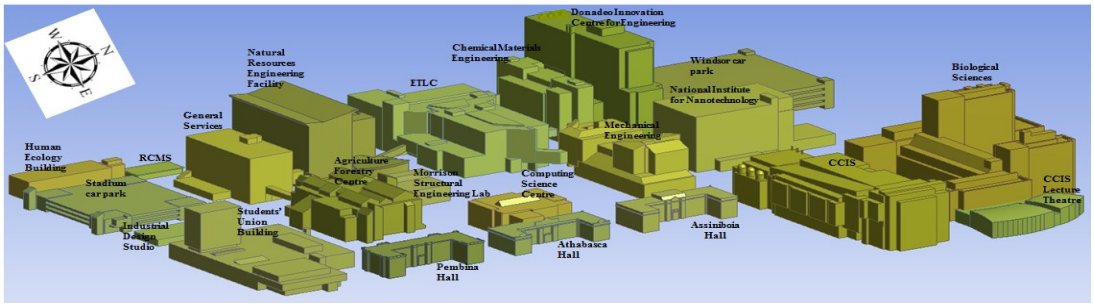

Figure 3-2: CAD model of the University of Alberta designed in SolidWorks.

The meshing was done using a combination of hexahedral elements to mesh simple regions, and the Delaunay meshing algorithm [53] which produced tetrahedral elements around buildings with complex shapes (Figure 3-3). Several prismatic layers were generated near the ground, the walls, and the roofs of buildings to capture boundary layers gradients. Smaller cells were used around small geometric details and in areas with high solution gradients (complex flow) [51].

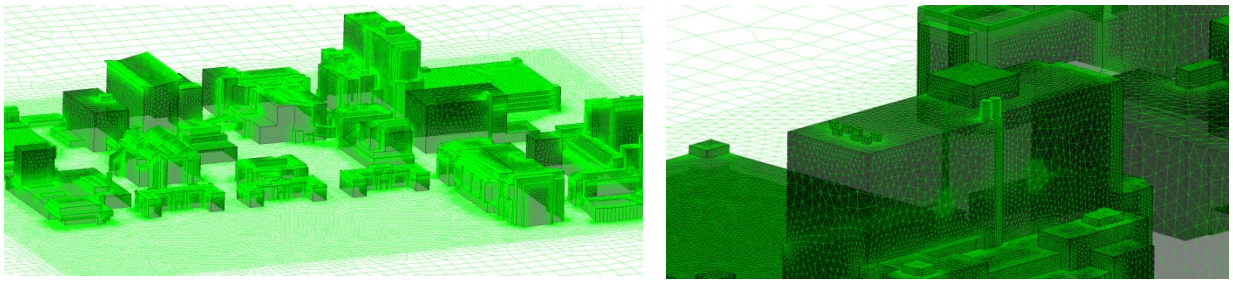

Figure 3-3: Plan view of the meshed geometry. A lower resolution was used in simple regions and a high resolution in the vicinity of buildings. Inflation layers near the ground, the walls and the roofs of buildings.

The simulated buildings were placed in a rectangular domain with a distance of $5H_{max}$ (where $H_{DICE} = H_{max}$, the height of the tallest building) between the building and: the inlet, the lateral sides and the top of the computational domain; and a distance of $15H_{max}$ from the building and the outlet.

The boundary conditions were defined at the limits of this rectangular domain. The mean logarithmic velocity profile (U) and the turbulence quantities profiles (turbulence kinetic energy, k, and its dissipation rate, ε) derived from the assumption of an equilibrium boundary layer by Richards and Hoxey [54] were computed at the inlet of the computational domain [51]:

$$U = \frac{u_\tau}{\kappa} \ln\left(\frac{z + z_0}{z_0}\right) \tag{3.3}$$

$$k = \frac{u_\tau^2}{\sqrt{C_\mu}} \tag{3.4}$$

$$\varepsilon = \frac{u_\tau^3}{\kappa(z + z_0)} \tag{3.5}$$

Where u_τ is the friction velocity associated with the logarithmic wind speed profile, z is the vertical displacement, and z_0 is the aerodynamic roughness length, κ is the von Karman constant, $\kappa = 0.412$, and C_μ is a model constant, $C_\mu = 0.09$.

The value of the aerodynamic roughness length ($z_0 = 1$ m) and a representative wind speed ($U_{ref} = 5.58$ m/s) at a reference height of 80 m were estimated via the Canadian Wind Atlas website, and were used to determine the friction velocity, u_τ. The Shear Stress Transport (SST) $k-\omega$, was chosen as the turbulence model because of its overall good performance for resolving wind flow around buildings [32]. This choice required converting the profile of ε to the specific dissipation rate ω using the relation: $\omega = \varepsilon/C_\mu k$. Therefore, the inflow profiles defined at the inlet of the computational domain were the wind speed, U, the turbulence kinetic energy, k, and the specific dissipation rate, ω.

At the outlet of the domain, zero relative pressure was imposed, while symmetry boundary conditions were applied at the top and the side faces of the computational domain. The roofs and the walls of all simulated buildings as well as the ground were set as no-slip walls and the automatic near-wall treatment method was deployed by ANSYS CFX. This allowed a gradual switch between wall functions and low-Reynolds number grids to treat the wall effects within the boundary layer regions [51].

The 3D steady RANS equations were computed in combination with the SST $k-\omega$ turbulence closure model. Steady simulations were run as they are less computationally expensive and require less time per simulation, compared to unsteady simulations. High resolution schemes are used for the advection and viscous terms, and turbulence parameters of the governing equations. The normalized residual target was set to 10^{-5}, as recommended by Franke et al. [55]. Three points upwind, one downwind of the domain, and one 1 m above DICE roof were monitored during each simulation. The convergence was reached when the normalized residuals of the momentum and the velocity profiles obtained in three different locations over the computational domain exhibited no remarkable fluctuations and remained steady during the iterative process [51].

A grid independence analysis was performed for ensuring that the simulated results were independent of the grid resolution. Three different grid sizes of 5,530,761 nodes (Mesh 1), 8,309,837 nodes (Mesh 2) and 11,020,616 nodes (Mesh 3) were analyzed and the results are shown in Figure 3-4. The wind was coming from the South and the normalized velocity profiles were taken along a vertical line above the roof, near the west edge of DICE building.

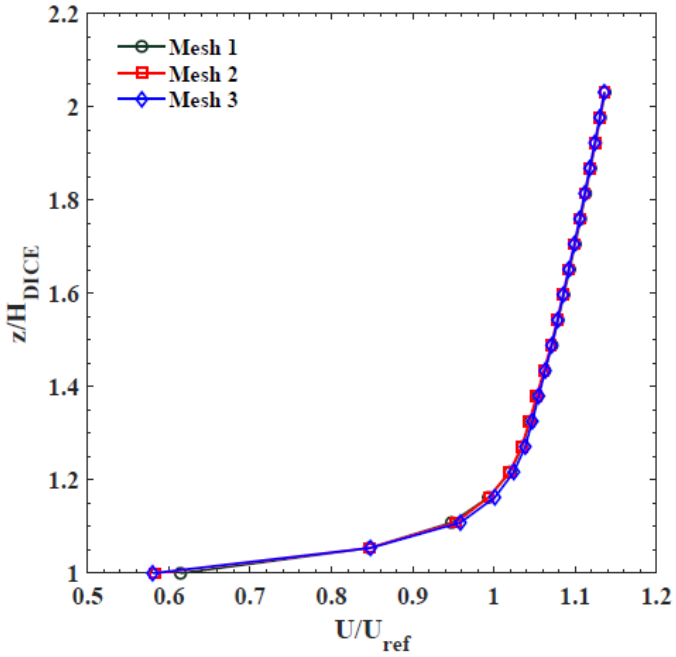

Figure 3-4: Normalized velocity profiles taken along a vertical line above DICE roof. Source: [51].

As there were no significant differences in the profiles of the normalized velocity along the vertical direction for the three grids, the intermediate grid (Mesh 2) was chosen as the optimum grid for the simulations over the campus [51].

3.3 Location and Equipment

Four anemometers were used to collect wind data: two R. M. Young Model 81000 3D ultrasonic anemometers (Figure 3-5a), ‘B’ and ‘D’, and two R. M. Young Model 09101 wind monitors (Figure 3-5b), ‘A’ and ‘E’. Detailed specifications of these are provided in Appendix B. The anemometers were setup around the roof of the target Donedeo Innovation Center for Engineering (DICE) (Figure 3-6), which is located in the University of Alberta North Campus and its dimensions are 63.7 m tall, 99.5 m long and 64.3 m wide. DICE is the tallest building in North Campus and has been chosen as the target building because of its height and suitable location. Note that a third wind monitor, ‘C’, was initially set up for data collection in addition to the four described above, but experienced software issues and was taken offline and not included in the measurement campaign.

(a) (b)

Figure 3-5: a) Young Model 81000 3D ultrasonic anemometer, b) Young Model 09101 wind monitors.

Figure 3-6: Locations of anemometers on the roof of the DICE building (not to scale). Note that dimensions are in m.

Ultrasonic anemometers measure the time it takes a signal of ultrasonic frequency to travel between two transducers. Electronic circuits inside measure the time it takes for the sound to make its journey from each transmitter to the corresponding receiver. Depending on how the wind blows, it will affect some of the signals more than the others, slowing it down or speeding it up very slightly. A sonic beam at a given frequency is directed toward a point O which consists of elements carried by the wind. The Doppler shift frequency received by these elements is re-radiated (scattered) and a new Doppler shift frequency is received at the receivers. The wind velocity is obtained by measuring the Doppler shift experienced between the frequency emitted by the source and that obtained at the receivers. The circuits measure the difference in speeds of the signals and use that to calculate air speed [56] The time depends on the distance between the transducers, the speed of sound and the air speed along the axis of the transducers [57]. They can operate

in most conditions experienced in the atmosphere, but heavy rain and ice buildup may affect the quality of the data [58].

Mechanical wind monitors measure two dimensional wind speed and direction. In the 09101 monitor, the wind speed sensor is a four blade propeller that turns a multipole magnet. The rotation induces a variable frequency signal in a stationary coil. The raw transducer signals are processed by onboard electronics; however a conventional calibrated voltage output can be selected and processed by an external board [59]. The specifications of both pieces of equipment are presented in Table 3-1 below.

Table 3-1: Anemometer specifications.

	Ultrasonic Anemometer	**Wind Monitor**
Wind speed range (m/s)	0 to 40	0 to 100
Accuracy (m/s)	± 0.05	± 0.03
Wind direction range (°)	0 – 359.9	0 - 360
Accuracy (°)	± 2	± 2
Threshold (m/s)	0.01	1
Output rate (Hz)	4 - 32	1 -10
Temperature range (°C)	-50 to 50	-50 to 50
Weight (kg)	1.7	1
Output format	Serial output RS-232 or RS-485 (selectable) or Voltage output	Serial output RS-485 or Voltage output

Several considerations went into the decision of equipment heights and locations. Through discussions with the Architectural Maintenance group and Facilities and Operations on campus, and Aegis West Engineering, a third party building science engineering services firm that was contracted to assess the safety of the project, it was decided that a maximum height of 15 ft was deemed safe, as it allowed us to purchase non-penetrating roof mounts (NPRMs), which do not need guywires and do not alter the integrity of the roof. Baird 15ft NPRMs were purchased (drawings and details of mounts can be found in Appendix B and concrete slabs were placed on the bases to provide extra stability (Figure 3-7).

(a) (b)

Figure 3-7: (a) Anemometer B set up on 15ft Baird NPRM, b) Concrete blocks added for extra stability.

As the masts purchased were stock pieces, adapters were required to fit the anemometers on to the masts. Both the mechanical and the ultrasonic anemometers mount onto a STD 1″ pipe (1.32″ OD), while the NPRMs have an upper mast of STD $1-1/2''$ pipe (1.9″ OD). Pipe reducers where then designed and secured onto the masts for safe anemometer mounting. The reducers were machined from solid 2″ aluminum stock, and can be seen in Figure 3-8. The reducer specifications can be found in Appendix B

Figure 3-8: $1-1/2''$ to $1''$ pipe reducer.

Aegis West provided us with a report outlining the recommendations for safe setup. From these recommendations, a control zone of 2 m from the edge of the roof was prescribed, and no equipment or persons should be within it at any time. If any equipment was to be installed within the control zone, guiderails must be installed surrounding it. Three sides of railing would be required leaving only the section facing the main roof open for access. From this, all measurement locations were limited to outside of this control zone.

From the Figure 3-6, it can be seen that there are several stacks of solar panels on the west side of the roof. It was also recommended that no equipment is to be installed within 5 m of the solar panels to ensure the safety of any personnel working on the roof either around or with the solar panels.

The locations were also chosen to allow us to get a more complete view of the wind flow around the building. Because of the presence and location of the elevator penthouse, regardless of the prevailing wind direction, the flow will be disturbed downstream of the penthouse, and having only upstream measurements will not be an accurate representation of the entire flow field. So, it was important to have at least one anemometer that was undisturbed for all wind directions, which led to siting the anemometers as such.

Data collection was done using the National Instruments software, LabVIEW. Two virtual instruments were created, one for the mechanical monitors and one for the ultrasonic anemometers. The block diagrams and front panels of the virtual instruments can be found in Appendix C. Both the mechanical and ultrasonic anemometers were set to serial outputs, RS-485 and RS-232, respectively. Serial to USB converters were employed, allowing the anemometers to connect directly to a computer. The computer, power supply, and the anemometer connections were housed in a Campbell Scientific weather resistant enclosure, ENC 16/18, that remained on the roof (Figure 3-9).

(a) (b)

Figure 3-9: a) Campbell Scientific ENC 16/18 weather resistant enclosure enclosure, b) contents of enclosure.

To avoid damaging the computer during the harsh winter weather and rainy summers, a network connection was set up on the roof to allow for remote access to this computer, so that the enclosure is not opened when there is a need to retrieve data from the computer or any computer maintenance is required.

The mechanical monitors were set to collect data at a rate of 1 Hz and the ultrasonic at a rate of 15 Hz. The recorded data were saved to a daily .txt file, with a naming convention of “month, day, year.” Sample outputs from the anemometers are shown below in Table 3-2 and Table 3-3.

Table 3-2: Sample data output, Anemometer A.

Date	Time	Name	Address	Wind Direction (°)	2D Speed (m/s)
2/8/2019	00:00:00.925	A	1	333	7.6
2/8/2019	00:00:01.995	A	1	338	7.8
2/8/2019	00:00:03.082	A	1	327	6.8
2/8/2019	00:00:04.152	A	1	328	7.1
2/8/2019	00:00:05.240	A	1	321	7.4
2/8/2019	00:00:06.358	A	1	333	7.3
2/8/2019	00:00:07.461	A	1	319	7.4
2/8/2019	00:00:08.548	A	1	328	6.2

Table 3-3: Sample data output, Anemometer B.

Date	Time	Name	u (m/s)	v (m/s)	w (m/s)	3D Speed (m/s)	Azimuth (°)	Elevation (°)	S.O.S. (m/s)	Temp (°C)
2/8/2019	00:00:00.152	B	-3.43	6.26	-1.52	7.31	331.3	-12.0	318.82	-20.90
2/8/2019	00:00:00.218	B	-3.27	5.83	-2.29	7.08	330.7	-18.9	318.82	-20.90
2/8/2019	00:00:00.283	B	-2.72	5.52	-1.80	6.41	333.8	-21.1	318.82	-20.91
2/8/2019	00:00:00.349	B	-2.99	6.48	-2.65	7.61	335.2	-25.7	318.82	-20.91
2/8/2019	00:00:00.414	B	-3.10	6.65	-2.89	7.88	335.0	-26.9	318.86	-20.84
2/8/2019	00:00:00.481	B	-3.78	6.68	-3.21	8.32	330.5	-28.5	318.84	-20.89
2/8/2019	00:00:00.546	B	-4.28	5.12	-4.03	7.80	320.1	-38.4	318.90	-20.77
2/8/2019	00:00:00.611	B	-4.23	3.84	-3.80	6.86	312.2	-41.3	319.00	-20.64

Where Azimuth is the wind direction angle in the $u - v$ plane ($0 - 360°$), Elevation is the wind elevation angle relative to the $u - v$ plane ($\pm 90°$), and S.O.S. is the speed of sound. Note that a negative v corresponds to wind from the South, a negative u corresponds to wind from the West, and a negative w corresponds to winds from above (negative elevation).

The ultrasonic anemometers output the wind speed and its three components (u, v and w), direction and elevation of the wind relative to the $u - v$ plane, temperature and the speed of sound. The mechanical monitors output the 2D wind speed and direction. The timestamps on each reading are added by LabVIEW and are corresponding to the moment the device was polled, meaning a request was sent to the device from LabVIEW to output wind data.

3.4 Data Processing

The equipment was set up on November 30th, 2018, and the continuous data collection began on February 8th, 2019. While the data collection remains ongoing, for the scope of this thesis, the data processed and analyzed were limited to the six month period of February 8th to August 8th 2019. Note that there are a few days of data that were not collected throughout the dataset, due to power outages and scheduled maintenance of the engineering network.

For a reference wind speed and direction, data from the University of Alberta, Earth and Atmospheric Science (EAS) Department weather station on the roof of the University of Alberta's Henry Marshall Tory Building were used. This building is the tallest within its immediate vicinity, at 57 m tall, with all the surrounding buildings significantly lower. The weather station is positioned at 64 m above the ground and appears to be sufficiently elevated above the surrounding ground and building roughness elements. Because of this, we chose to consider the measurements as a reference point for wind analysis on campus. The weather station consists of a RM Young 05103 mechanical monitor and a Campbell Scientific CR10X data logger. The data are measured at a rate of roughly 1 Hz and are averaged and archived as hourly wind data. The archives date back to July 2000, meaning we could use reference measurements for the same six month period of February 8th to August 8th 2019, for our analysis. The Tory weather station (TWS) provides hourly averaged data for solar radiation, rain, temperature, relative humidity, and barometric pressure, along with 2D wind speed and wind direction.

To process the data, the statistical analysis software RStudio [60] was used. The raw daily wind data files were first averaged to determine daily averages of wind speed and direction. As the wind monitors output the 2D wind speed and the ultrasonic output the 3D wind speed and its three components, direct comparisons between them are not correct. To have accurate comparisons, the magnitude of the horizontal (2D) component of the wind velocity for the ultrasonic wind data was calculated, and was defined as V (m/s).

$$V = \sqrt{u^2 + v^2} \tag{3.6}$$

Where u is the longitudinal component of wind velocity in the East-West direction, and v is the lateral component in the North-South direction.

The daily 2D averages were then calculated at all measurement locations. To determine the average direction, the simple arithmetic mean approach does not work, as we are dealing with polar quantities. As such, the mean of circular quantities was calculated, using equations (3.7) and (3.8) below:

$$\bar{s} = \frac{1}{n}\sum_{j=1}^{n} \sin\theta_j\,, \qquad \bar{c} = \frac{1}{n}\sum_{j=1}^{n} \cos\theta_j \tag{3.7}$$

$$\bar{\theta} = \begin{cases} \arctan\left(\frac{\bar{S}}{\bar{c}}\right), & \bar{s} > 0, \bar{c} < 0 \\ \arctan\left(\frac{\bar{S}}{\bar{c}}\right) + 180°, & \bar{c} < 0 \\ \arctan\left(\frac{\bar{S}}{\bar{c}}\right) + 360°, & \bar{s} < 0, \bar{c} < 0 \end{cases} \tag{3.8}$$

Where θ is the wind direction.

The standard deviation of the wind direction measurements were calculated using the Yamartino method:

$$\sigma_\theta = \arcsin(\varepsilon)\left[1 + \left(\frac{2}{\sqrt{3}} - 1\right)\varepsilon^3\right] \tag{3.9}$$

Where

$$\varepsilon = \sqrt{1 - (\bar{s}^2 + \bar{c}^2)} \tag{3.10}$$

The daily wind power densities (WPD) were then also calculated, using equation (2.26). The averaged air density at DICE was calculated from measured temperature and pressure readings taken from the TWS, and using the ideal gas equation:

$$\rho = \frac{1}{\mathrm{R}}\frac{P}{T} \tag{3.11}$$

Where ρ is the air density, P is the air pressure, T is the measured air temperature, and R is the gas constant of dry air, $\mathrm{R} = 287\ \mathrm{J/kg\ K}$.

After the daily WPD's and averages were calculated, hourly averages were determined for both the mechanical and ultrasonic measurements. Hourly averages allow us to have accurate comparisons between our experimental data, and the TWS reference measurements.

The raw unprocessed data from the ultrasonic anemometers were also averaged into 1 min and 10 min increments. These averages were used to determine the turbulence intensity of the three components of the

wind velocity, using equations (2.15), (2.16), and (2.17). The turbulence intensities were then plotted using RStudio.

A wind resource assessment software, Windographer [61], was then used to plot the daily wind speeds and wind power densities, create wind roses, and fit Weibull distributions, and Tecplot 360 [62], a data visualization and CFD post processing software was used to create radial plots to compare the numerical and experimental data.

The results of this wind resource assessment are presented in the following chapter.

4. Results and Discussion

4.1 Application of Validation Framework and Results of Case Study

Following the validation methodology that was created and presented in section Proposed CFD Validation Framework, wind flow around the campus was simulated and analyzed for four inflow wind directions, $0°$ (North), $90°$ (East), $180°$ (South), and $270°$ (West). The reference wind speed, U_{ref}, at a height of 80 m was varied between $4 - 12$ m/s.

Data were collected for six months and, as previously discussed; the Tory Weather Station (TWS) only provides hourly averages for the free stream data, so the DICE data were averaged into hourly intervals. The TWS data were then filtered for the same inflow direction and speeds as was simulated and 36 bins were created for the free stream flow. The number of resultant data points (hourly averages) in each bin can be found in Table 4-1.

Table 4-1: Number of measurement samples (hourly averaged) for each free stream bin.

Speed \ Direction	North	East	South	West
4 m/s	12	5	6	11
5 m/s	12	6	3	5
6 m/s	5	2	2	2
7 m/s	4	0	0	0
8 m/s	2	0	0	1
9 m/s	0	0	0	2
10 m/s	0	0	0	0
11 m/s	0	0	0	0
12 m/s	0	0	0	0

As can be seen, there are a number of bins for which no measurements fit the criteria, so only free stream velocities of $4, 5,$ and 6 m/s were considered for the validation process. The DICE data at positions A, B, D, and E were then filtered and the measurement intervals corresponding to those in the free stream bins were obtained and placed into bins of their own. It is important to note here that only a limited number of measurements were selected as validation points because of the strictness of the acceptance criteria, namely, the allowable range allotted to a given bin. This allows us to test the validity of the model under very precise conditions, which can ensure that any issues with the model can be exposed. Because of the short duration of this project, a test of validity with more lenient criteria and a comparison between the two could not done, but was suggested for future work in section 5.2.

Next, the simulated wind speed and direction at the four DICE locations were exported from CFD Post. Two different methods were used to determine the simulated wind speed and direction. In the first method (from here on, "the single point method", SPM), points were placed at the exact measurement locations on DICE and the speed and direction were determined. For the second method (from here on, "the point cloud method", PCM), point clouds of 100 points on a 1 m x 1 m horizontal plane centered on the exact measurement locations were created, and the speed and direction at each point were determined, and an average value was taken. Both methods can be seen in Figure 4-1.

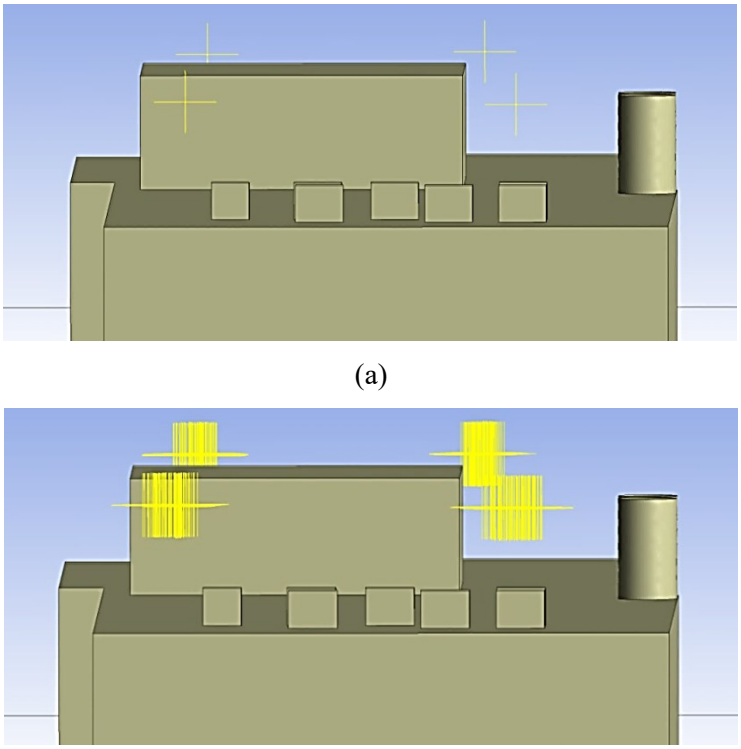

(a)

(b)

Figure 4-1: Methods of data extraction from the CFD results: (a) using the SPM, (b) using the PCM.

To calculate the difference between the experimental and numerical results, two methods were also used. The first method (from here on, "the average method", AM) took all measurements in the bins and an average value of wind speed and direction were calculated, and then used to compare to the CFD results, as it is commonly done in literature [36]–[38], [41], [45]. The second proposed method (from here on, "the standard deviation method", SDM) consisted of comparing the measurement which had the least variability in the wind direction with the CFD results. The date and time of the TWS measurement that had the lowest wind direction standard deviation in each bin was noted, and the corresponding DICE measurement was

used to compare with CFD. Both these methods were used to ensure that the best validation technique was being applied, and to assess any differences that arise from the application of different validation methods.

Radial and scatter plots were created to visually assess and compare the differences between the experimental and numerical results. Radial plots were used to show the differences between the numerical and experimental results for a given wind speed and direction at each measurement location, and the scatter plots were used to assess the overall correlation of the simulated and measured results at all locations and all incident wind directions. The scatter plots are shown in Figures Figure 4-2 – Figure 4-5 below. Note that 'SDM', 'AM', 'SPM', and 'PCM' correspond to the standard deviation method, average method, the single point method and the point cloud method, respectively. The solid line represents a perfect agreement between the simulated and measured results, and the dashed lines represent a 10% deviation. A, B, D, and E are the four anemometer measurement locations.

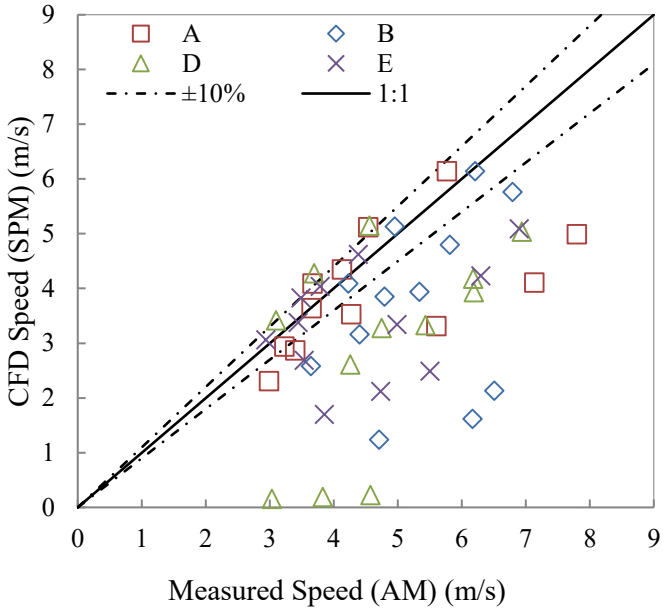

Figure 4-2: Comparison between the measured and simulated speeds at all locations, using the single point method and the average method

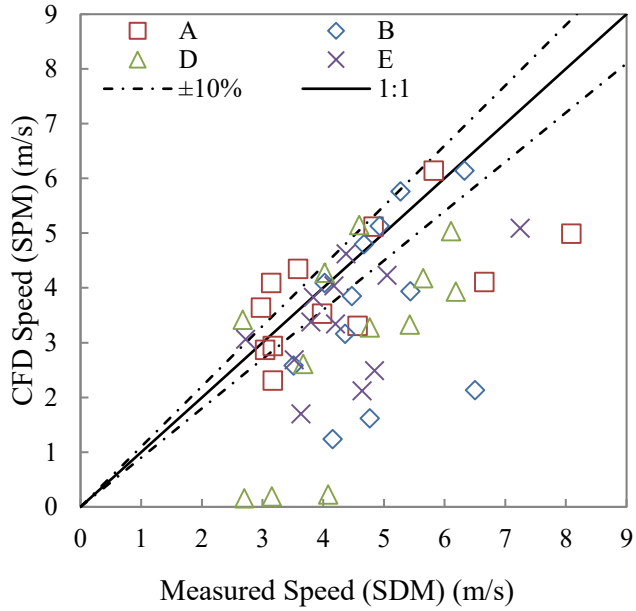

Figure 4-3: Comparison between the measured and simulated speeds at all locations, using the single point method and the standard deviation method.

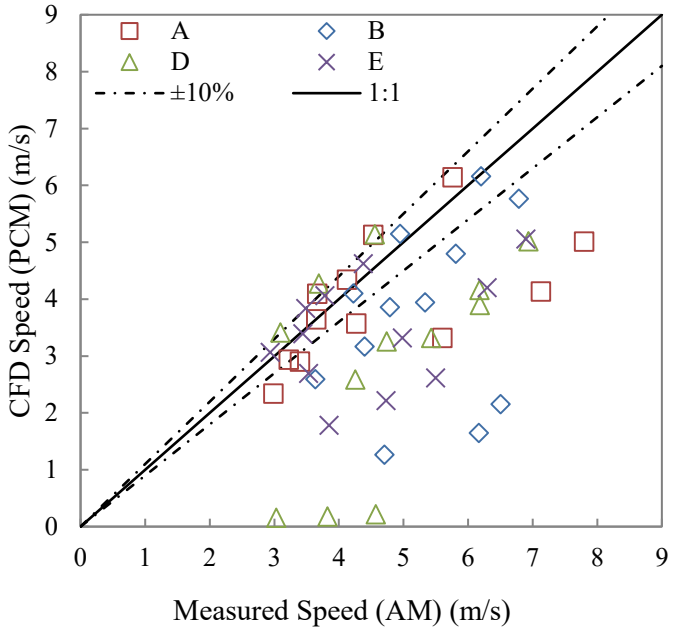

Figure 4-4: Comparison between the measured and simulated speeds at all locations, using the point cloud method and the average method.

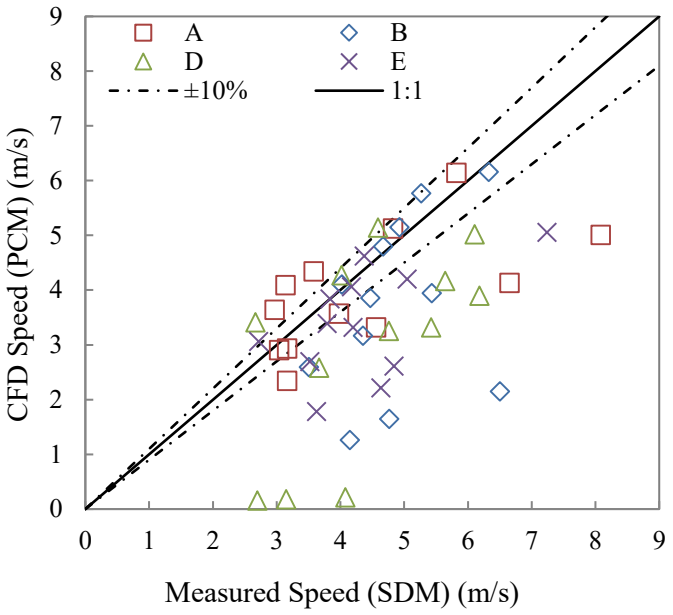

Figure 4-5: Comparison between the measured and simulated speeds at all locations, using the point cloud method and the standard deviation method.

As previously indicated, the objective of these plots is not the assess the exact deviations of the model from the measured speeds, but to see the overall agreement of the CFD results with the measured results, using the different comparison methods. The first clear inference we can make from these plots is that the CFD

is more consistently underestimating the speed, regardless of the method of analysis used. Assessing the differences between Figure 4-2 and Figure 4-4, and the differences between Figure 4-3 and Figure 4-5 we can see that there is no significant variation between the point cloud and the single point methods, which indicates that the results are not within regions of high gradients, and we can conclude that the grid is fine enough to accurately resolve the flow at the target locations, and the single point method seems adequate for analysis.

Comparing Figure 4-2 with Figure 4-3 and Figure 4-4 with Figure 4-5, we can see that there are very minor differences between the standard deviation method and the average method; however the numerical results seem to be a slightly better representation of the measured results when the standard deviation method of analysis is used. The results for the standard deviation method appear to shift closer to and have an overall closer fit to the 1:1 ratio line. This is not unexpected, as the standard deviation method used the hours which had the least wind variability, meaning the wind direction was more consistently blowing in the same direction, which is better reproduced by a CFD simulation.

The radial comparisons at all locations (A, B, D, and E) for free stream velocities of $4 - 6\ \mathrm{m/s}$ are shown in Figure 4-7 – Figure 4-13 below. Note that 'SDM' and 'AM' correspond to measurements using the standard deviation method and the average method, respectively, 'CFD Speed' is the simulated speed, and 'TWS' is the reference free stream measurement from the Tory Weather Station.

Figures Figure 4-6, Figure 4-8, Figure 4-10, and Figure 4-12 contrast the differences between the measured and simulated wind speeds for all incident wind directions and free stream speeds. Figures Figure 4-7, Figure 4-9, Figure 4-11, and Figure 4-13 present the deviations of the simulated wind direction to the measured wind direction for all incident winds. The solid black line represents a $0°$ deviation (i.e. exact match), $30°$ represents a clockwise deviation, and $-30°$ represents a counter-clockwise deviation of the numerical results from the experimental results.

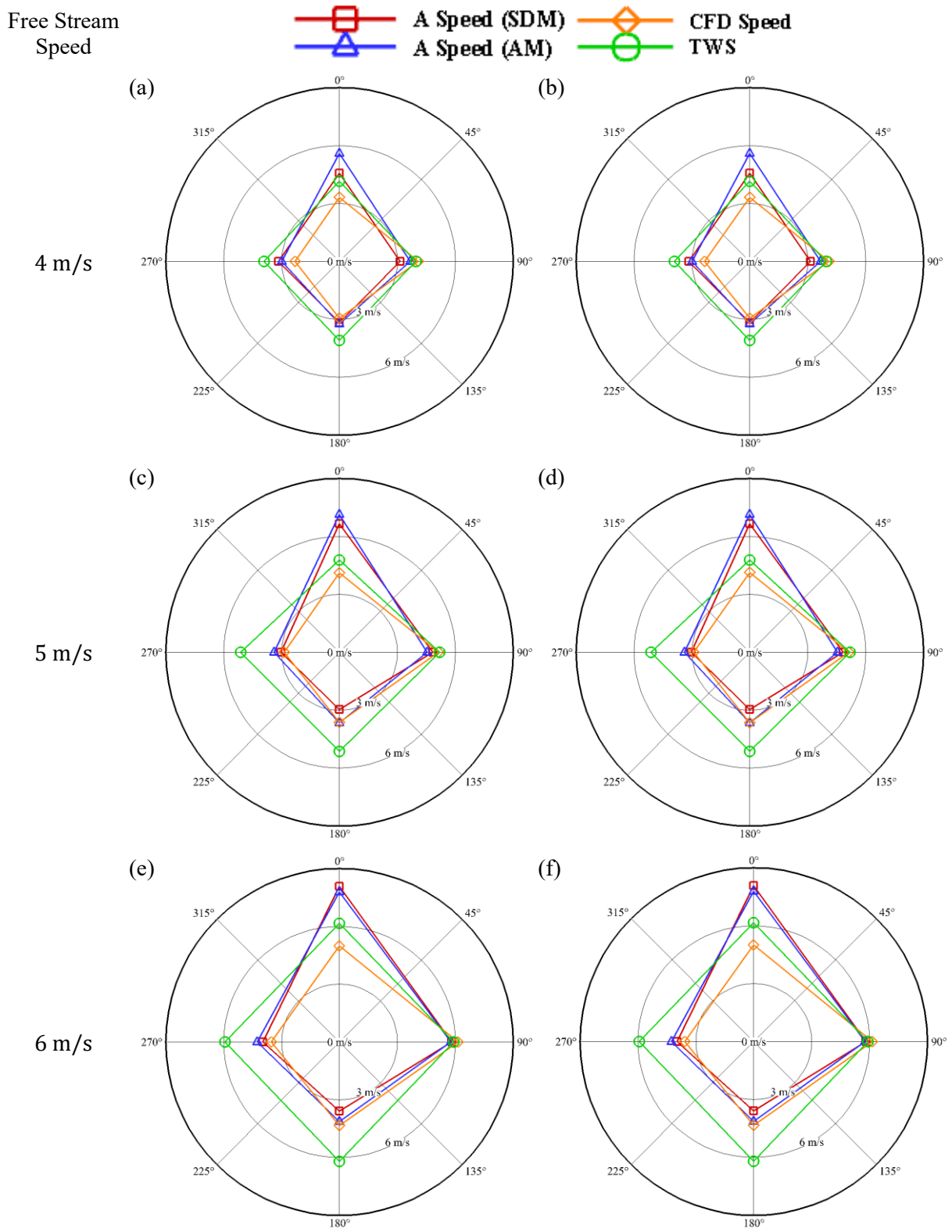

Figure 4-6: Comparison of measured and simulated wind speeds at location A using the single point (a, c, e) and point cloud (b, d, f) methods.

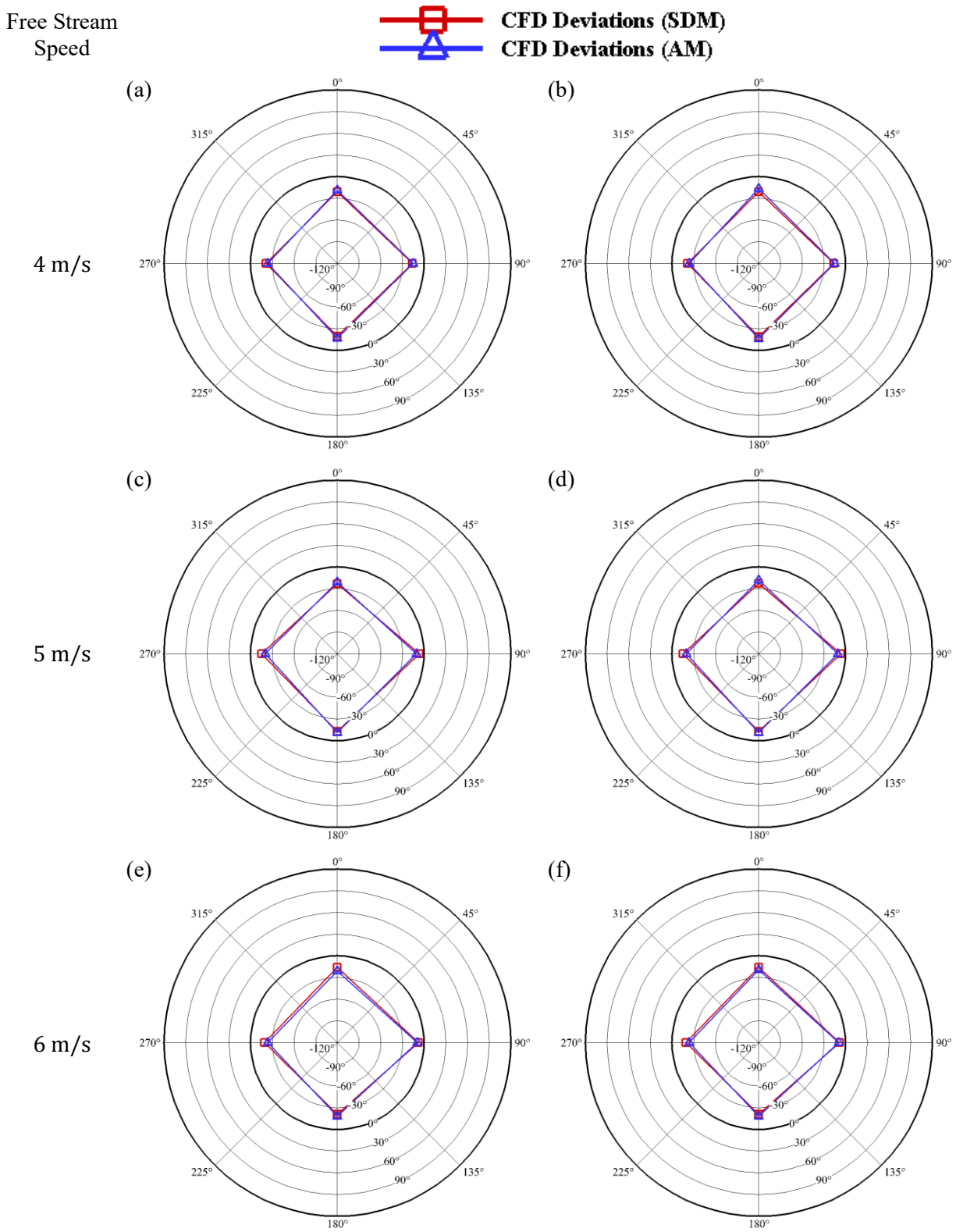

Figure 4-7: Deviation of simulated wind direction from measured wind direction at location A using the single point (a, c, e) and point cloud (b, d, f) methods.

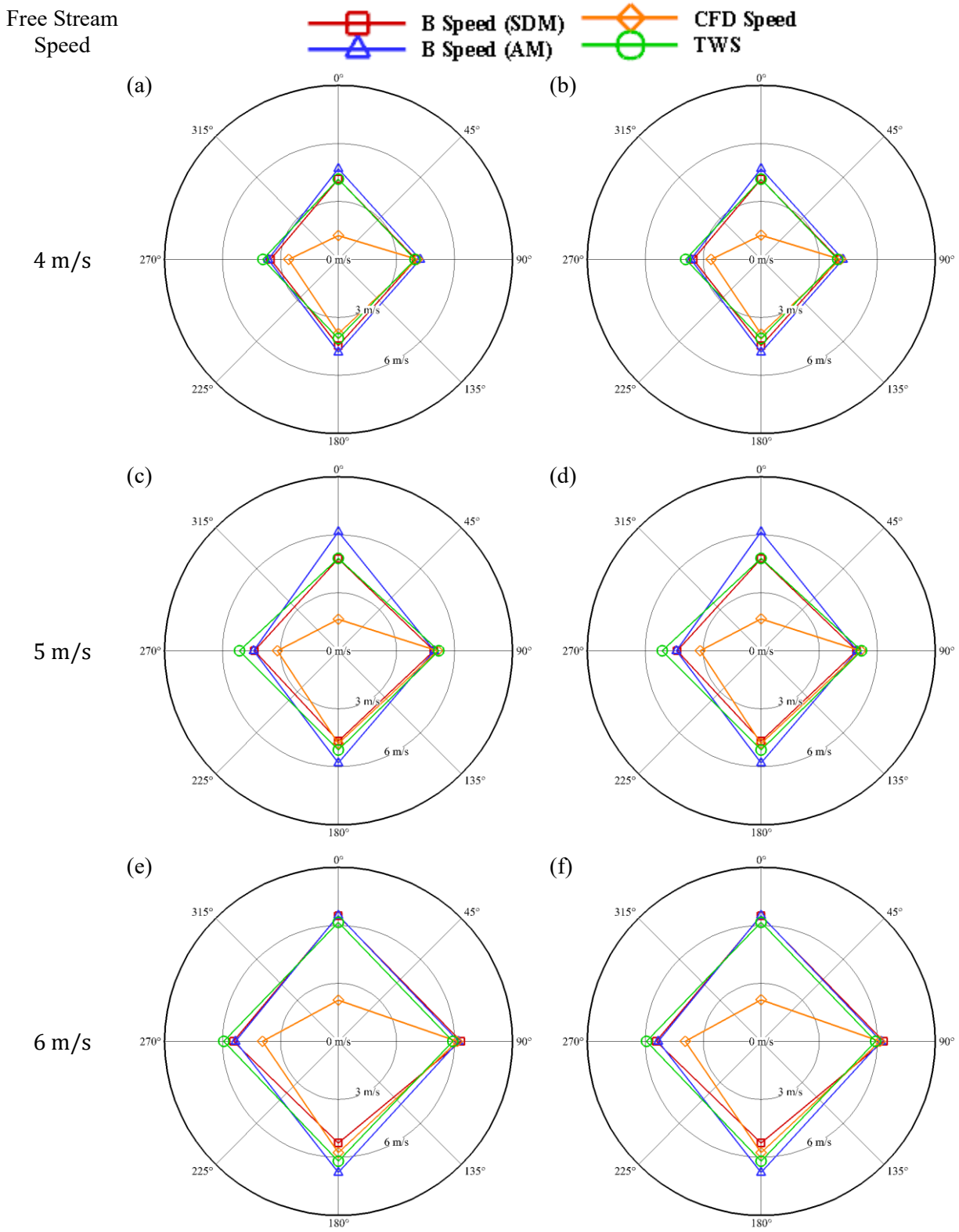

Figure 4-8: Comparison of measured and simulated wind speeds at location B using the single point (a, c, e) and point cloud (b, d, f) methods.

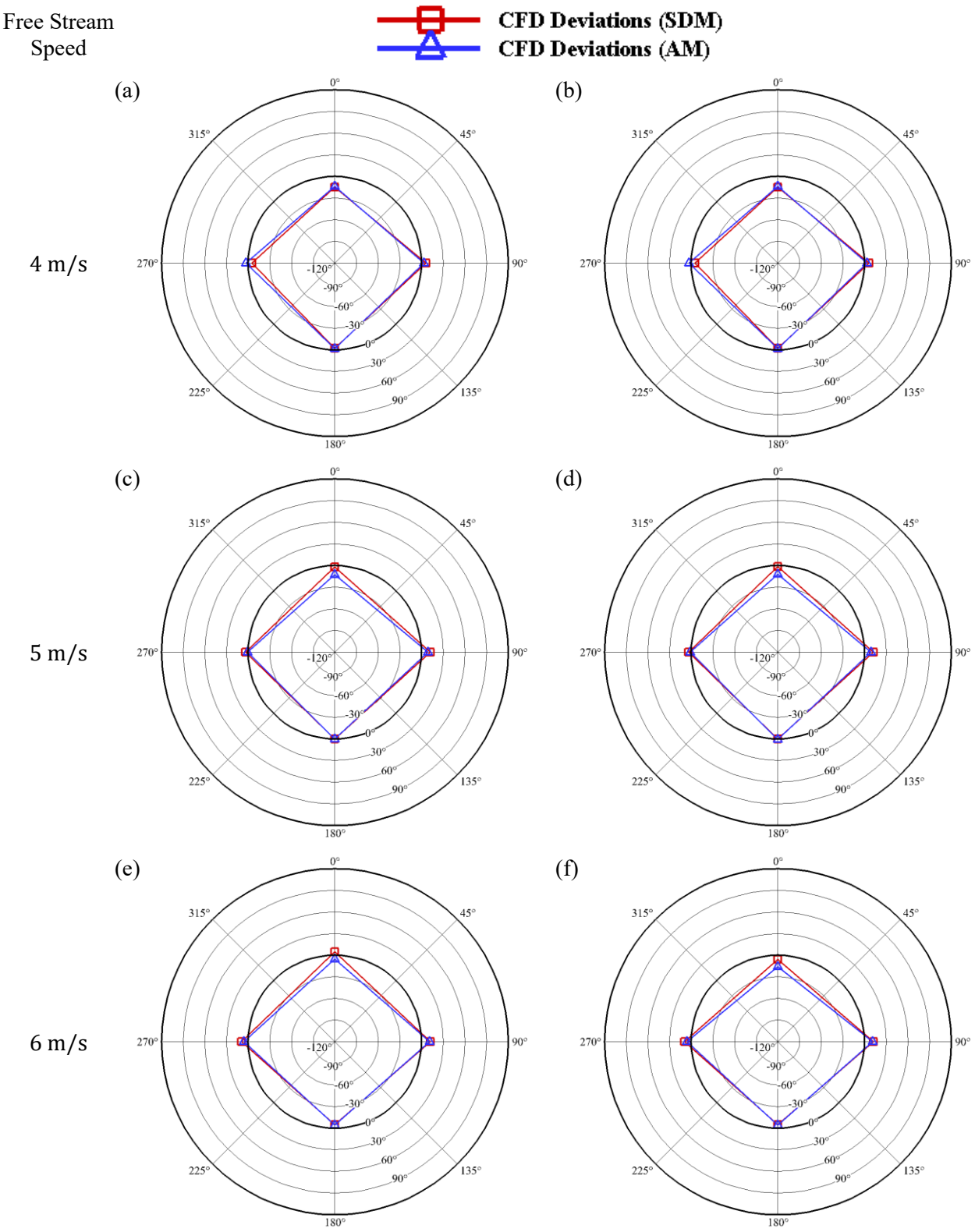

Figure 4-9: Deviation of simulated wind direction from measured wind direction at location B using the single point (a, c, e) and point cloud (b, d, f) methods.

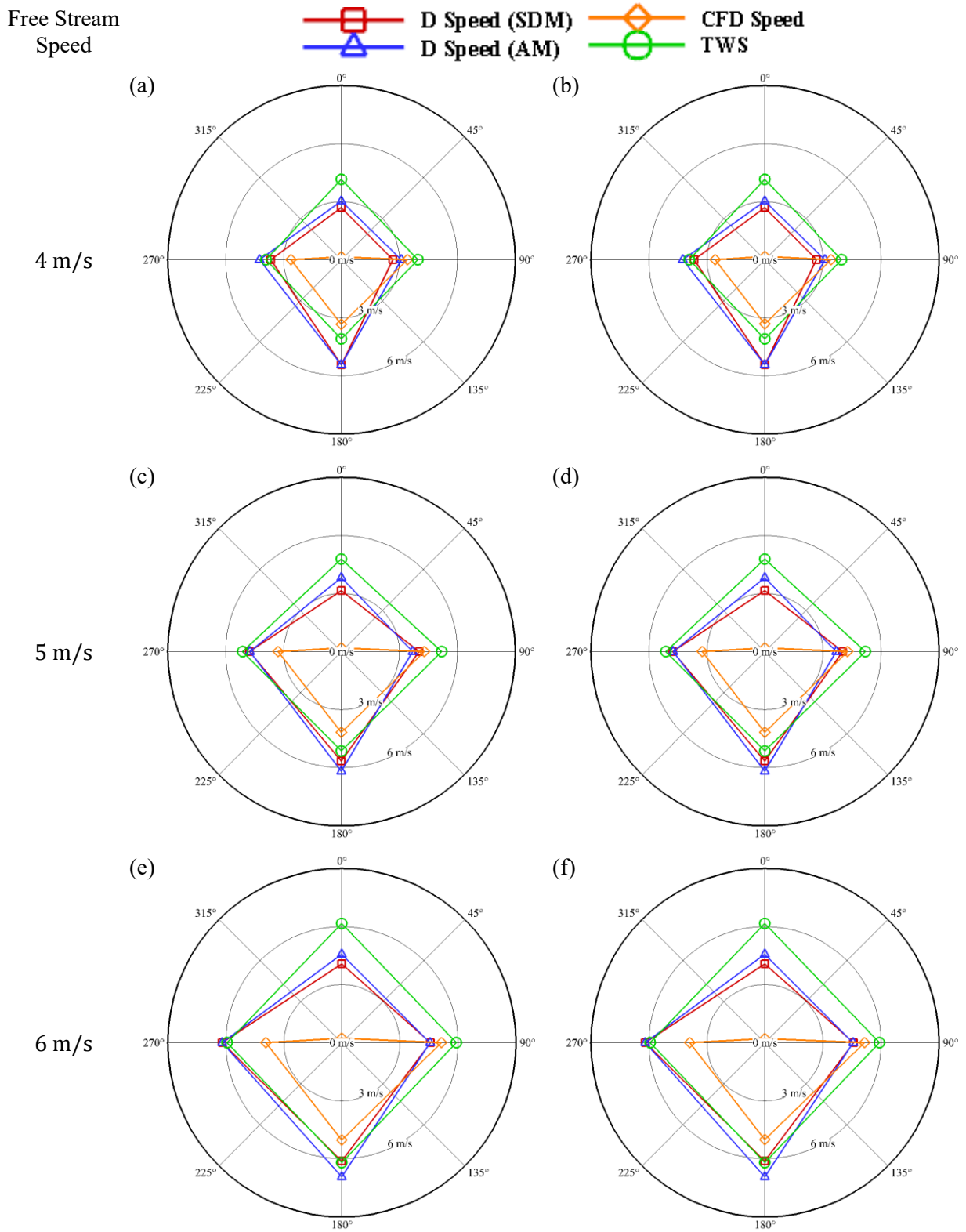

Figure 4-10: Comparison of measured and simulated wind speeds at location D using the single point (a, c, e) and point cloud (b, d, f) methods.

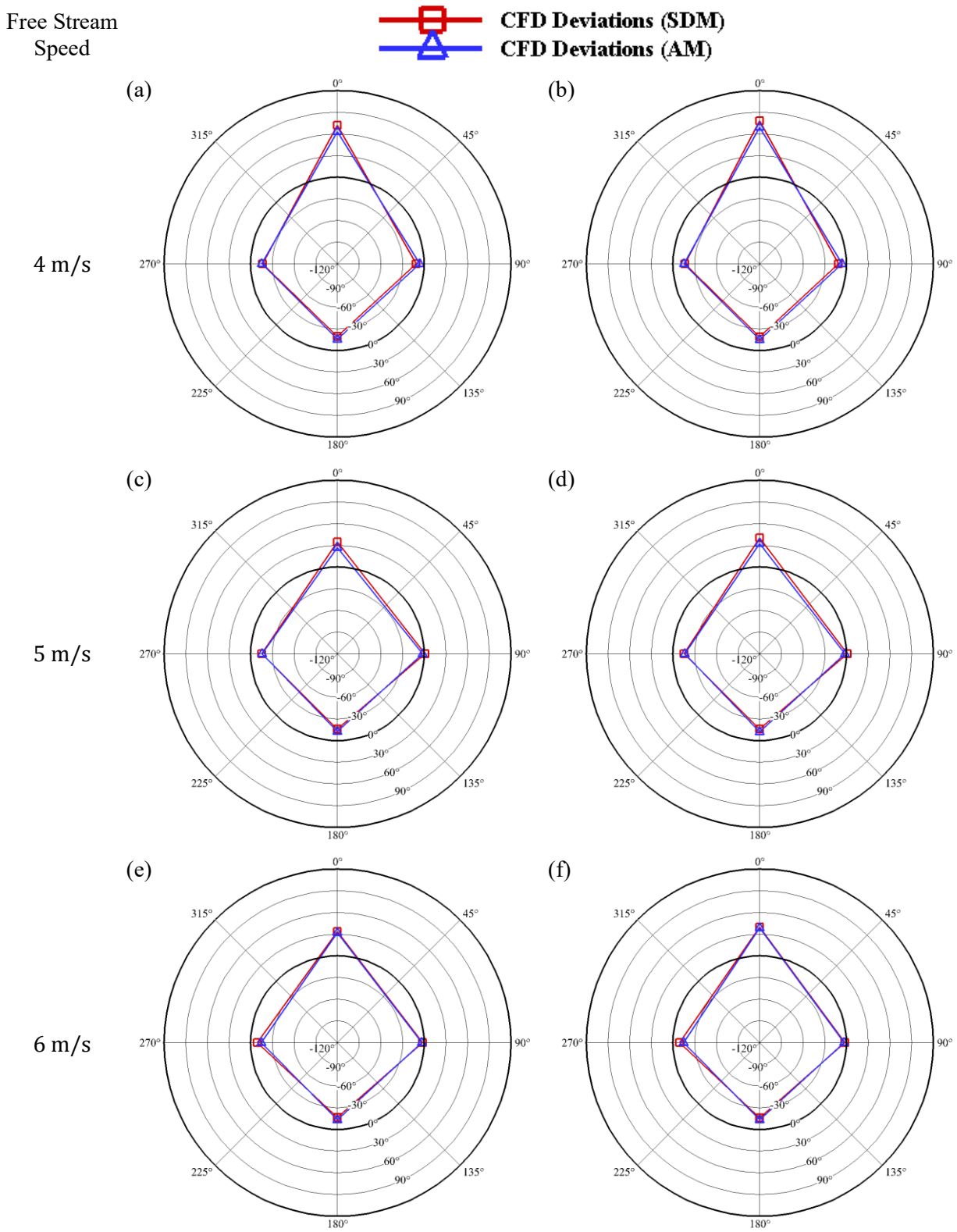

Figure 4-11: Deviation of simulated wind direction from measured wind direction at location D using the single point (a, c, e) and point cloud (b, d, f) methods.

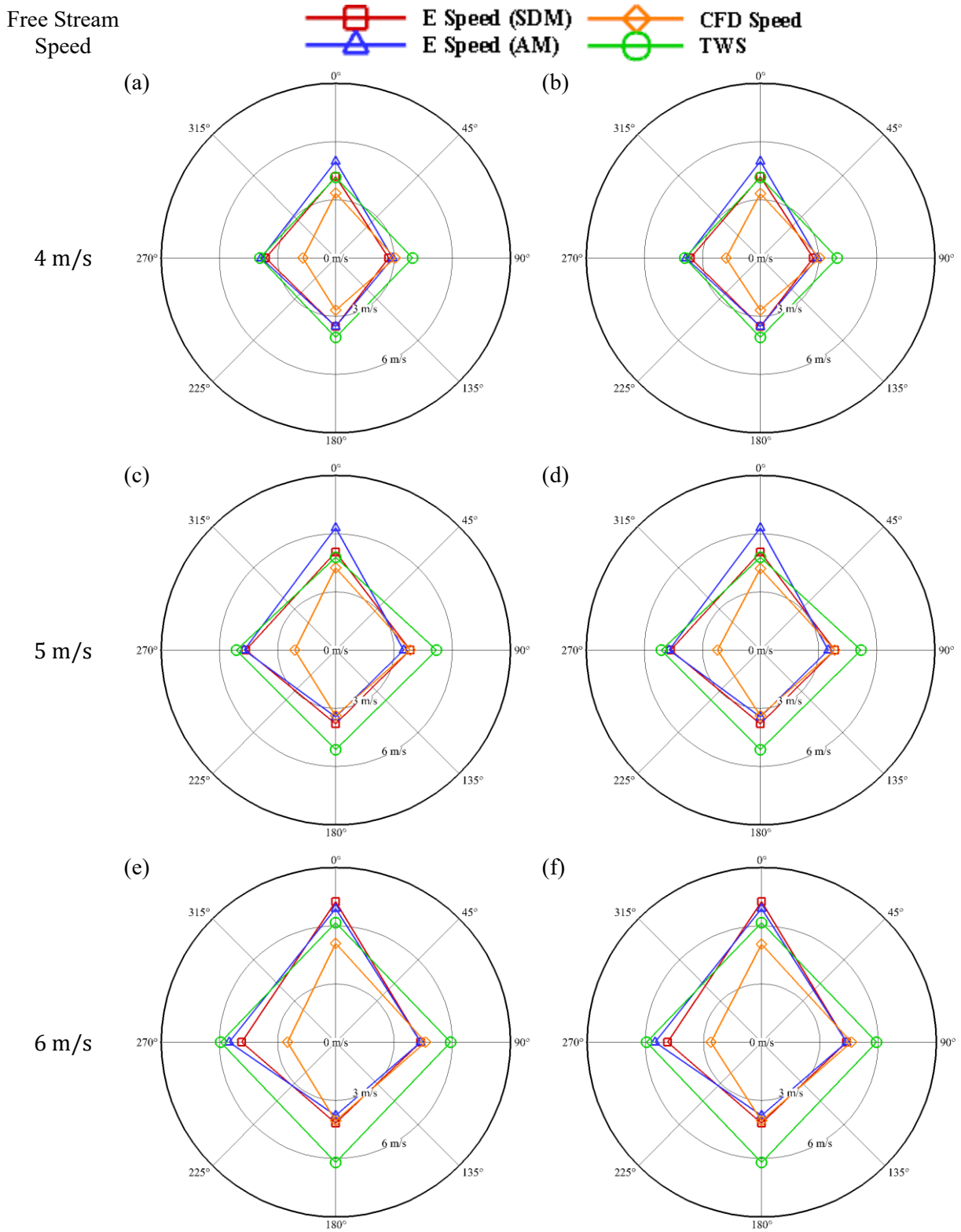

Figure 4-12: Comparison of measured and simulated wind speeds at location E using the single point (a, c, e) and point cloud (b, d, f) methods.

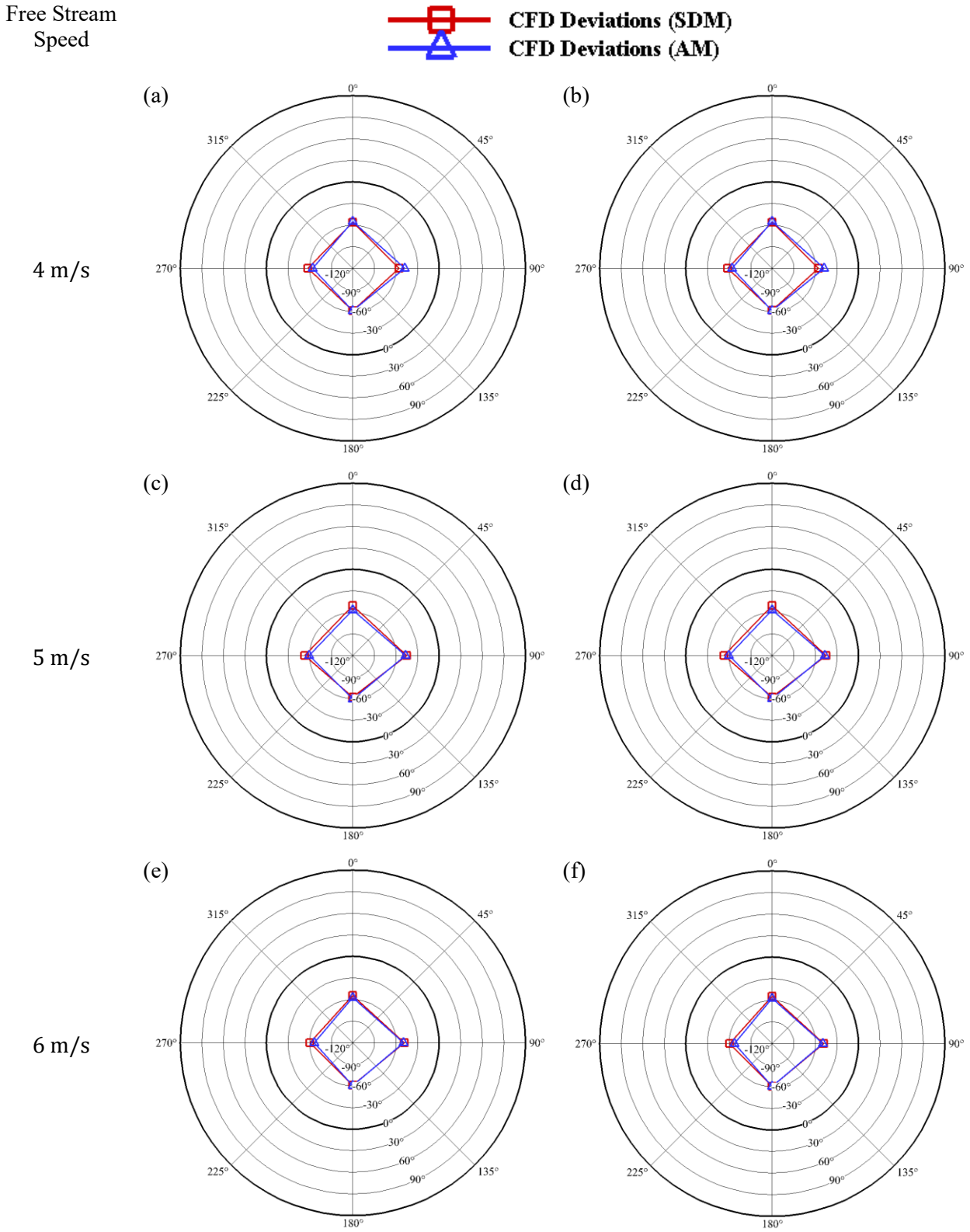

Figure 4-13: Deviation of simulated wind direction from measured wind direction at location E using the single point (a, c, e) and point cloud (b, d, f) methods.

Figures Figure 4-6 – Figure 4-12, confirm the preliminary conclusions made from the scatter plots, as there only minor differences between the numerical speed and direction for the single point method and the point cloud method at all locations, and the single point method is considered sufficient, and will be used to analyze the results of these simulations. Examining Figures Figure 4-6, Figure 4-8, Figure 4-10, and Figure 4-12 also confirms the initial inferences made, as we can see that the numerical results seem to be a better representation of the measured speeds when the standard deviation method of analysis is used, and we can observe that for all locations, the CFD is almost always underestimating the speed, as previously deduced by the scatter plots. From these radial plots, we can also see that at all locations and for all free stream speeds, the largest deviations between the simulated and measured speeds are consistently for winds from the North, followed by West and South, in that order. The simulated speeds for East winds seem to have regularly good agreements with the experimental values, for both methods of analysis used, at all locations.

When examining Figures Figure 4-7 – Figure 4-13, however, there only seem to be slight and insignificant differences between the standard deviation and average methods for the wind direction at most for most locations and incident wind directions. Figures Figure 4-7 and Figure 4-9 show that at locations A and B, there is a good agreement between the measured and simulated wind directions, with most deviations less than $20°$, and a few less than $25°$. This is comparable to the results found by Blocken et al. [38], who had average deviations of $21°$ and $22°$ for all directions at both measurement locations.

From Figures Figure 4-10 and Figure 4-11, we find that the numerical estimates of the North wind produce a seemingly isolated large deviation from the measured at that location, for both the speed and direction. Upon further inspection of the simulations for the North wind, it is evident that the measurement location D falls within a recirculation zone, as shown in Figure 4-14, which is the cause of this inconsistency.

Further inspection of the numerical results shows a large area of recirculation on the West side of the roof for incident winds coming from the West, as shown in Figure 4-15. As this is not present on the East side for winds incident from the East (Figure 4-16), this recirculation zone is attributed to the presence of the solar panels on the West side.

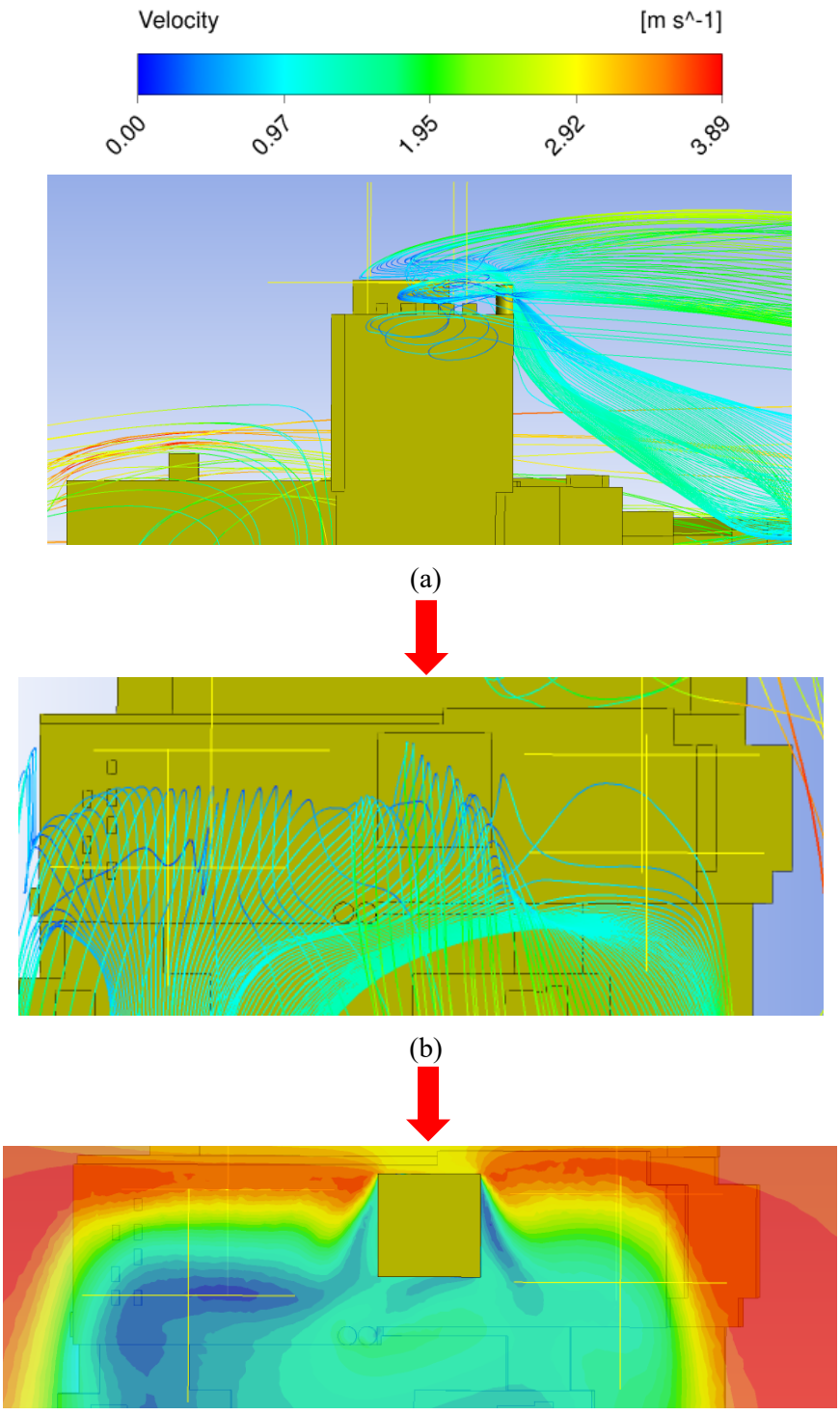

Figure 4-14: Recirculation over DICE for North winds at 4 m/s. (a) View from West edge of DICE, (b) View from above DICE, (c) Velocity contour at height of anemometers. Note that the red arrows indicate the incident wind direction.

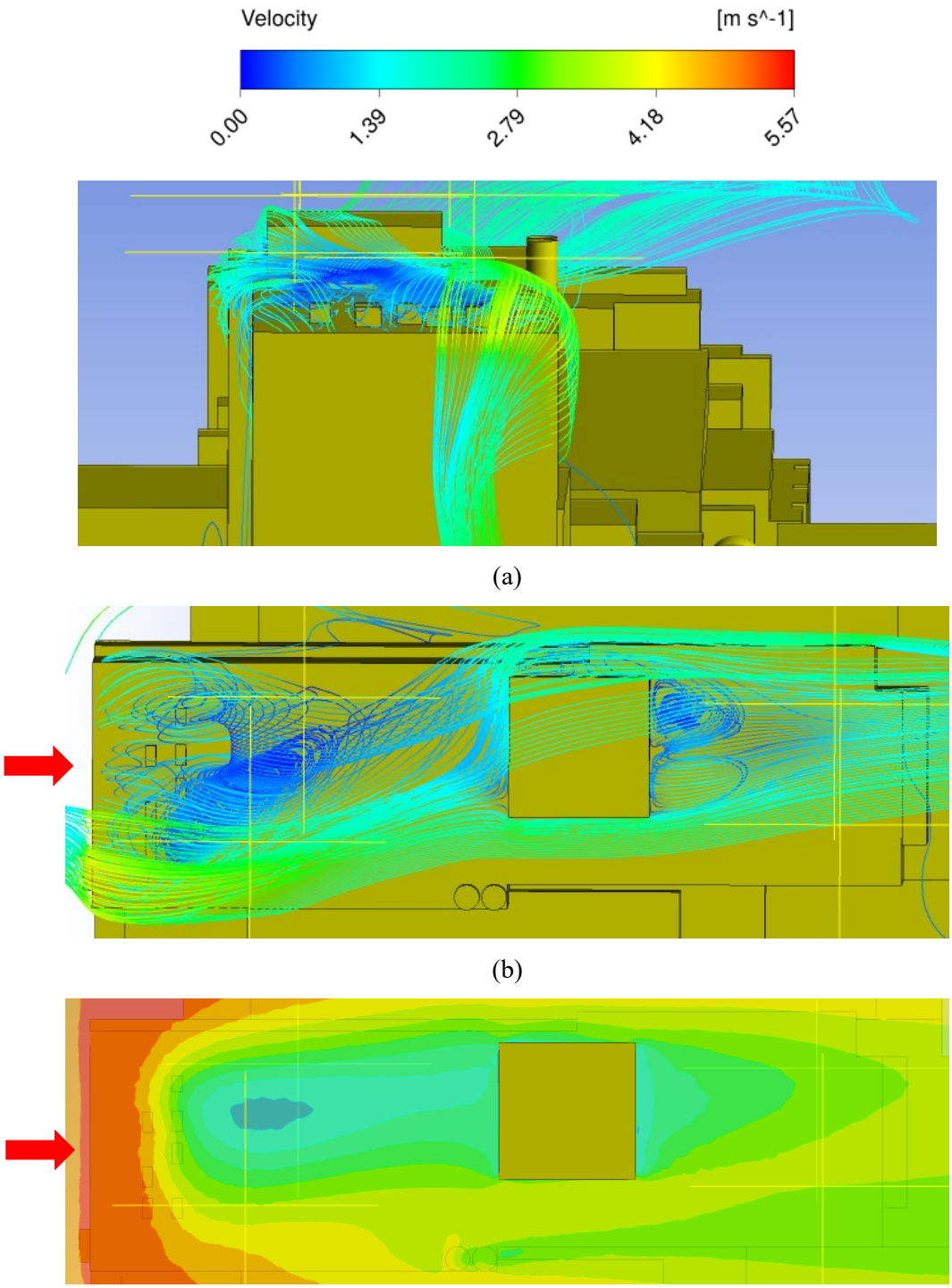

(a)

(b)

(c)

Figure 4-15: Recirculation over DICE for West winds at 4 m/s. (a) View from West edge of DICE, (b) View from above DICE, (c) Velocity contour at height of anemometers. Note that the red arrows indicate the incident wind direction.

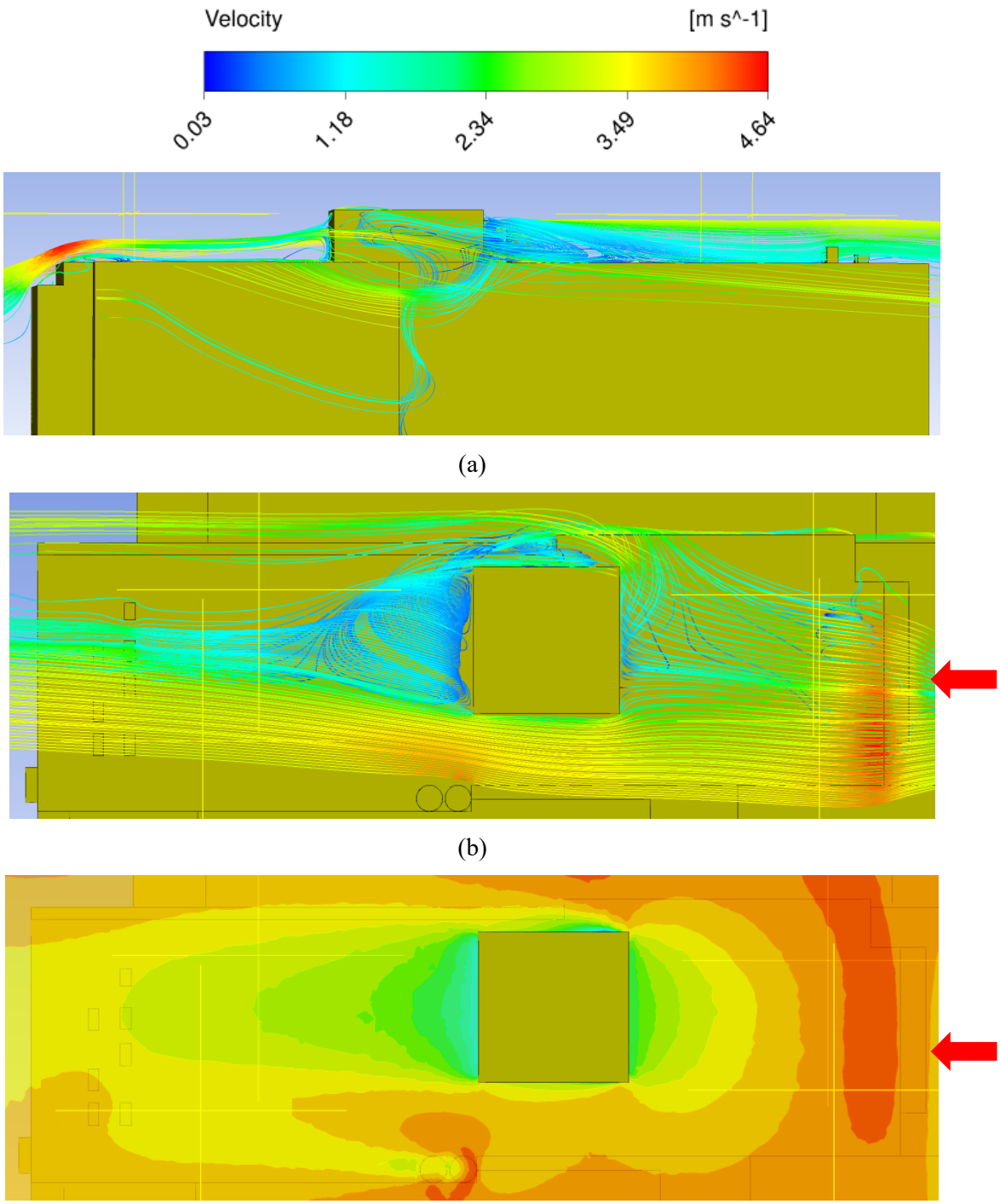

(a)

(b)

(c)

Figure 4-16: Recirculation over DICE for East winds at 4 m/s. (a) View from North edge of DICE, (b) View from above DICE, (c) Velocity contour at height of anemometers. Note that the red arrows indicate the incident wind direction.

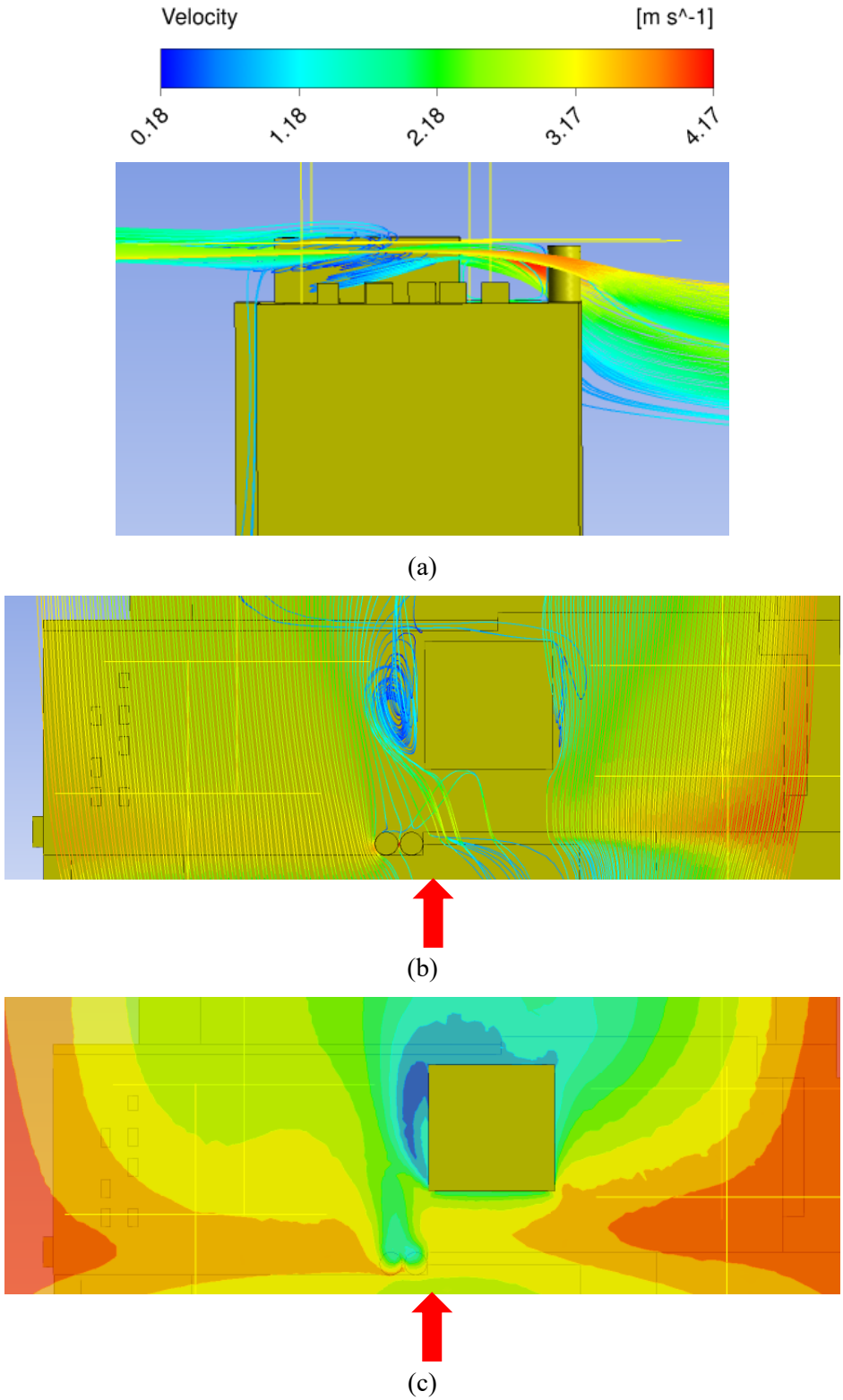

Figure 4-17: Flow over DICE for South winds at 4 m/s. (a) View from West edge of DICE, (b) View from above DICE, (c) Velocity contour at height of anemometers. Note that the red arrows indicate the incident wind direction.

Location E however, shows consistently large deviations between the measured and simulated wind directions for all incident wind directions and free stream speeds, which are far greater than any differences experienced by the other anemometers, including anemometer D, which is nearest to E. Assessing the results of the CFD simulations for wind coming from the South, Figure 4-17, also shows no signification areas of recirculation that could be affecting anemometer E this greatly, which could mean that the piece of equipment might be experiencing software issues, or could have alignment issues and may need to be recalibrated.

The average absolute deviations between the CFD results and the measured results were tabulated to better quantify the validity of the simulations. Since anemometer D was situated in a recirculation zone, for incident winds coming from the North, and anemometer E could potentially be experiencing issues, these measurements were taken out of the study and will not be considered when making a final assessment. The values in Table 4-2 were calculated by taking the absolute value of the difference between the numerical results and the experimental results at all locations for each incident wind direction and free stream speed, and finding the average. The decision to consider all locations for any given incident wind direction was made as there was no clear distinction or distinguishing pattern between the deviations from the upstream and downstream measurement points for us to consider. The differences between the numerical and experimental results at each measurement location for all incident wind directions can be found in Appendix D, along with the percent error of the numerical speeds at each measurement location.

The deviation in speed for the standard deviation method (D_{SDM}) for North winds at $4\ \mathrm{m/s}$ (for the single point method) was calculated as follows:

$$D_{SDM,N,4} = \frac{1}{n}\sum_{i=m}^{n}\left|V_{num,i} - V_{exp,i}\right| = \frac{1}{2}\left(\left|V_{num,A} - V_{exp,A}\right| + \left|V_{num,B} - V_{exp,B}\right|\right)$$

$$D_{SDM,N,4} = \frac{1}{2}\left(|3.31\ \mathrm{m/s} - 4.56\ \mathrm{m/s}| + |1.24\ \mathrm{m/s} - 4.15\ \mathrm{m/s}|\right) = 2.08\ \mathrm{m/s}$$

The italics denote the smallest deviation (closest agreement between the measured and numerical results) between the standard deviation method and the average method. We can see that the standard deviation method produced smaller deviations more frequently, as 15 of the 24 numerical deviations were better agreements with the measured values, most commonly for deviations in speed. Table 4-3 presents the corresponding average percent error of the deviations between numerical and experimental speeds for each incident wind direction.

Table 4-2: Average deviations in speed and direction for each incident wind direction.

	North	East	South	West
Free Stream Speed 4 m/s				
Deviation in Speed (SDM) (m/s)	*2.08*	0.59	*0.98*	*0.95*
Deviation in Speed (AM) (m/s)	2.88	*0.29*	1.11	1.13
Deviation in Direction (SDM) (°)	17.75	10.97	13.36	14.11
Deviation in Direction (AM) (°)	*16.20*	*8.03*	*10.91*	*13.85*
Free Stream Speed 5 m/s				
Deviation in Speed (SDM) (m/s)	*2.84*	*0.25*	*0.76*	*0.95*
Deviation in Speed (AM) (m/s)	3.78	0.45	1.01	1.08
Deviation in Direction (SDM) (°)	*12.50*	*6.77*	9.58	*11.32*
Deviation in Direction (AM) (°)	16.57	7.33	*7.95*	12.27
Free Stream Speed 6 m/s				
Deviation in Speed (SDM) (m/s)	3.73	0.36	*0.77*	*1.40*
Deviation in Speed (AM) (m/s)	*3.59*	*0.35*	1.05	1.46
Deviation in Direction (SDM) (°)	*10.25*	*7.48*	14.02	*12.51*
Deviation in Direction (AM) (°)	13.27	8.00	*11.98*	14.81

Table 4-3: Average percent error of numerical speeds for each incident wind direction.

	North	East	South	West
Free Stream Speed 4 m/s				
Error in Velocity (SDM) (%)	48.80	19.97	19.89	27.46
Error in Velocity (AM) (%)	57.28	8.40	22.40	30.14
Free Stream Speed 5 m/s				
Error in Velocity (SDM) (%)	52.11	5.56	17.12	21.39
Error in Velocity (AM) (%)	58.04	10.83	16.68	24.85
Free Stream Speed 6 m/s				
Error in Velocity (SDM) (%)	52.76	6.87	16.06	25.06
Error in Velocity (AM) (%)	51.63	6.87	15.96	26.66

As previously mentioned, the largest deviations for speed are consistently for winds from the North, which is confirmed by the results in Table 4-2 and Table 4-3. We can also see that at 6 m/s, the deviations in the wind direction are largest for the winds from the West and South. Looking at the simulated geometry in Figure 4-18: CFD geometry., we can immediately note that the DICE building and attached car park is at the North West edge, and the surroundings to the North and West of the building are not modelled, which could be the cause of the large deviations. The deviations for South winds could be attributed to some simplifications to the geometrical details of the surrounding buildings. In addition, the North Saskatchewan

River runs in a deep valley around the University of Alberta, and is immediately North and West of DICE, separated by some homes, parks, and vegetation.

The presence of a body of water could create local wind from the water body to the land during the day, and local wind from the land to the water during the night [63]. This is because water has a higher effective thermal mass than that of land, and under the sun, the surface of land is heated up much faster than water. The warmer air above the land goes up due to the buoyancy effect, creating an air pressure differential from the water to land. During the night, land cools faster than water due to thermal radiation, and again the thermal buoyancy in the air forms a land to water wind [63].

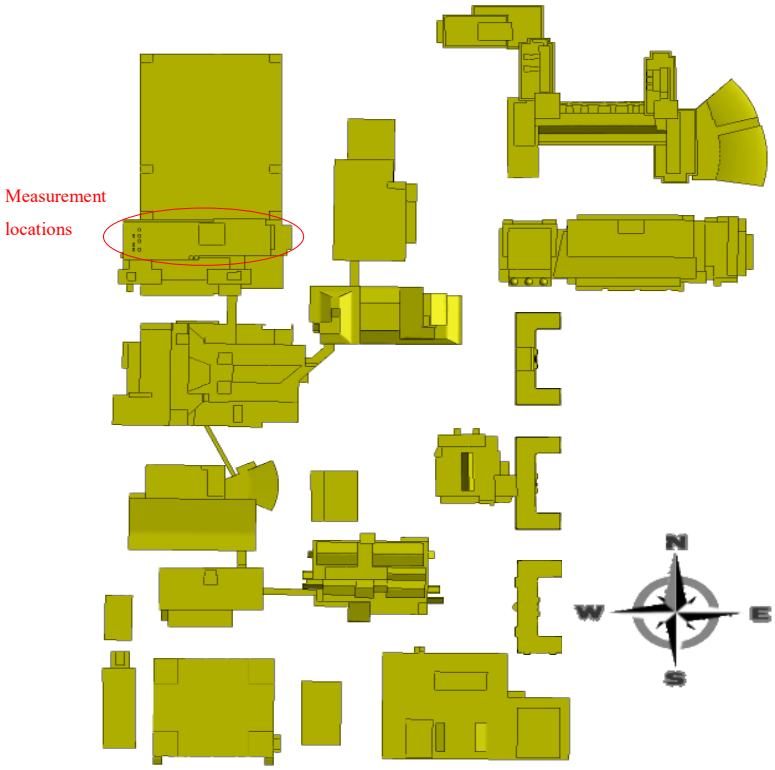

Figure 4-18: CFD geometry.

From our results, we can see that the validation methodology and the simulation can be considered valid, as we reached an acceptable agreement between the numerical and experimental results for the East and South directions. The average wind speed errors were 10.8% and 17.7%, respectively, and average wind direction deviations were 8.4° and 12.3°, respectively, with the standard deviation method. However, as the upstream geometry was not accurately modeled for the North and West winds, the average wind direction deviations were slightly higher, at 13.5° and 12.7°, respectively, along with higher errors between the simulated and measured wind speeds at 51.2% and 24.6%, respectively.

4.2 Results of Wind Resource Assessment

The daily mean wind speeds measured by each anemometer was plotted, along with the behavior at the reference Tory Weather Station (TWS), and the results are presented below. The results at location E were not assessed as the equipment seemed to be experiencing issues in data collection.

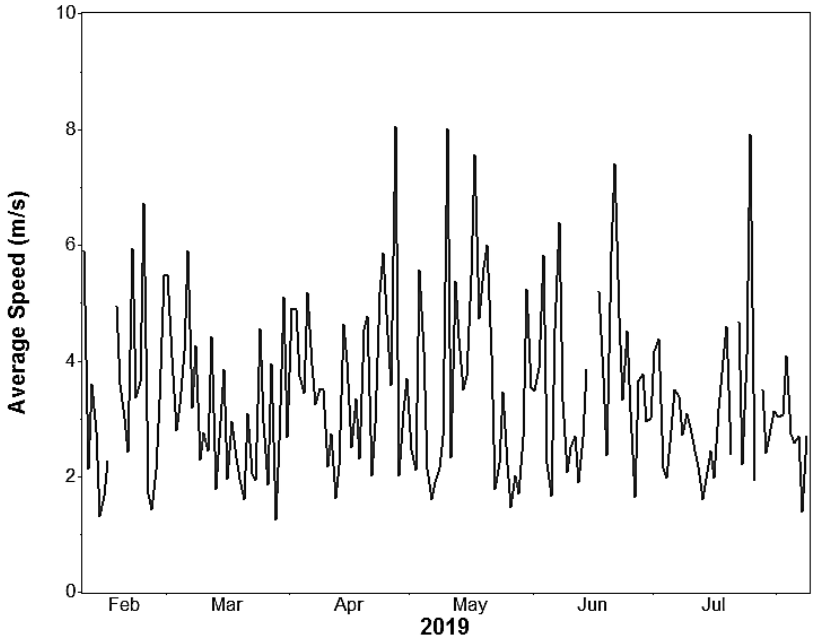

(a)

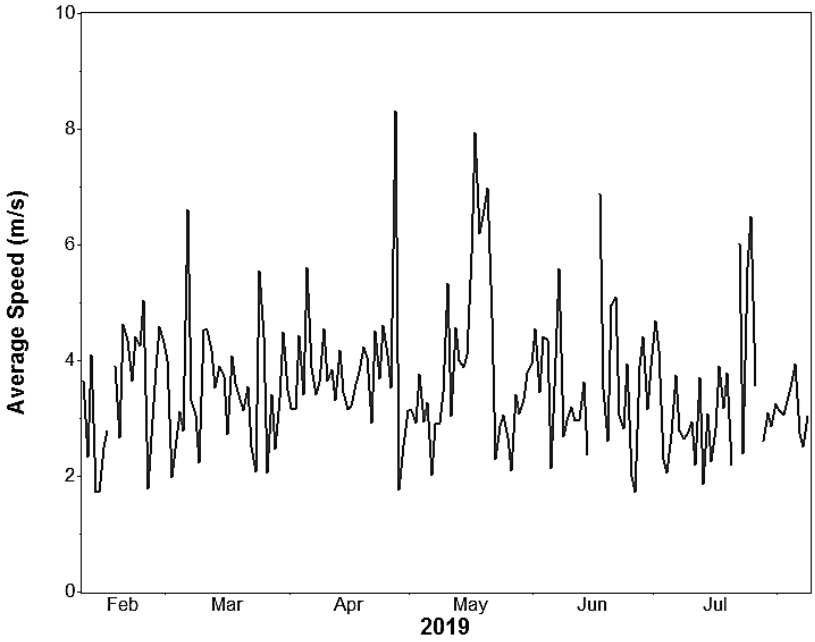

(b)

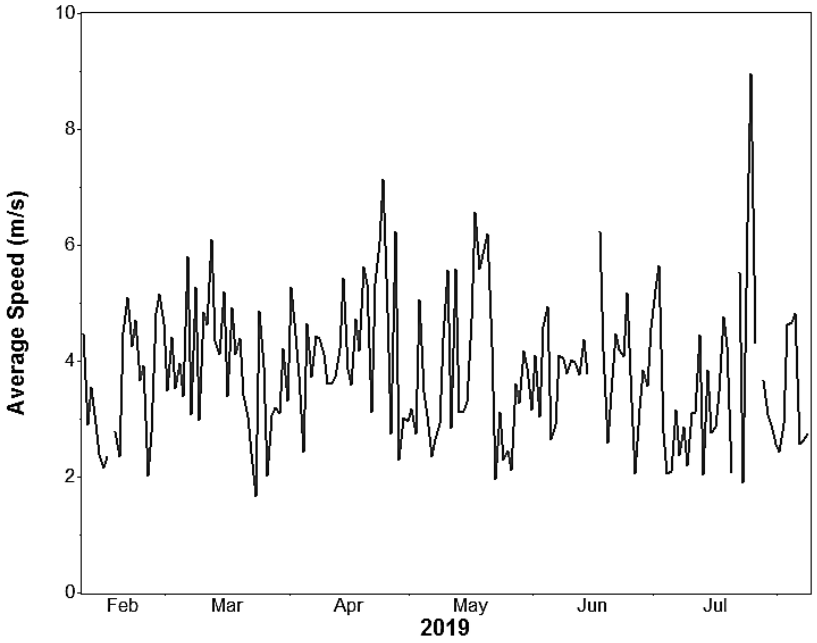

(c)

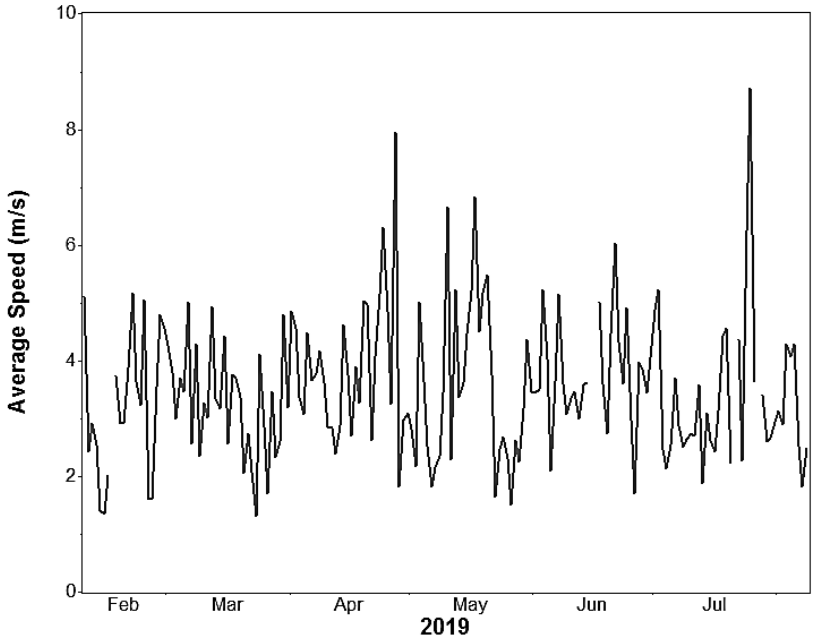

(d)

Figure 4-19: Daily mean wind speeds measured at location: (a) A, (b) B, (c) D, (d) Tory Weather Station.

Table 4-4 summarizes the main aspects of the plots shown above.

Table 4-4: Wind speed statistics for DICE and TWS between Feb 8th – Aug 8th 2019.

Location	Minimum (m/s)	Maximum (m/s)	Mean (m/s)	Standard Deviation (m/s)
A	1.262	8.056	3.407	2.009
B	1.738	8.328	3.602	1.686
D	1.673	8.976	3.845	1.741
TWS	1.320	8.712	3.519	1.738

The corresponding average daily wind power densities were also calculated and the results are shown in Figure 4-20 and Table 4-5 below.

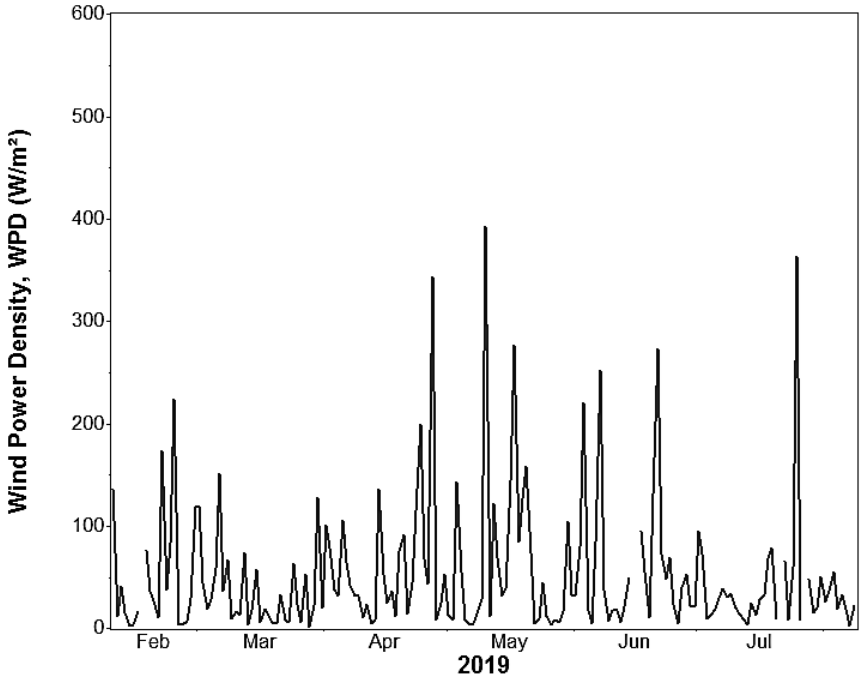

(a)

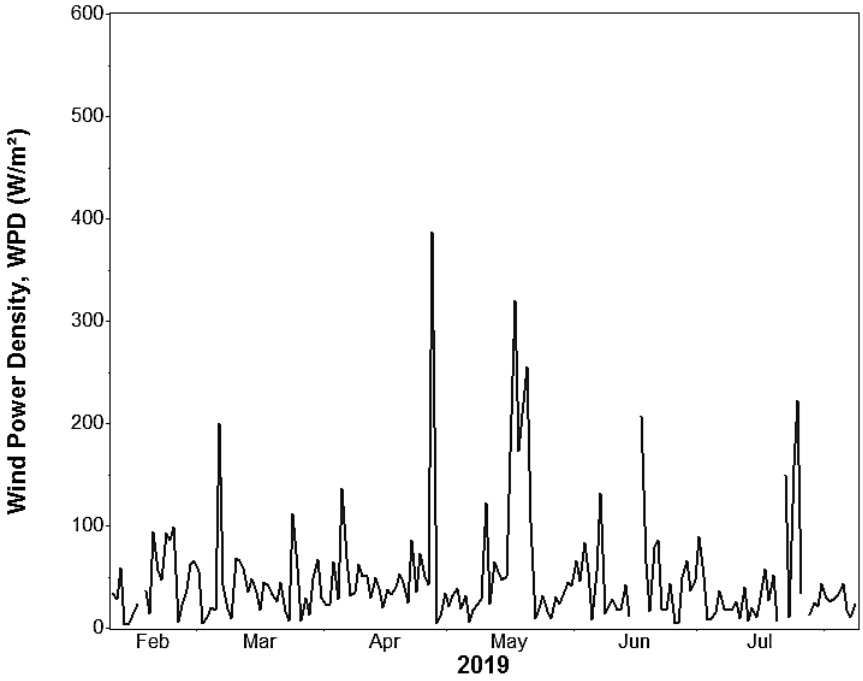
Wind Power Density, WPD (W/m²)
600
500
400
300
200
100
0
Feb
Mar
Apr
May
Jun
Jul
2019

(b)

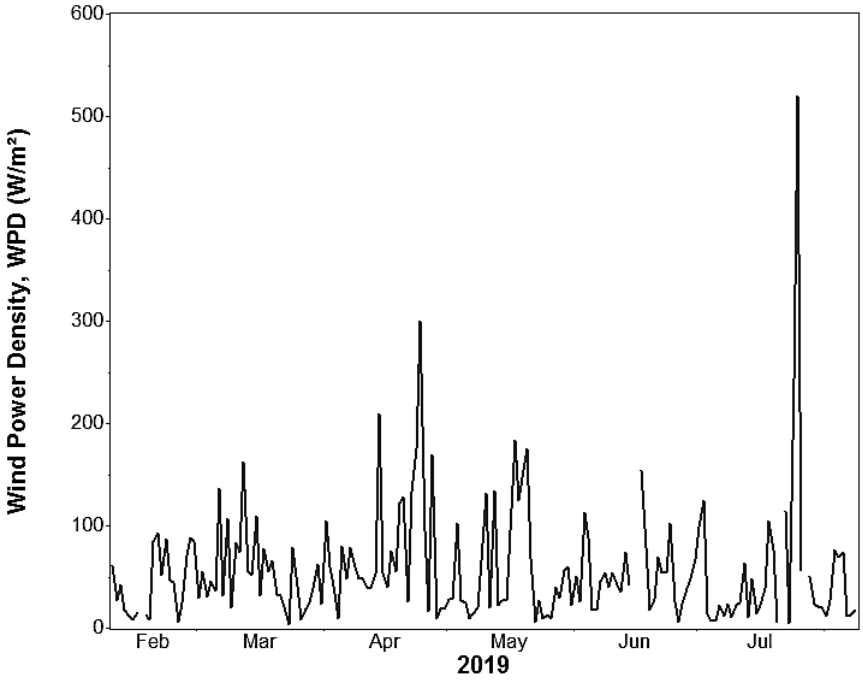
Wind Power Density, WPD (W/m²)
600
500
400
300
200
100
0
Feb
Mar
Apr
May
Jun
Jul
2019

(c)

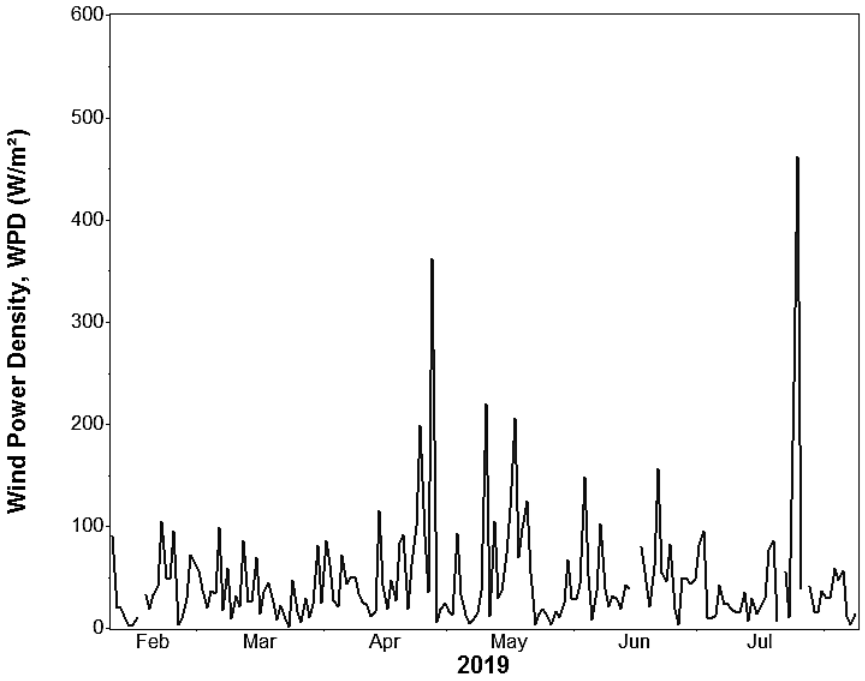

(d)

Figure 4-20: Daily mean wind power density measured at location: (a) A, (b) B, (c) D, (d) Tory Weather Station.

Table 4-5: Average wind power density over DICE and TWS for Feb 8th – Aug 8th 2019.

Location	Minimum (W/m^2)	Maximum (W/m^2)	Mean (W/m^2)	Standard Deviation (W/m^2)
A	2.30	393.56	54.09	46.65
B	3.56	387.33	49.78	41.85
D	4.35	521.16	58.59	48.75
TWS	2.11	462.49	48.49	42.90

Figure 4-19 shows that at all measurement locations, the anemometers are experiencing the same overall trends in wind behavior; however we can see that the measurements on DICE have a tendency to have higher average wind speeds than TWS. Despite location A showing the most peaks in wind speed, it has the lowest overall mean speed, and highest standard deviation, indicating that this location is the most prone to wind gusts. While the mean wind speed over DICE is slightly higher than the reference TWS, we see no signs of a clear "concentration effect," as described by Ayhan et al. [11], who assessed the wind flow over buildings of varying heights in an urban environment. This is likely due to the presence of the elevator penthouse on the roof of DICE, which can slow down the wind and cause areas of recirculation, as seen in

the previous section. The results show that overall, the wind power densities are very low over the DICE roof and at the TWS. The values correspond to wind power class 1, as the average WPD $< 200\ \mathrm{W/m^2}$, showing very poor wind power potential [29]. Wind power class is a number indicating the mean energy content of the wind resource. Wind power classes are based on the mean wind power density at 50 meters above ground.

The effect of changing averaging period was also analyzed, and the WPD for the month of March at location B was assessed with 3 different time periods. The results were plotted and shown in Figure 4-21.

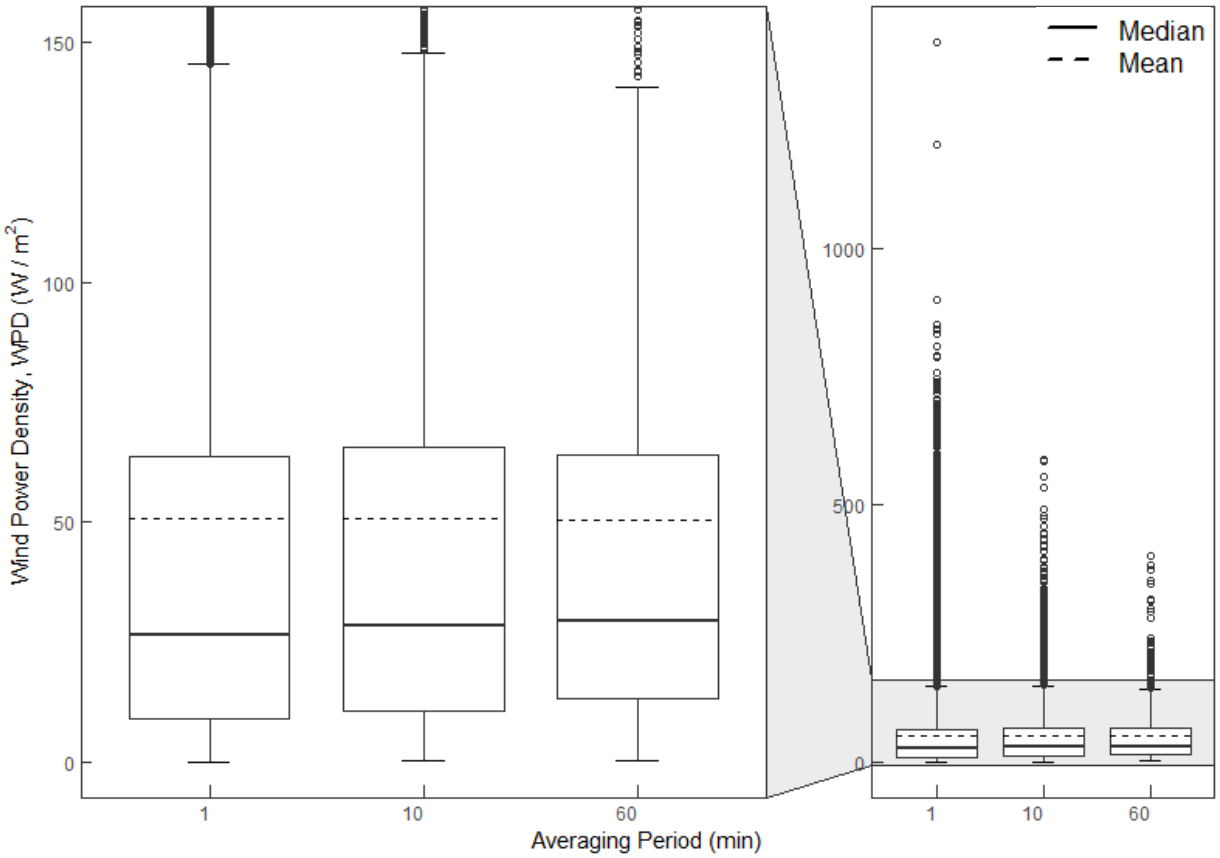

Figure 4-21: Effect of averaging period on WPD.

Figure 4-21 shows that the average value of WPD does not differ greatly with different averaging periods, with $50.59\ \mathrm{W/m^2}$, $50.59\ \mathrm{W/m^2}$, and $50.46\ \mathrm{W/m^2}$ for 1 min, 10 min, and 60 min averaging periods, respectively. We can see however, that as the period gets smaller, there are more frequent instances of short bursts of high power, that we could potentially capture with a turbine with a fast enough response time.

Weibull distributions were fit for the data and the results are shown in Figure 4-22 and Table 4-6.

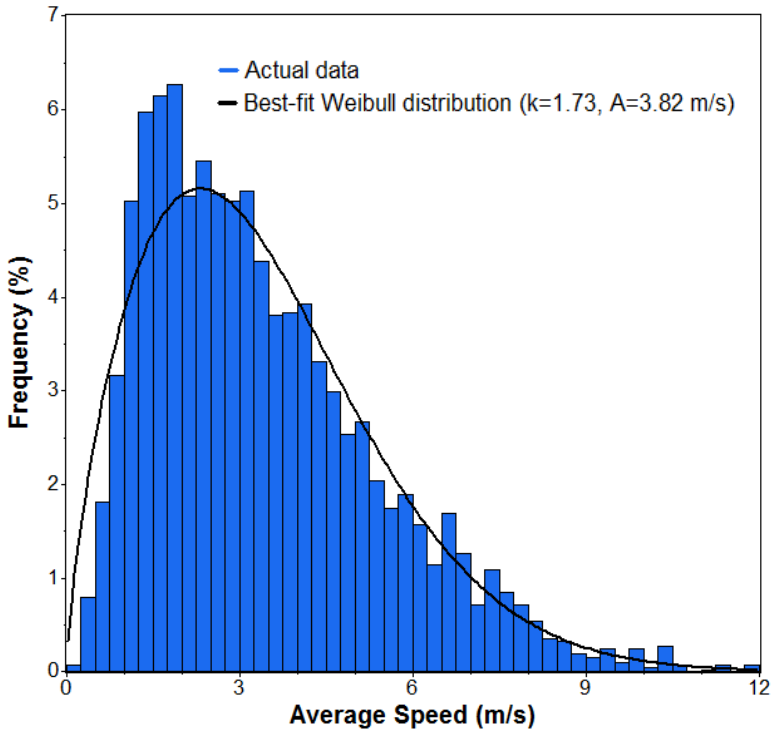
Actual data
Best-fit Weibull distribution (k=1.73, A=3.82 m/s)
Frequency (%)
Average Speed (m/s)
0
1
2
3
4
5
6
7
0
3
6
9
12

(a)

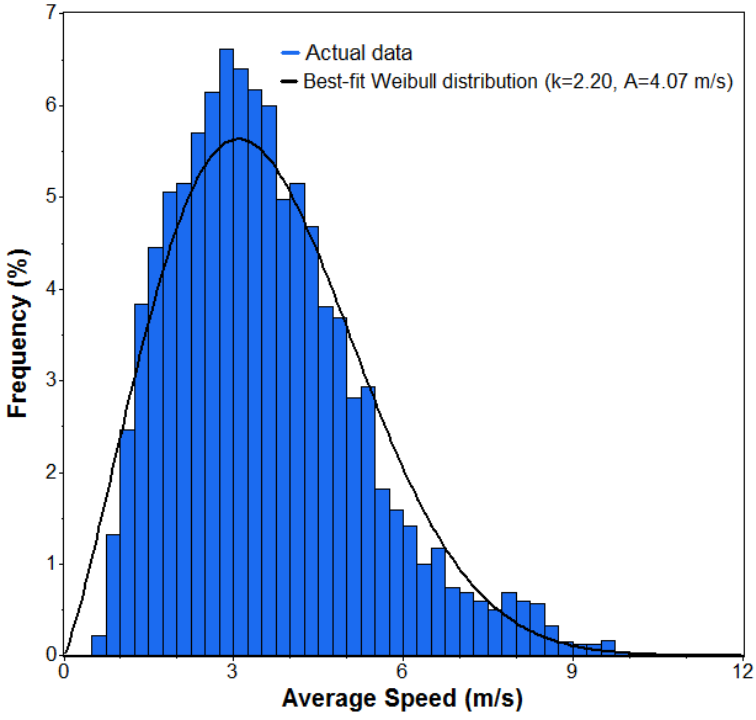
Actual data
Best-fit Weibull distribution (k=2.20, A=4.07 m/s)
Frequency (%)
Average Speed (m/s)
0
1
2
3
4
5
6
7
0
3
6
9
12

(b)

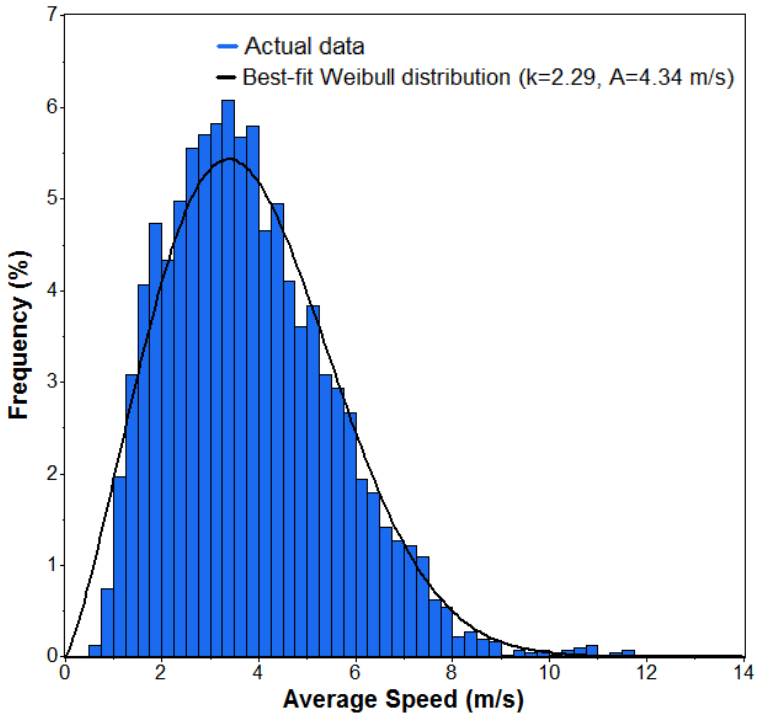

(c)

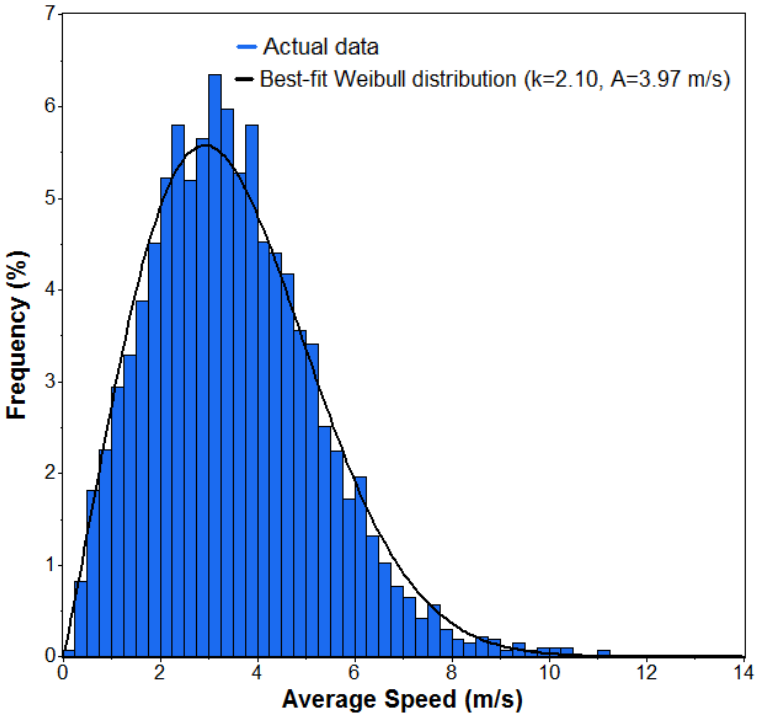

(d)

Figure 4-22: Weibull distribution fit for measurements at location: (a) A, (b) B, (c) D, (d) Tory Weather Station.

The most probable wind speed at each location was calculated based off the fitted Weibull distributions using the following equation:

$$V_{mp} = A\left(\frac{k-1}{k}\right)^{k^{-1}} \tag{4.1}$$

Table 4-6: Weibull parameters for wind over DICE and TWS between Feb 8th – Aug 8th 2019.

Location	Mean (m/s)	Weibull Shape Parameter, k	Weibull Scale Parameter, A (m/s)	Wind Power Density, WPD (W/m^2)	Most Probable Wind Speed, V_{mp} (m/s)	Proportion Above Actual Mean
A	3.42	1.732	3.82	52.7	2.33	0.447
B	3.61	2.203	4.07	49.0	3.09	0.470
D	3.85	2.291	4.34	57.9	3.38	0.472
TWS	3.52	2.100	3.97	48.0	2.92	0.462

Comparing Table 4-4, Table 4-5, and Table 4-6, shows that the Weibull distribution fits the measured data very well at all locations, with predicted mean wind speeds and wind power density values that are very similar. We can see that although the average wind speeds for the measured results are around $3.5\ m/s$, the most probable wind speed (and most frequent) is actually quite lower at all locations, with the biggest deviation being at location A, with a mean of $3.4\ m/s$ and a most probable speed of $2.33\ m/s$. This reinforces the initial assumption of location A experiencing the most gusty wind patterns. In addition, from the fitted distribution, we can see that the proportion of wind measurements that are above the mean of the actual data (found in Table 4-4) is lower than 50% at all locations, indicating that the majority of the measured data are under $3.5\ m/s$, and there are only short periods of time with wind speeds high enough to affect the mean.

To assess the most frequent wind direction and the average wind speed associated with that wind direction, wind roses were created and presented in Figure 4-23. We can see that the most common incident wind direction for locations A, D and TWS is North-West wind, with location B showing West winds as the most common. This is not surprising, because looking back to Figure 3-6, we can see that the elevator penthouse is directly North-West of the ultrasonic anemometer B, and will provide cover from any wind coming from that direction.

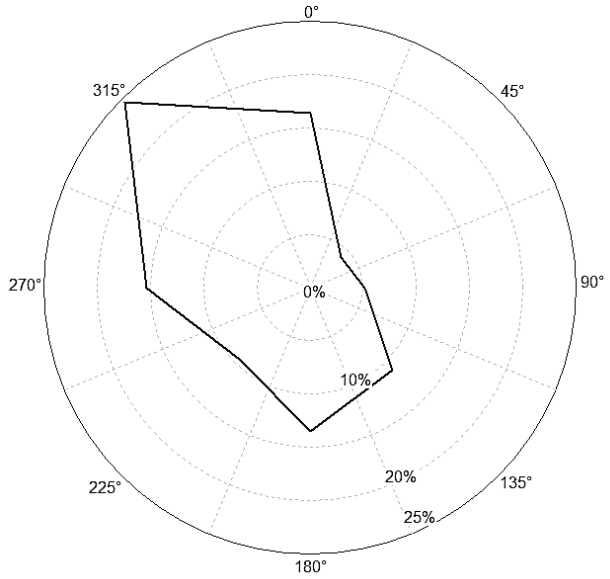
0°
45°
90°
135°
180°
225°
270°
315°
0%
10%
20%
25%

(a)

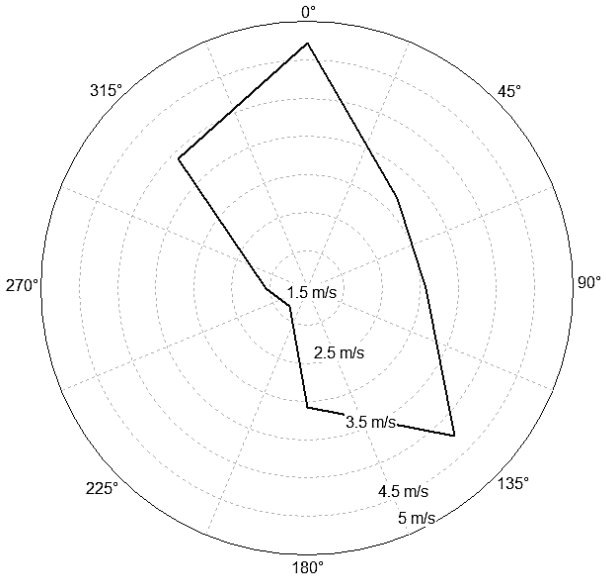
0°
45°
90°
135°
180°
225°
270°
315°
1.5 m/s
2.5 m/s
3.5 m/s
4.5 m/s
5 m/s

(b)

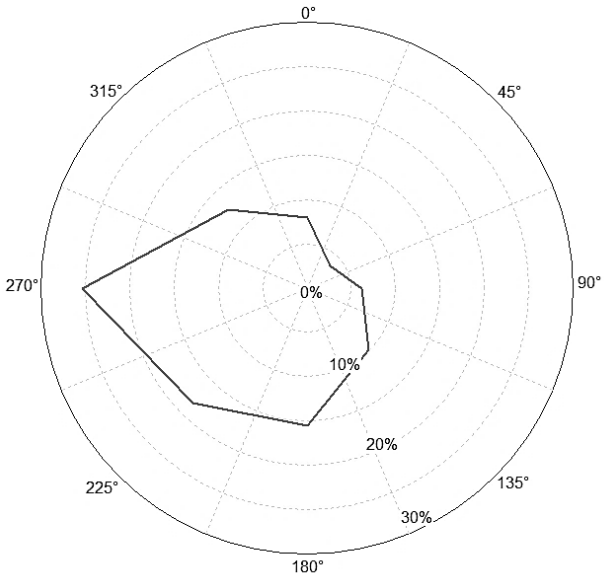
0°
45°
90°
135°
180°
225°
270°
315°
0%
10%
20%
30%

(c)

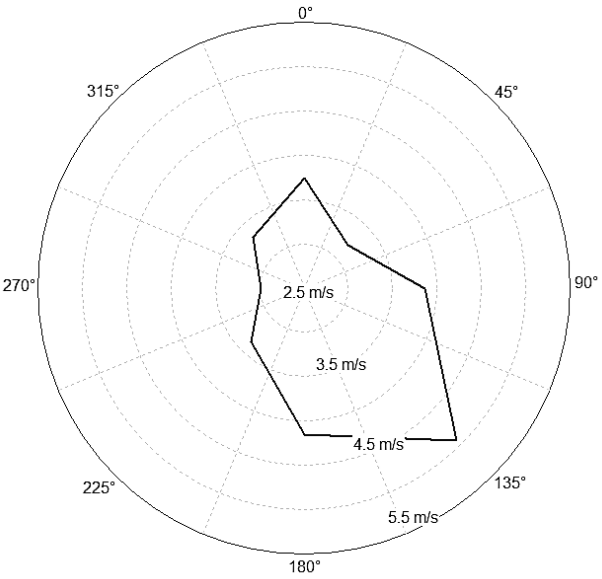
0°
45°
90°
135°
180°
225°
270°
315°
2.5 m/s
3.5 m/s
4.5 m/s
5.5 m/s

(d)

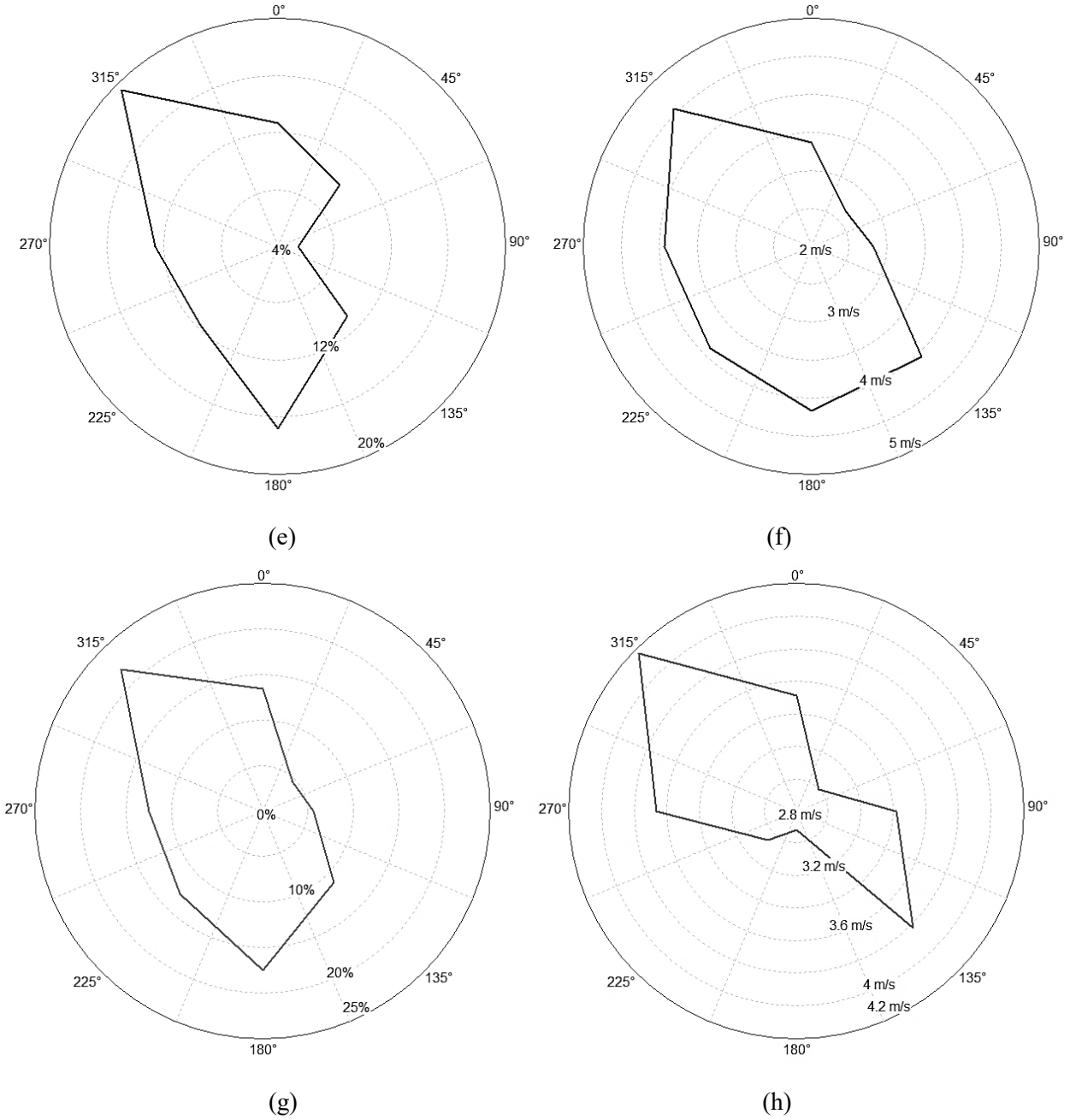

(e) (f)

(g) (h)

Figure 4-23: Frequency (left) and mean wind speed (right) wind roses for measurements at location: (a, b) A, (c, d) B, (e, f) D, (g, h) Tory Weather Station.

Locations A, D, and TWS also exhibit similar magnitudes the North-West wind direction, with all experiencing average speeds between $4 - 4.5\ \mathrm{m/s}$. Something interesting to note is that for winds from the South, both A and TWS experience winds with an average magnitude of around $3\ \mathrm{m/s}$, while B and D show peaks of around $4.2\ \mathrm{m/s}$. Location D also experiences relatively high speeds from winds coming

from the South-West. These could be attributed to a slight concentration effect for South winds as they would be experiencing the acceleration effects passing over the rows of buildings upstream. East is the least common wind direction, with less or around 5% at all locations, and then closely followed by North-East. From FiguresFigure 4-20 – Figure 4-23, it is clear that location D has the best agreement with the reference TWS measurements, in terms of wind speed, and consequently wind power density, and wind direction.

A turbulence assessment was conducted with the data from the ultrasonic anemometers at locations B and D. The turbulence intensities were calculated for each wind component, and different averaging periods were used, 10 minutes and 1 minute, and the differences between them were analyzed. The plots for the u-component of speed are presented in Figure 4-24 and Figure 4-25. The plots of the v and w components can be found in Appendix D.

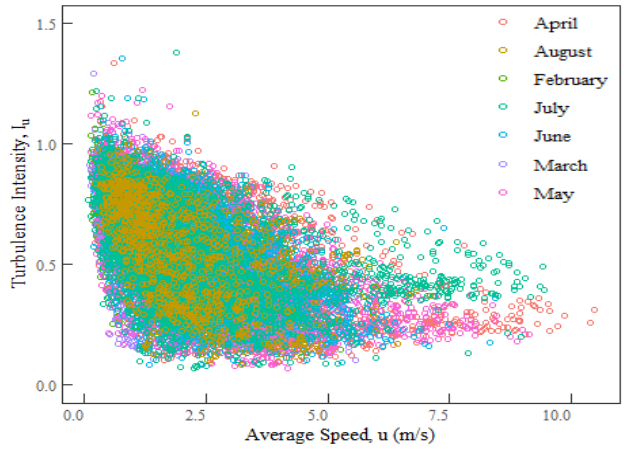

(a)

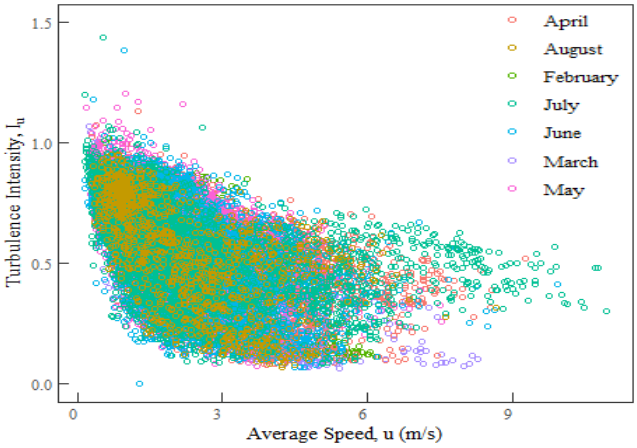

(b)

Figure 4-24: 10 minute averaged turbulence intensity at: (a) location B, (b) location D.

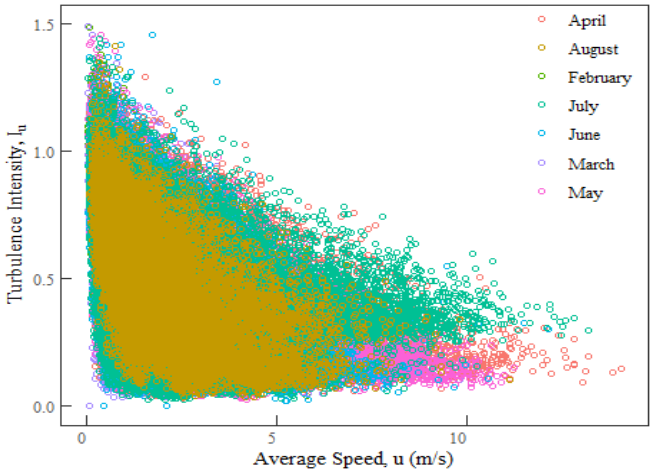

(a)

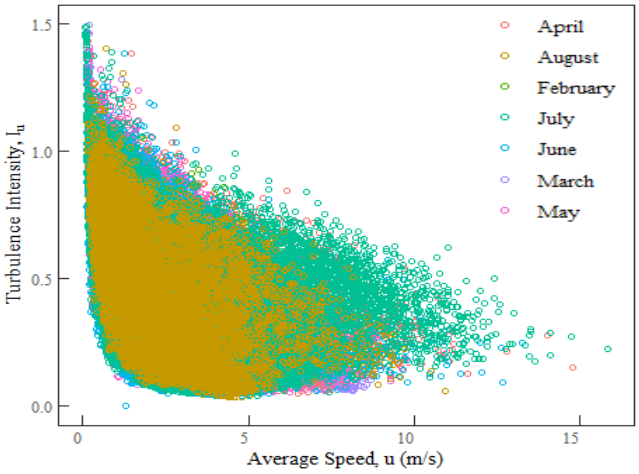

(b)

Figure 4-25: 1 minute averaged turbulence intensity at (a) location B, (b) location D.

A summary of the results of the turbulence study is presented below in Table 4-7.

Table 4-7: Effect of Averaging period on average turbulence intensity.

	B			D		
Period	Average I_u	Average I_v	Average I_w	Average I_u	Average I_v	Average I_w
10 Minutes	0.575	0.558	0.713	0.578	0.562	0.683
1 Minute	0.509	0.494	0.671	0.525	0.507	0.653

The figures show the expected trend of decreasing turbulence intensity with increasing wind speeds [64]. Both locations show results, suggesting that the entire roof is being subjected to the same turbulent regime. Turbulence intensity usually characterizes the high frequency of turbulence, and is a key aspect when it comes to assess a location for power production, since it has important effects on a wind turbine performance [13]. Turbulence affects the power output and increases fatigue loads on the turbines. And according to the National Renewable Energy Laboratory (NREL), acceptable values of turbulence intensity for setting urban wind turbines in terms of power production and fatigue loads, should be under 18% [65]. Our results show a very highly turbulent regime, indicating that these locations are not suitable for power production for traditional large Horizontal Axis Wind Turbines.

The results show 11.5%, 10.6%, and 5.9% decreases in I_u, I_v, and I_w, respectively, at location B, and 9.2%, 9.8% and 4.4% decreases in I_u, I_v, and I_w, respectively, at location D when the averaging period was decreased from 10 minutes to 1 minute. This shows that the horizontal components of the wind, u, and v, are more sensitive to time averaging than the vertical component, w.

Similar results were reported Tabrizi et al. [40], who found decreasing the averaging periods led to a decrease in the value of the calculated turbulence intensity. The authors found that the longitudinal and lateral turbulence intensities, I_u and I_v were reduced by 25% when the averaging period was reduced from 10 minutes to 1 minutes. The vertical turbulence intensity also exhibited similar behavior as our results, showing a lower reduction of 11% when the averaging period was reduced.

For a more illustrative approach, a 10 minute averaging period should be used when conducting a wind resource assessment to evaluate the suitability of a location for wind power production, as this would give a more representative value for turbulence intensity and ensure that if a turbine was installed, it could be designed to handle the turbulent loading and gusting [40].

Finally, an assessment was conducted to analyze the difference in turbulence intensity for wind coming from the North and wind coming from the South. The North wind is considerably less disturbed than that coming from the South, as located North of the DICE building are parks, homes, and the North Saskatchewan River, while South of DICE has several rows of buildings on campus. The month of March was analyzed at location B and the results are presented in Figure 4-26.

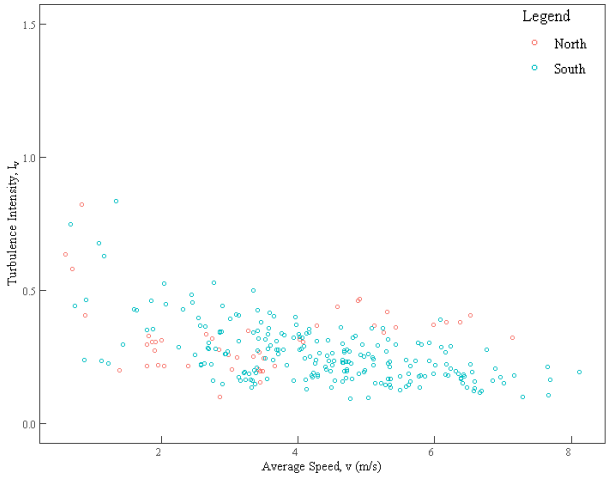

(a)

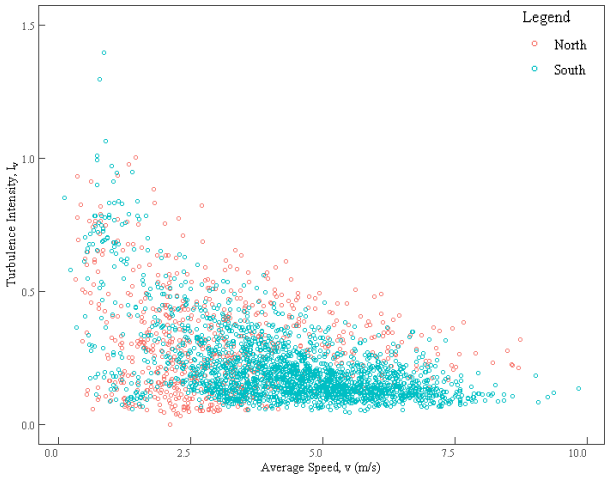

(b)

Figure 4-26: Effect of incident wind direction on lateral component of turbulence intensity, I_v, at location B with (a) 10 min averaging, (b) 1 min averaging.

It is clear from the figures that as the wind speed increases, the turbulence intensity for the wind coming from the North is higher than that coming from the South. This is likely attributed to the fact that the measurement location B is located in the wake of the leading edge, the North edge of DICE, and is likely within the recirculation zone. The measurement location is expected to be near the interface between the freestream and the boundary layer, where there are higher velocity fluctuations, and hence, higher turbulence intensities.

5. Conclusion

5.1 Summary

The goal of this thesis was to conduct an experimental measurement campaign to provide data for the creation of a framework for the validation of a CFD model assessing the rooftop wind regime around buildings of the University of Alberta North Campus. This CFD model can be used for wind turbine location siting for urban wind power generation, improving efficiency of HVAC systems, building and urban planning, and improving design of building exhaust stacks for better dispersion.

A review of relevant literature was conducted to assess the existing best practice guidelines for CFD validation, and to examine the studies that carried out validation of a CFD model. It was found that while there are many studies that use CFD for a wide variety of assessments (pedestrian wind safety, pollution dispersion, wind power potential, etc.), none outline the validation technique that was used, but only state that validation was conducted. This thesis aims to fill that gap, and present a detailed validation study, with a step by step guide.

To collect data, an experimental measurement campaign was first designed and installed on the roof of the Donadeo Innovation Centre for Engineering (DICE) building, which was the target of the CFD study. Four anemometers, two ultrasonic and two mechanical wind monitors, measuring at 15 Hz and 1 Hz, respectively, were set up around the building in a way that would allow us to get a more complete view of the wind flow around the building, so they were set up around the four corners of the roof, within a safe working distance of the West edge, due to the presence of some stacked solar panels. The anemometers were installed on 15 ft high masts. A data acquisition system was designed using the software LabVIEW. Measurements from the Tory Weather Station (TWS) on campus were used reference free stream data. Data were collected for six months, and were processed and analyzed using the statistical software RStudio. The data were averaged into one hour increments, to allow us to accurately compare with the TWS data, as it is hourly averaged and archived. One of the mechanical monitors was found to be experiencing some alignment issues, and was removed from the analysis.

Simulations were run for a range of wind speeds and directions, and two methods of data extraction were used. The first was a single point method, which extracted the values of the wind speed and direction at the exact location of the anemometers, and the second was a point cloud method, which consisted of extracting the values at 100 points on a 1 m x 1 m horizontal plane around the anemometer locations and determining the average values. It was found that there were only slight and insignificant differences between the two

methods, as our measurements were not within regions of high velocity gradients, and the single point method was considered adequate and was used in the remaining analysis.

The experimental data were filtered and placed into directional bins, and two methods were also used to compare with the numerical results. The first method was the standard deviation method, which used the measurement with the calmest winds (smallest standard deviation of the wind direction for the hourly average) to compare with the numerical results. The second method was the average method, which took the average of all measurements in each bin, and compared to the numerical results.

The standard deviation method was found to produce slightly better agreements between the numerical and experimental results more frequently than the average method as 15 of the 24 numerical deviations were better agreements with the measured values, most commonly for deviations in speed. The results of the validation found that model is in good agreement with the measured values for incident winds from the East and South, with average wind speed errors of 10.8% and 17.7%, and wind direction deviation of $8.4°$ and $12.3°$, respectively. However, the average wind direction deviations for the North and West incident winds were $13.5°$ and $12.7°$, respectively, and the errors between the simulated and measured wind speeds are 51.2% and 24.6%, respectively. The results show that the validation methodology that was presented in this work is valid, as we have reached acceptable agreements between the numerical and experimental results for the East and South directions. However, as the upstream geometry was not modeled in detail for the West and North directions, the errors were higher.

The average daily wind speeds, wind power densities and probability density functions for each measurement location were also determined. The average wind speeds were between $3.4 - 3.9\ \mathrm{m/s}$ and the corresponding wind power densities were between $48 - 59\ \mathrm{W/m^2}$ which is considered power class 1, and a poor location for wind power production. The results of the Weibull distribution showed that the most probable wind speeds are in the range $2.3 - 3.4\ \mathrm{m/s}$, with roughly 45% of the measured data with speeds above the mean. Wind roses were created for each location and predominant wind direction was found to be North-West.

The turbulent intensities were calculated and the effects of averaging time were assessed. The turbulence intensities were found to decrease with increasing wind speeds, as expected, and the average values of turbulence intensity were found to be between 55 – 72% at the first location, B, and between 56 – 68% at the second location, D, for all components, I_u, I_v, and I_w, with a 10 minute averaging period.

When the averaging period was decreased from 10 minutes to 1 minute, we saw 11.5%, 10.6%, and 5.9% decreases in I_u, I_v, and I_w, respectively, at location B, and 9.2%, 9.8% and 4.4% decreases in I_u, I_v, and I_w, respectively, at location D. This was consistent with what has been found in previous studies.

5.2 Future Work and Recommendations

Some recommendations and areas of improvements for this study are listed below:

- Data acquisition should be improved and should not rely on power supply from the building. A data acquisition system that has a backup power source is required as the power is frequently cycled in the building and the LabVIEW Virtual Instruments need to be rerun in order to continue collecting data.
- Ultrasonic anemometers should be used in place of mechanical wind monitors as they have no moving parts and do not need as frequent recalibration.
- Data should be collected for at least one year and a complete wind resource assessment should be conducted prior to running any simulations. The predominant and most frequent wind directions and speeds should be determined and the simulations should be run accordingly.
- Allowable range for measurement bins should be increased and validation assessment re-done. The effect on the validation of the model should be noted and the differences between strict acceptance criteria and lenient acceptance criteria should be studied.
- An anemometer should be set up on the DICE elevator penthouse to locally measure the reference free stream.
- The location at which the reference free stream measurements are being taken should be included in the CFD model and the numerical and experimental values should be compared.
- An averaging time of 10 minutes should be used, as 1 hour is too large to fully capture the inherent structures in the wind.
- Unsteady simulations should be run, and the differences between the unsteady and steady simulations should be assessed.

References

[1] M. Roser, H. Ritchie, and E. Ortiz-Ospina, "Our World in Data." [Online]. Available: https://ourworldindata.org/world-population-growth. [Accessed: 20-May-2019].

[2] ExxonMobil, "2018 Outlook for Energy: A View to 2040," 2018.

[3] UNFCCC. Conference of the Parties (COP), "ADOPTION OF THE PARIS AGREEMENT - Conference of the Parties COP 21," 2015.

[4] C. Period *et al.*, "Ontario Rebate for Electricity Consumers Act , 2016," vol. 22, no. c, pp. 1–11, 2019.

[5] Hydro-Quebec, "Net Metering Rate Option for Self-Generators," 2019.

[6] B. Hydro, "Our distributed generation programs," 2019.

[7] E. U. Act, "MICRO-GENERATION REGULATION," 2018.

[8] Alberta Electric System Operator, "Micro-generation in Alberta," 2018.

[9] K. Ohlenforst *et al.*, "Global Wind report 2018," 2019.

[10] X. Lu and M. B. McElroy, "Global Potential for Wind-Generated Electricity," *Wind Energy Eng. A Handb. Onshore Offshore Wind Turbines*, vol. 106, no. 27, pp. 51–73, 2017.

[11] D. Ayhan and A. Sağlam, "A technical review of building-mounted wind power systems and a sample simulation model," *Renew. Sustain. Energy Rev.*, vol. 16, no. 1, pp. 1040–1049, 2012.

[12] M. Versteege and S. Leblanc, "Energy Reduction Master Plan 2017-2020," 2017.

[13] S. Emeis, *Wind Energy Meteorology Atmospheric Physics for Wind Power Generation*, Second Edi. 2018.

[14] L. Landberg, *METEOROLOGY FOR WIND ENERGY*. Springer, 2016.

[15] R. B. Stull, *An Introduction to Boundary Layer Meteorology*. Kluwer Academic Publishers, 1988.

[16] T. Kershaw, *Climate Change Resilience in the Urban Environment*. IOP, 2017.

[17] S. L. Walker, "Building mounted wind turbines and their suitability for the urban scale — A review of methods of estimating urban wind resource," *Energy Build.*, vol. 43, no. 8, pp. 1852–1862, 2011.

[18] X. I. A. Yang, J. Sadique, R. Mittal, and C. Meneveau, “Exponential roughness layer and analytical model for turbulent boundary layer flow over rectangular-prism roughness elements,” pp. 127–165, 2016.

[19] D. Micallef and G. van Bussel, “A Review of Urban Wind Energy Research: Aerodynamics and Other Challenges,” *Energies*, vol. 11, no. 9, p. 2204, 2018.

[20] R. W. Macdonald, “MODELLING THE MEAN VELOCITY PROFILE IN THE URBAN,” pp. 25–45, 2000.

[21] D. Jiang, W. Jiang, H. Liu, and J. Sun, “Systematic influence of different building spacing, height and layout on mean wind and turbulent characteristics within and over urban building arrays,” *Wind Struct. An Int. J.*, vol. 11, no. 4, pp. 275–289, 2008.

[22] L. Jian-Zhong, L. Hui-Jun, and Z. Kai, “New expressions for the surface roughness length and displacement height in the atmospheric boundary layer,” *Chinese Phys.*, vol. 16, no. 7, pp. 2033–2039, 2007.

[23] H. Tennekes and J. L. Lumley, *A FIRST COURSE IN TURBULENCE*. The MIT Press, 1972.

[24] H K Versteeg and W. Malalasekera, *Introduction to Computational Fluid Dynamics*, Second Edi., vol. M. 2012.

[25] G. Ren, J. Liu, J. Wan, F. Li, Y. Guo, and D. Yu, “The analysis of turbulence intensity based on wind speed data in onshore wind farms,” *Renew. Energy*, vol. 123, pp. 756–766, 2018.

[26] D. Wood, *Small Wind Turbines: Analysis, Design, and Application*. Springer, 2011.

[27] “Weibull Distribution,” 2019. .

[28] S. Mathew, *Wind Energy Fundamentals, Resource Analysis and Economics*. Springer Netherlands, 2006.

[29] D. L. Elliott, C. G. Holladay, W. R. Barchet, H. P. Foote, and W. F. Sandusky, “Wind Energy Resourse Atlas of the United States,” 1986.

[30] A. N. Celik, “A statistical analysis of wind power density based on the Weibull and Rayleigh models at the southern region of Turkey,” *Renew. Energy*, vol. 29, no. 4, pp. 593–604, 2004.

[31] ANSYS Inc., “11.2.2. Linear Equation Solution,” 2019.

[32] M. A. Mohamed and D. H. Wood, “Computational modeling of wind flow over the University of Calgary campus,” *Wind Eng.*, vol. 40, no. 3, pp. 228–249, 2016.

[33] B. Blocken, “50 years of Computational Wind Engineering: Past, present and future,” *J. Wind Eng. Ind. Aerodyn.*, vol. 129, pp. 69–102, 2014.

[34] T. Simões and A. Estanqueiro, “A new methodology for urban wind resource assessment,” *Renew. Energy*, vol. 89, pp. 598–605, 2016.

[35] M. B. Tadie Fogaing, H. Gordon, C. F. Lange, D. H. Wood, and B. A. Fleck, “A Review of Wind Energy Resource Assessment in the Urban Environment,” in *Advances in Sustainable Energy*, A. Vasel and D. S.-K. Ting, Eds. Cham: Springer International Publishing, 2019, pp. 7–36.

[36] B. Blocken and J. Persoon, “Pedestrian wind comfort around a large football stadium in an urban environment: CFD simulation, validation and application of the new Dutch wind nuisance standard,” *J. Wind Eng. Ind. Aerodyn.*, vol. 97, no. 5–6, pp. 255–270, 2009.

[37] A. Kalmikov, G. Dupont, K. Dykes, and C. Chan, “Wind power resource assessment in complex urban environments : MIT campus case-study using CFD Analysis,” *AWEA 2010 Wind. Conf.*, p. 2010, 2010.

[38] B. Blocken, W. D. Janssen, and T. van Hooff, “CFD simulation for pedestrian wind comfort and wind safety in urban areas: General decision framework and case study for the Eindhoven University campus,” *Environ. Model. Softw.*, vol. 30, pp. 15–34, 2012.

[39] A. B. Tabrizi, J. Whale, T. Lyons, and T. Urmee, “Performance and safety of rooftop wind turbines: Use of CFD to gain insight into inflow conditions,” *Renew. Energy*, vol. 67, pp. 242–251, 2014.

[40] A. B. Tabrizi, J. Whale, T. Lyons, and T. Urmee, “Rooftop wind monitoring campaigns for small wind turbine applications: Effect of sampling rate and averaging period,” *Renew. Energy*, vol. 77, pp. 320–330, 2015.

[41] B. Blocken, A. van der Hout, J. Dekker, and O. Weiler, “CFD simulation of wind flow over natural complex terrain: Case study with validation by field measurements for Ria de Ferrol, Galicia, Spain,” *J. Wind Eng. Ind. Aerodyn.*, vol. 147, pp. 43–57, 2015.

[42] A. Z. Dhunny, F. Toja-Silva, C. Peralta, M. R. Lollchund, and S. D. D. V. Rughooputh, “Computational fluid dynamics simulation and full-scale experimental model inter-comparison of the wind flow around a university campus,” *Wind Eng.*, vol. 41, no. 1, pp. 43–54, 2017.

[43] B. W. Yan and Q. S. Li, “Coupled on-site measurement/CFD based approach for high-resolution wind resource assessment over complex terrains,” *Energy Convers. Manag.*, vol. 117, pp. 351–366, 2016.

[44] A. S. Yang, Y. M. Su, C. Y. Wen, Y. H. Juan, W. S. Wang, and C. H. Cheng, “Estimation of wind power generation in dense urban area,” *Appl. Energy*, vol. 171, pp. 213–230, 2016.

[45] A. Z. Dhunny, M. R. Lollchund, and S. D. D. V. Rughooputh, “Wind energy evaluation for a highly complex terrain using Computational Fluid Dynamics (CFD),” *Renew. Energy*, vol. 101, pp. 1–9, 2017.

[46] S. Liu *et al.*, “Influence of surrounding buildings on wind flow around a building predicted by CFD simulations,” *Build. Environ.*, vol. 140, no. May, pp. 1–10, 2018.

[47] Q. Wang, J. Wang, Y. Hou, R. Yuan, K. Luo, and J. Fan, “Micrositing of roof mounting wind turbine in urban environment: CFD simulations and lidar measurements,” *Renew. Energy*, vol. 115, pp. 1118–1133, 2018.

[48] X. Y. Tang, S. Zhao, B. Fan, J. Peinke, and B. Stoevesandt, “Micro-scale wind resource assessment in complex terrain based on CFD coupled measurement from multiple masts,” *Appl. Energy*, vol. 238, no. August 2018, pp. 806–815, 2019.

[49] Y. Toparlar *et al.*, “CFD simulation and validation of urban microclimate: A case study for Bergpolder Zuid, Rotterdam,” *Build. Environ.*, vol. 83, pp. 79–90, 2015.

[50] J. Franke, M. Sturm, and C. Kalmbach, “Validation of OpenFOAM 1.6.x with the German VDI guideline for obstacle resolving micro-scale models,” *J. Wind Eng. Ind. Aerodyn.*, vol. 104–106, pp. 350–359, 2012.

[51] M. B. T. Fogaing, J. Yalchin, S. Shadpey, C. F. Lange, and A. Fleck, “Numerical assessment of rooftop wind regime around buildings in a complex urban environment,” pp. 0–7.

[52] 3D Warehouse, “3D Warehouse,” 2018. [Online]. Available: https://3dwarehouse.sketchup.com/. [Accessed: 11-Feb-2018].

[53] ANSYS Inc., “Quick (Delaunay),” 2019.

[54] P. J. Richards and R. P. Hoxey, “Appropriate boundary conditions for computational wind engineering models using the k-ε{lunate} turbulence model,” *J. Wind Eng. Ind. Aerodyn.*, vol. 46–

47, no. C, pp. 145–153, 1993.

[55] J. Franke, A. Hellsten, H. Schlünzen, and B. Carissimo, *Guideline for the CFD Simulation of Flows in the Urban Environment: COST Action 732 Quality Assurance and Improvement of Microscale Meteorological*, no. May. 2007.

[56] G. Kelton and P. Bricout, "Wind Velocity Measurements Using Sonic Techniques," *Bull. Am. Meteorol. Soc.*, vol. 45, no. 9, pp. 571–580, 1964.

[57] C. Woodford, "Anemometers," 2009. [Online]. Available: https://www.explainthatstuff.com/anemometers.html. [Accessed: 27-Jul-2019].

[58] U. of M. Center for Atmospheric Science, "Sonic Anemometers." [Online]. Available: http://www.cas.manchester.ac.uk/restools/instruments/meteorology/sonic/. [Accessed: 27-Jul-2019].

[59] A. Weather, "R M Young Company 09101 WIND MONITOR - SE." .

[60] RStudio, "RStudio," 2019. [Online]. Available: https://www.rstudio.com/. [Accessed: 11-Sep-2019].

[61] Windographer, "Windographer," 2019. [Online]. Available: https://www.windographer.com/. [Accessed: 11-Sep-2019].

[62] Tecplot, "Tecplot 360," 2019. [Online]. Available: https://www.tecplot.com/products/tecplot-360/. [Accessed: 11-Sep-2019].

[63] Q. Chen, "Using computational tools to factor wind into architectural environment design," *Energy Build.*, vol. 36, no. 12, pp. 1197–1209, 2004.

[64] B. R. Karthikeya, P. S. Negi, and N. Srikanth, "Wind resource assessment for urban renewable energy application in Singapore," *Renew. Energy*, vol. 87, pp. 403–414, 2016.

[65] J. Fields, F. Oteri, R. Preus, and I. Baring-Gould, "Deployment of Wind Turbines in the Built Environment: Risks, Lessons, and Recommended Practices," no. June, p. 46, 2016.

Appendix A

Richardson Number Calculation

To ensure the simulation could be treated as isothermal the bulk Richardson number was calculated. However, as we did not have measurements at different heights on the DICE building, two values of the bulk Richardson number were calculated, one with a maximum possible shear gradient, taking measurements at the DICE building and at the Tory Weather Station, and another with a maximum possible temperature gradient, assuming that DICE is in an open undisturbed space, and using the measurements taken at DICE and the Edmonton International Airport. As our measurements are not at either end of these extremities, we expect the Richardson number at DICE to be within this range.

The equation for bulk Richardson number is:

$$Ri_b = \frac{g\Delta\Theta_v\Delta z}{\Theta_v[\Delta u^2 + \Delta v^2]}$$

Where Δz is a chosen height interval and $\Delta\Theta_v$ is the virtual potential temperature difference within this height interval, and Δu and Δv are the East-West and North-South velocity differences in the interval, respectively. The virtual potential temperature is the temperature that dry air must have to equal the density of moist air at the same pressure. This means that variations of virtual temperature can be studied in place of variations in density [15]. The virtual potential temperature is defined as:

$$\Theta_v = \Theta(1 + 0.609q)$$

Where q is the specific humidity, and Θ is the potential temperature, $\Theta = T\left(\frac{P_o}{P}\right)^{0.286}$, and P is air pressure, T is temperature, and P_o is a reference pressure usually set to $100\ kPa$.

<u>For a maximum shear gradient</u>

Tory Data:

$T = 29.68$ °C, $R_H = 17.27\%$, $P = 100.7$ kPa, $q = 4.46$ g/kg, $u = 2.312$ m/s, $v = -1.068$ m/s.

$$\Theta = (29.68 + 273.15\ \text{K})\left(\frac{100\ \text{kPa}}{100.7\ \text{kPa}}\right)^{0.286} = 302.226\ \text{K}$$

$$\Theta_v = 302.226\ \text{K}(1 + 0.609(4.46\ \text{g/kg} * 0.001\ \text{kg/g})) = 303.048\ \text{K}$$

DICE Data:

$T = 29.2\ ℃$, $R_H = 17.27\%$, $P = 100.7\ \text{kPa}$, $q = 4.33\ \text{g/kg}$, $u = 2.452\ \text{m/s}$, $v = 0.730\ \text{m/s}$.

$$\Theta = (29.2 + 273.15\ \text{K})\left(\frac{100\ \text{kPa}}{100.7\ \text{kPa}}\right)^{0.286} = 301.745\ \text{K}$$

$$\Theta_\text{v} = 301.745\ \text{K}\big(1 + 0.609(4.33\text{g/kg} * 0.001\text{kg/g})\big) = 302.541\ \text{K}$$

$$\text{Ri}_\text{B} = \frac{9.81\text{m/s} * (302.541\ \text{K} - 303.047\ \text{K}) * (68 - 64\ \text{m})}{303.047\ \text{K}[(2.452\ \text{m/s} - 2.312\ \text{m/s})^2 + (0.730\text{m/s} - -1.068\ \text{m/s})^2]} = -0.0119$$

For a maximum temperature gradient

Airport Data:

$T = 29.7\ ℃$, $R_H = 21\%$, $P = 92.35\ \text{kPa}$, $q = 5.92\ \text{g/kg}$, $u = -4.103\ \text{m/s}$, $v = 0.724\ \text{m/s}$.

$$\Theta = (29.7 + 273.15\ \text{K})\left(\frac{100\ \text{kPa}}{92.35\ \text{kPa}}\right)^{0.286} = 309.822\ \text{K}$$

$$\Theta_\text{v} = 309.822\ \text{K}(1 + 0.609(5.92\ \text{g/kg} * 0.001\ \text{kg/g})) = 310.939\ \text{K}$$

DICE Data:

$T = 29.2\ ℃$, $R_H = 17.27\%$, $P = 100.7\ \text{kPa}$, $q = 4.33\ \text{g/kg}$, $u = 2.452\ \text{m/s}$, $v = 0.730\ \text{m/s}$.

$$\Theta = (29.2 + 273.15\ \text{K})\left(\frac{100\ \text{kPa}}{100.7\ \text{kPa}}\right)^{0.286} = 301.745\ \text{K}$$

$$\Theta_\text{v} = 301.745\ \text{K}\big(1 + 0.609(4.33\text{g/kg} * 0.001\text{kg/g})\big) = 302.541\ \text{K}$$

$$\text{Ri}_\text{B} = \frac{9.81\text{m/s} * (302.541\ \text{K} - 310.939\ \text{K}) * (68\ \text{m} - 78\ \text{m})}{310.939\ \text{K}[(2.452\text{m/s} - -4.103\ \text{m/s})^2 + (0.730\text{m/s} - 0.724\ \text{m/s})^2]} = 0.0617$$

As both of these values are $\ll 1$, the buoyancy term is considered to be insignificant, and the flow is shear driven.

Appendix B

Anemometer Specifications

Ultrasonic Anemometer Model 81000

WIND SPEED

Range:	0 to 40 m/s (0 to 90 mph)
Resolution:	0.01 m/s
Threshold:	0.01 m/s
Accuracy:	±1% rms ±0.05 m/s (0 to 30 m/s)
	±3% rms (30 to 40 m/s)

WIND DIRECTION

Azimuth Range:	0.0 to 359.9 degrees
Elevation Range:	±60.0 degrees
Resolution:	0.1 degree
Accuracy:	±2° (1 to 30 m/s)
	±5° (30 to 40 m/s)

SPEED OF SOUND

Range:	300 to 360 m/s
Resolution:	0.01 m/s
Accuracy:	±0.1% rms ±0.05 m/s (0 to 30 m/s wind)

SONIC TEMPERATURE

Range:	-50 to +50 ºC
Resolution:	0.01 ºC
Accuracy:	± 2 ºC (0 to 30 m/s wind)

VOLTAGE OUTPUT (4 CHANNELS)

Range:	0 to 5000 mV
Resolution:	12 Bit
Accuracy:	± 0.1% of full scale

GENERAL

Air sample column:	10 cm high X 10 cm diameter
Air sample path:	15 cm
Output rate:	4 to 32 Hz (selectable)
Output formats:	Serial data (selectable)
	RS-232 and RS-485
Baud Rates:	1200 to 38400
Power Supply:	12 to 24 VDC, 110 mA
Dimensions:	Overall height 56 cm
	Support arm radius 17 cm
	Mounting 34 mm (1.34 in) diameter
	(standard 1 inch pipe)
Weight:	Sensor weight 1.7 kg (3.8 lb)

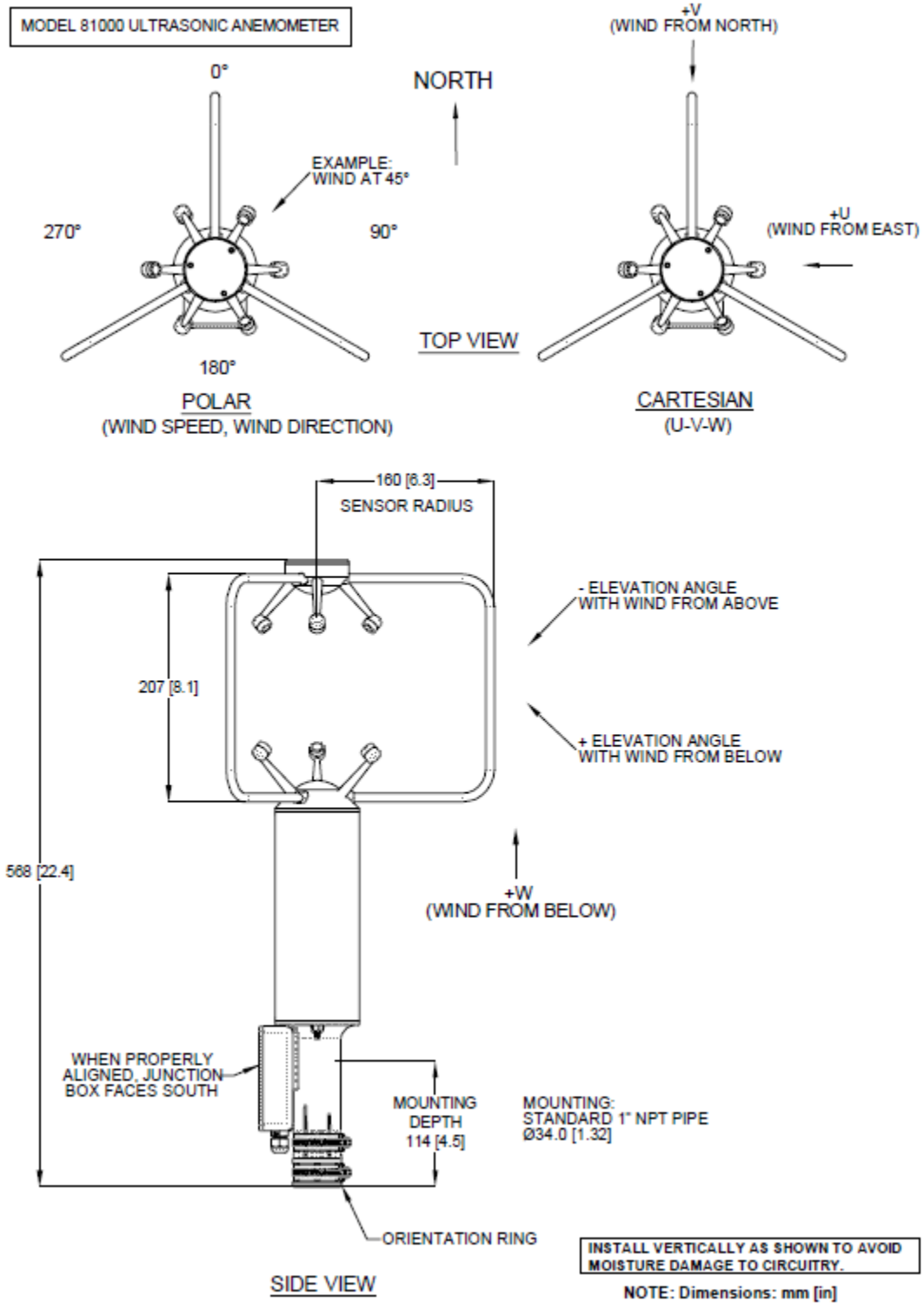
MODEL 81000 ULTRASONIC ANEMOMETER
0°
NORTH
EXAMPLE:
WIND AT 45°
270°
90°
180°
TOP VIEW
POLAR
(WIND SPEED, WIND DIRECTION)
+V
(WIND FROM NORTH)
+U
(WIND FROM EAST)
CARTESIAN
(U-V-W)
160 [6.3]
SENSOR RADIUS
207 [8.1]
- ELEVATION ANGLE
WITH WIND FROM ABOVE
+ ELEVATION ANGLE
WITH WIND FROM BELOW
568 [22.4]
+W
(WIND FROM BELOW)
WHEN PROPERLY
ALIGNED, JUNCTION
BOX FACES SOUTH
MOUNTING
DEPTH
114 [4.5]
MOUNTING:
STANDARD 1" NPT PIPE
Ø34.0 [1.32]
ORIENTATION RING
SIDE VIEW
INSTALL VERTICALLY AS SHOWN TO AVOID
MOISTURE DAMAGE TO CIRCUITRY.
NOTE: Dimensions: mm [in]

WIND SPEED SPECIFICATION SUMMARY

Range	0 to 100 m/s (224 mph)
Resolution:	0.1 unit
Accuracy:	±0.3 m/s (0.6 mph) or 1% of reading
Threshold:	1.0 m/s (2.2 mph)
Distance constant:	2.7 m (8.9 ft)
Transducer:	Rotating magnet and stationary coil.

WIND DIRECTION (AZIMUTH) SPECIFICATION SUMMARY

Range:	0-360 degrees
Accuracy:	± 2 degrees
Resolution:	1 degree
Threshold:	1.1 m/s (2.5 mph) @ 10° displacement
Delay distance:	1.3 m (4.3 ft)
Damping ratio:	0.3
Transducer:	Absolute encoder

GENERAL

Power requirement:	11-24 VDC, 20 mA
Dimensions:	Overall height 37 cm Overall length 55 cm Propeller 18 cm diameter Mounting 34 mm (1.34 in) diameter (standard 1 inch pipe)
Weight:	Sensor weight 1.0 kg (2.2 lb) Shipping weight 2.3 kg (5.0 lb)
Voltage Output:	WS: 0-5 VDC for 0-100 m/s WD: 0-5 VDC for 0-540°
Serial RS-485:	2 wire-half duplex, 1200-9600 Baud RMY, NCAR, NMEA, or RMYT protocols Polled or continuous
Operating Temperature:	-50 to 50°C (-58 to 122°F)

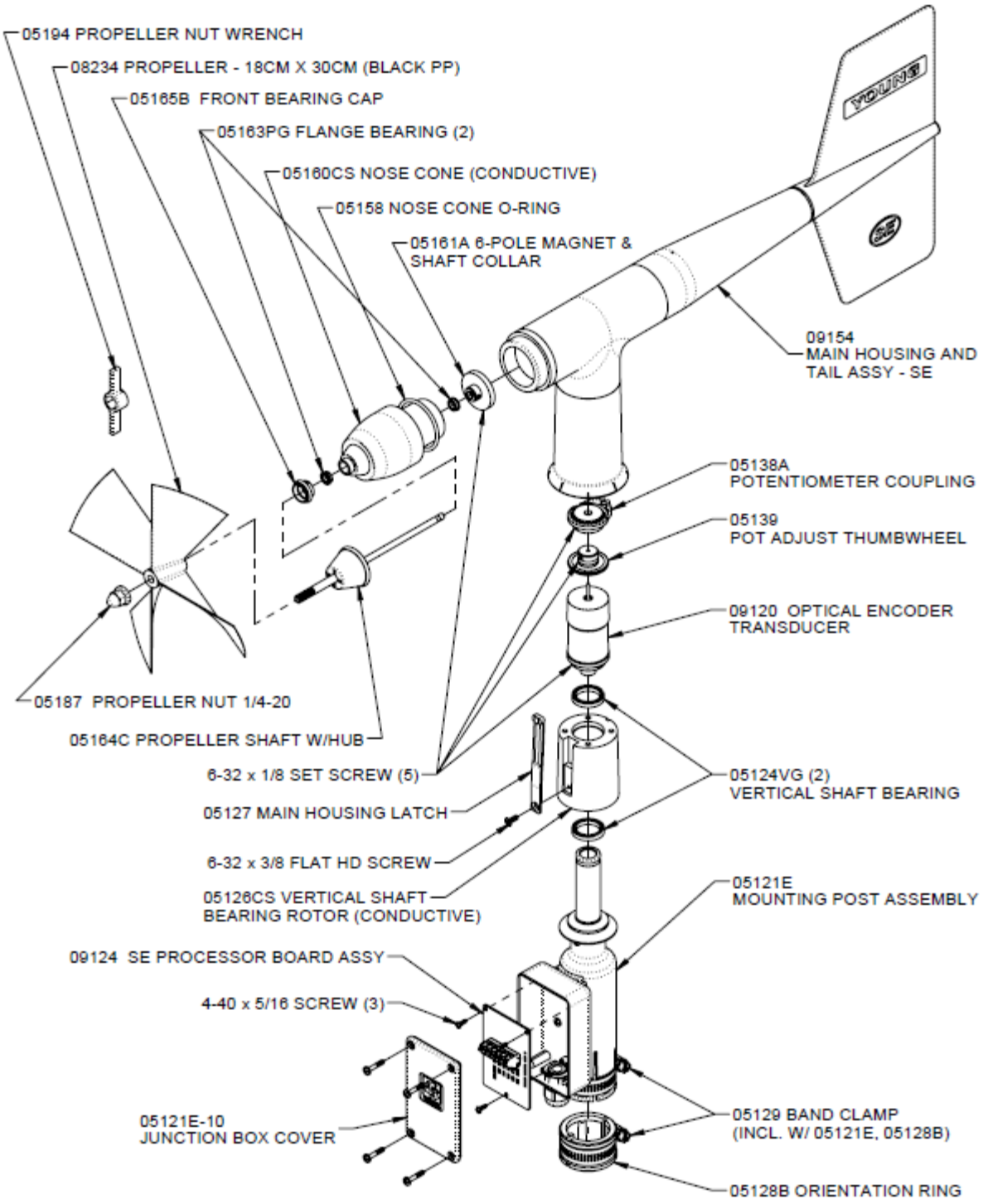
05194 PROPELLER NUT WRENCH
08234 PROPELLER - 18CM X 30CM (BLACK PP)
05165B FRONT BEARING CAP
05163PG FLANGE BEARING (2)
05160CS NOSE CONE (CONDUCTIVE)
05158 NOSE CONE O-RING
05161A 6-POLE MAGNET & SHAFT COLLAR
09154 MAIN HOUSING AND TAIL ASSY - SE
05138A POTENTIOMETER COUPLING
05139 POT ADJUST THUMBWHEEL
09120 OPTICAL ENCODER TRANSDUCER
05187 PROPELLER NUT 1/4-20
05164C PROPELLER SHAFT W/HUB
6-32 x 1/8 SET SCREW (5)
05124VG (2) VERTICAL SHAFT BEARING
05127 MAIN HOUSING LATCH
6-32 x 3/8 FLAT HD SCREW
05126CS VERTICAL SHAFT BEARING ROTOR (CONDUCTIVE)
05121E MOUNTING POST ASSEMBLY
09124 SE PROCESSOR BOARD ASSY
4-40 x 5/16 SCREW (3)
05121E-10 JUNCTION BOX COVER
05129 BAND CLAMP (INCL. W/ 05121E, 05128B)
05128B ORIENTATION RING

Baird Roof Mount Drawings

PART NO.	MAST DIAMETER	WEIGHT
B46LBK-288X10MA6-190X5	1.90"OD [48.3mm]	178 lbs. [80.7kg]
B46LBK-288X10MA6-237X5	2.37"OD [60.3mm]	183 lbs. [83.0kg]
B46LBK-288X10MA6-288X5	2.88"OD [73.0mm]	195lbs. [88.5kg]

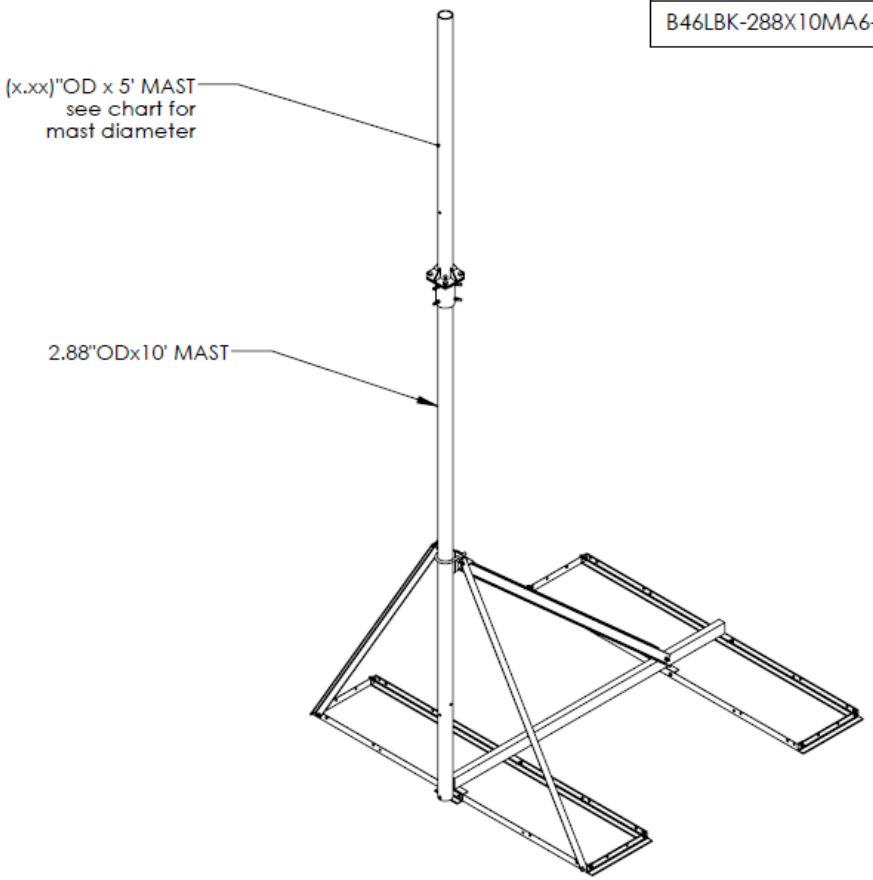

BAIRD MOUNTING SYSTEMS
WWW.BAIRDMOUNTS.COM

UNLESS OTHERWISE SPECIFIED:
DIMENSIONS ARE IN INCHES
TOLERANCES:
FRACTIONAL±
ANGULAR: MACH± BEND ±
TWO PLACE DECIMAL ±
THREE PLACE DECIMAL ±
DO NOT SCALE DRAWING

BAIRD MOUNTING SYSTEMS
WATERLOO, IA 50703
PHONE: 319-233-3561
SALES@BAIRDMOUNTS.COM

DESCRIPTION:
B4-6X6 w/ LG BRACE KIT, 15' TWO SECTION MAST, RUBBER PAD

DRAWN BY: JK	DATE: 05/12/16	
MATERIAL: STEEL	FINISH: HDG	
DWG. PURPOSE: CUSTOMER	SHEET: 1OF2	SCALE: 1:30
PART. NO.: B46LBK-288X10MA6-(000)X5		
DWG. NO.: B46LBK-288X10MA6-(000)X5		

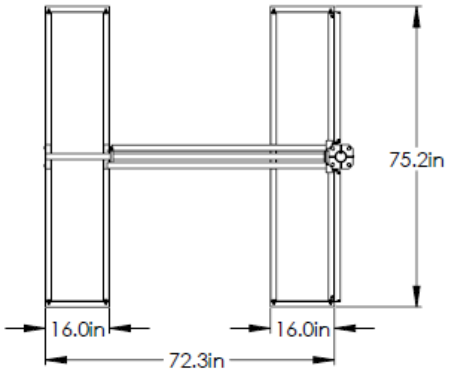

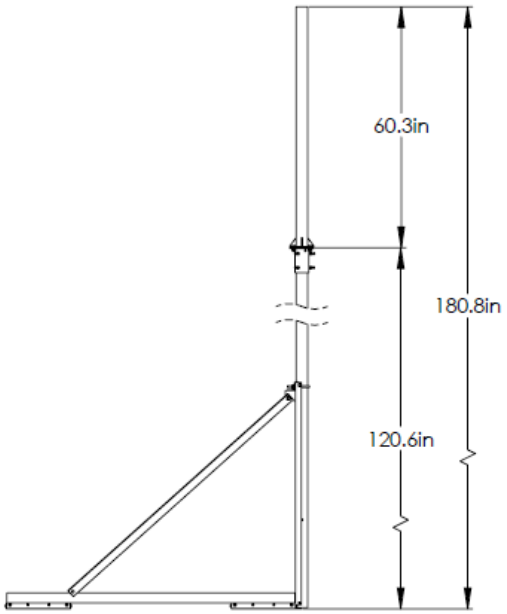

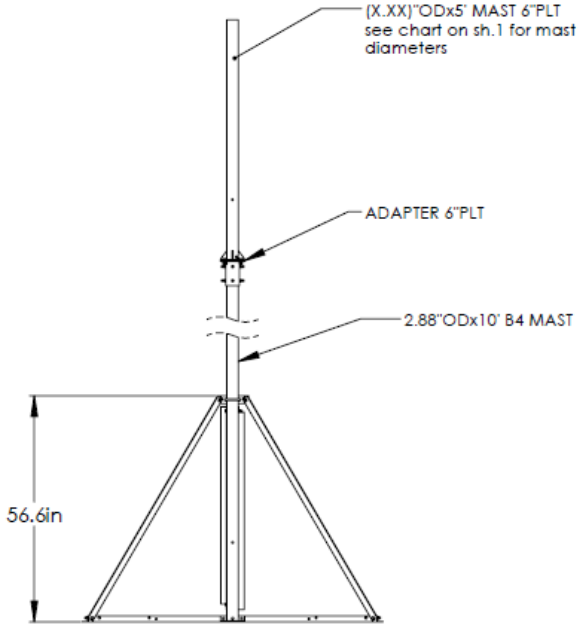

BAIRD MOUNTING SYSTEMS
WWW.BAIRDMOUNTS.COM

UNLESS OTHERWISE SPECIFIED:
DIMENSIONS ARE IN INCHES
TOLERANCES:
FRACTIONAL±
ANGULAR: MACH± BEND ±
TWO PLACE DECIMAL ±
THREE PLACE DECIMAL ±

DO NOT SCALE DRAWING

BAIRD MOUNTING SYSTEMS
WATERLOO, IA 50703
PHONE: 319-233-3561
SALES@BAIRDMOUNTS.COM

DESCRIPTION:
B4-6X6 w/ LG BRACE KIT, 2.88x15'
2 SECTION MAST, RUBBER PAD

DRAWN BY: JK	DATE: 05/12/16	
MATERIAL: STEEL	FINISH: HDG	
DWG. PURPOSE: CUSTOMER	SHEET: 2OF2	SCALE: 1:40
PART. NO.: B46LBK-288X10MA6-(000)X5		
DWG. NO.: B46LBK-288X10MA6-(000)X5		

Pipe reducers drawing

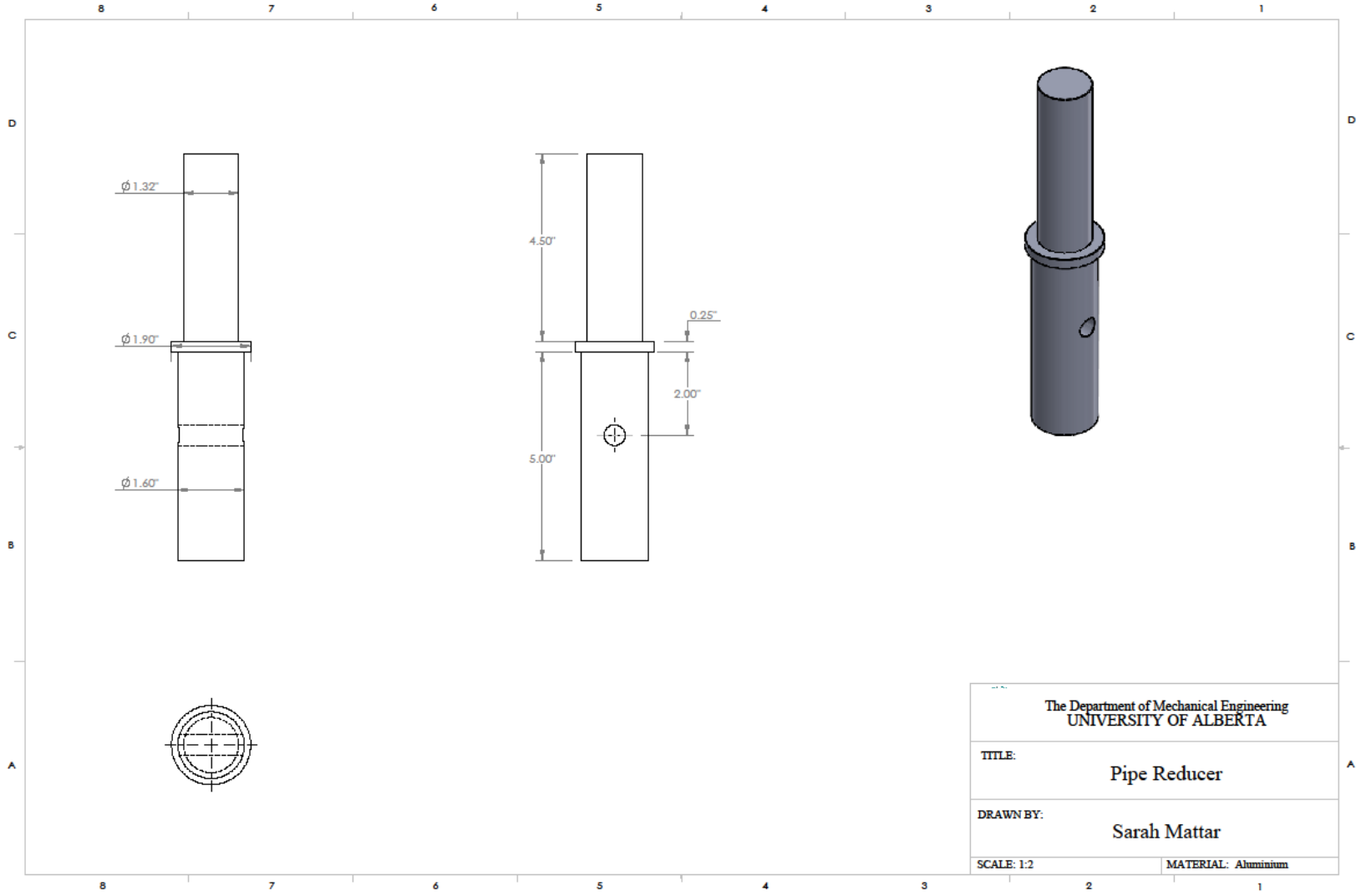

Appendix C

LabVIEW Virtual Instruments

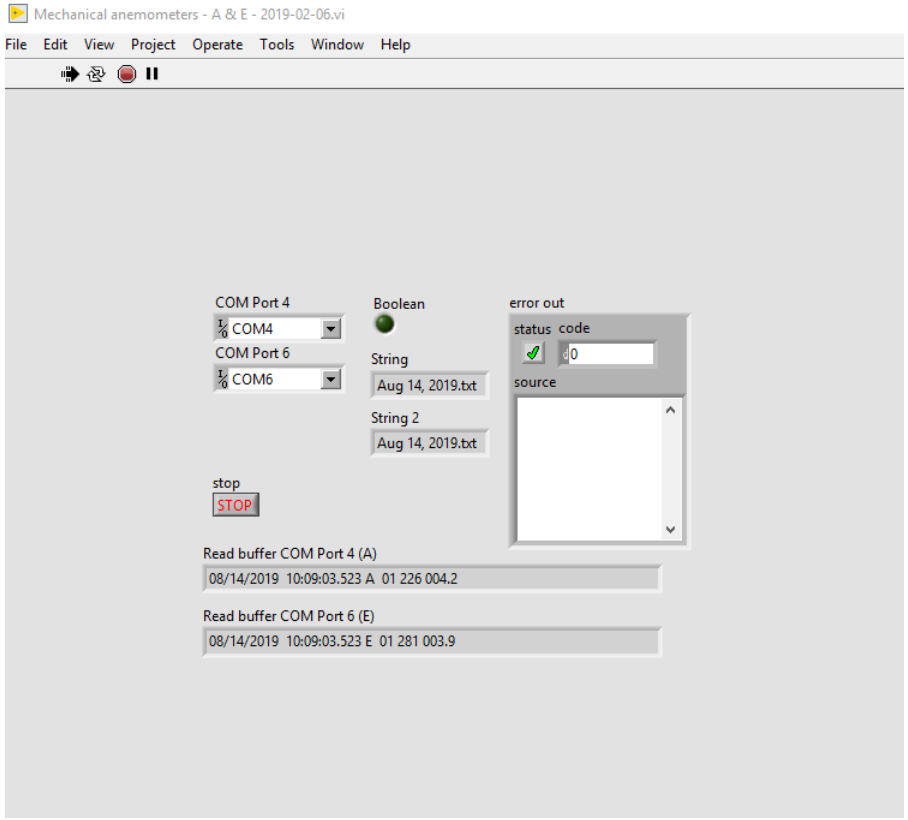

Figure C-1: Mechanical anemometers front panel.

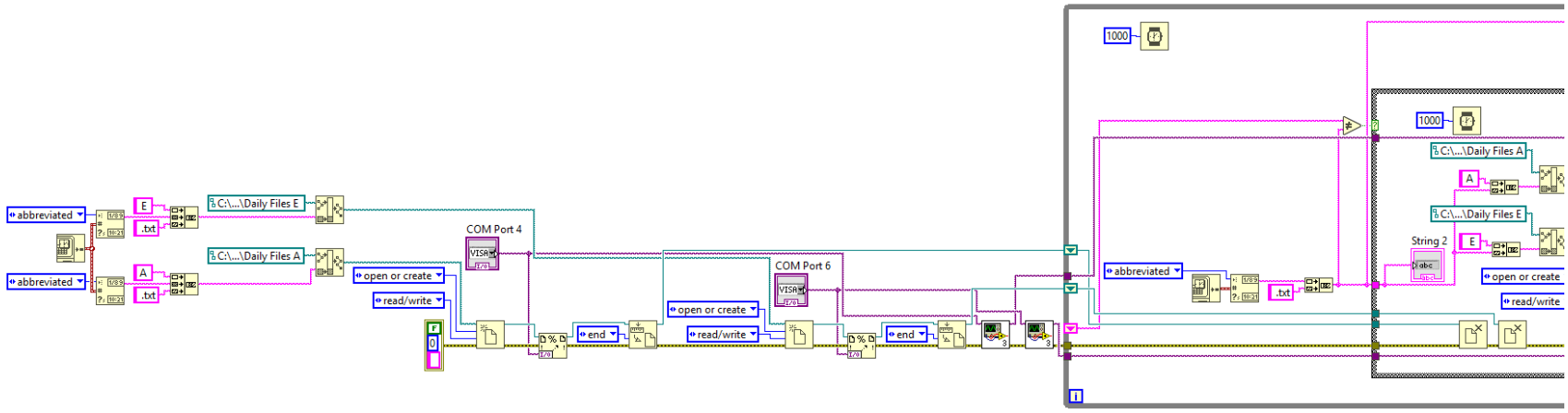

Figure C-2: LabVIEW block diagram, mechanical monitors A & E, Part 1.

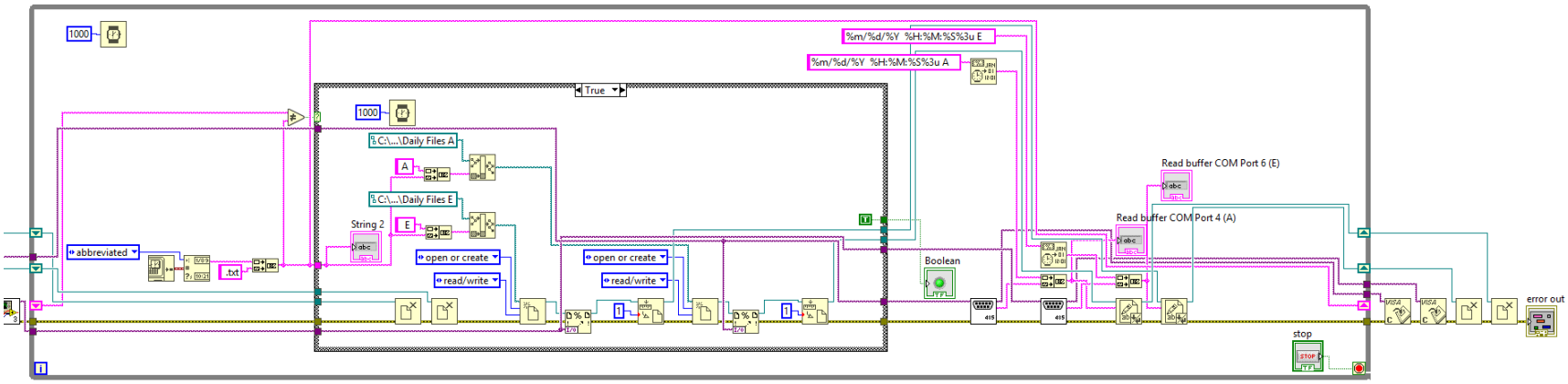

Figure C-3: LabVIEW block diagram, mechanical monitors A & E, Part 2.

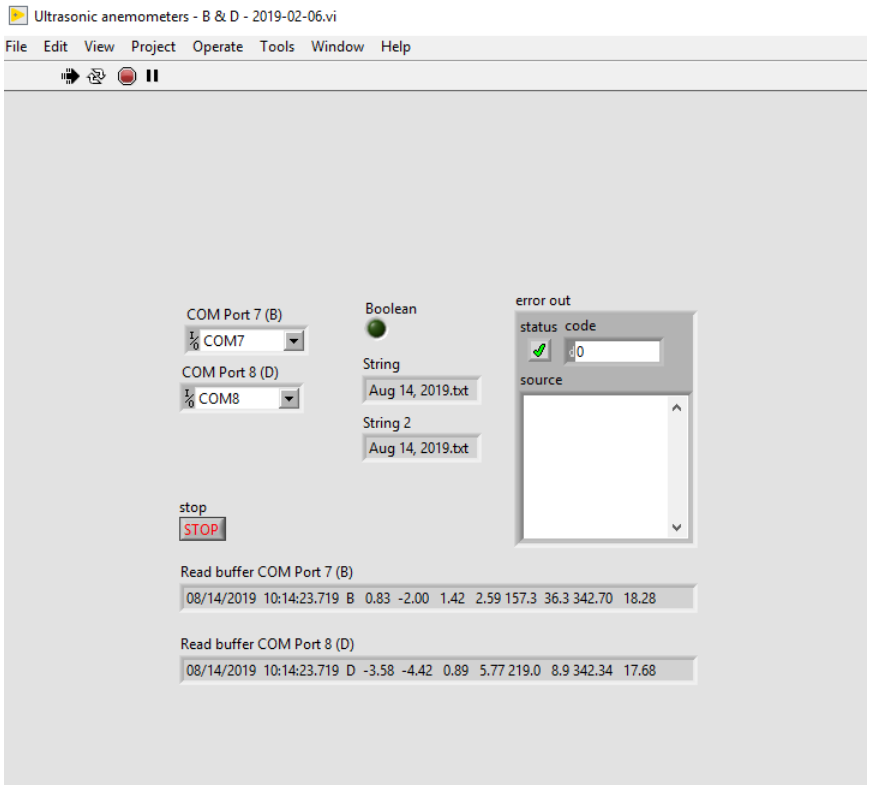

Figure C-4: Ultrasonic anemometers front panel.

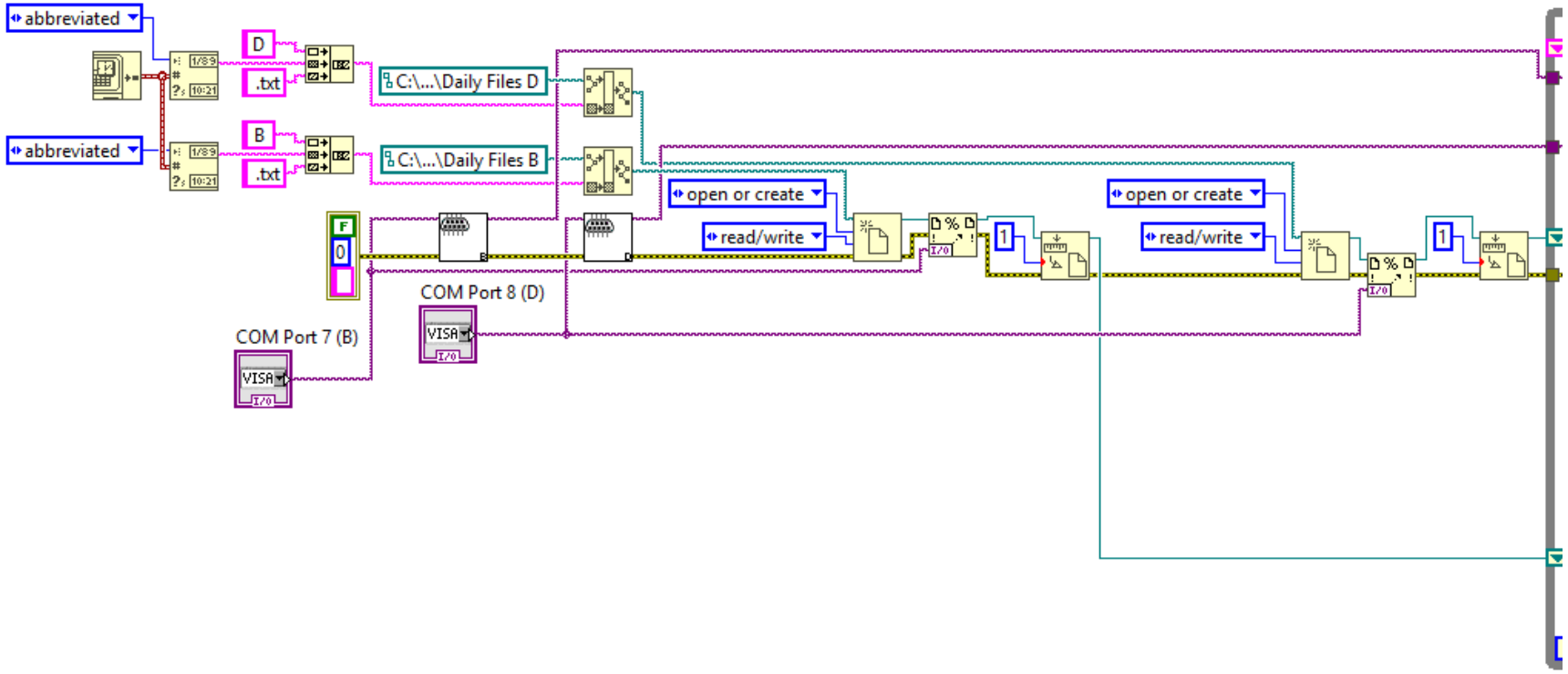

Figure C-5: LabVIEW block diagram, ultrasonic anemometers B & D, Part 1.

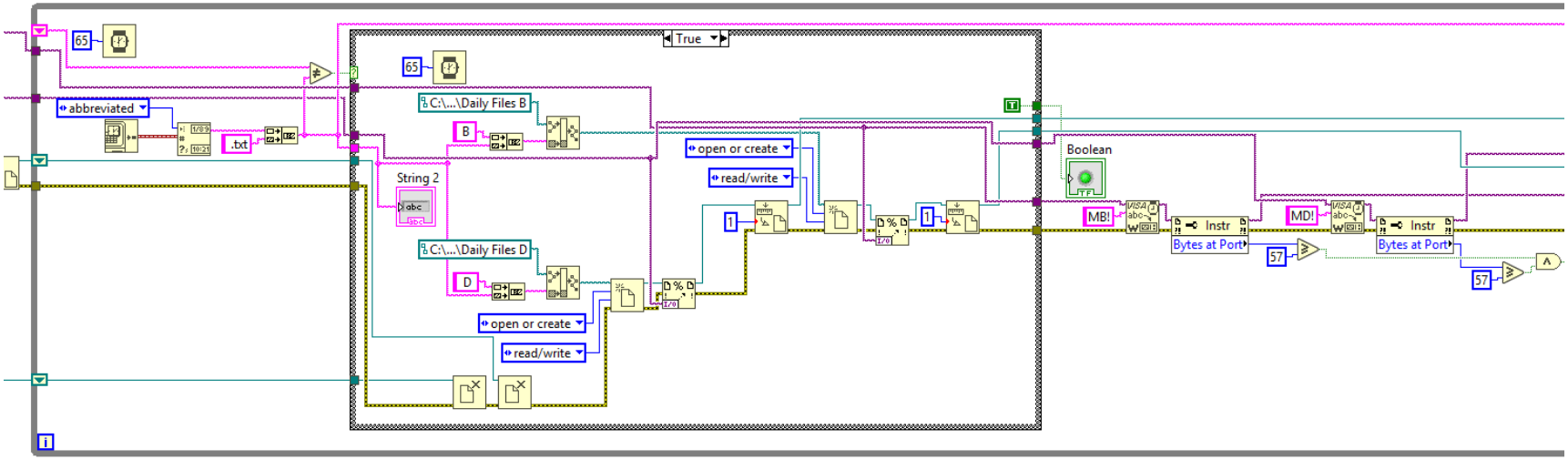

Figure C-6: LabVIEW block diagram, ultrasonic anemometers B & D, Part 2.

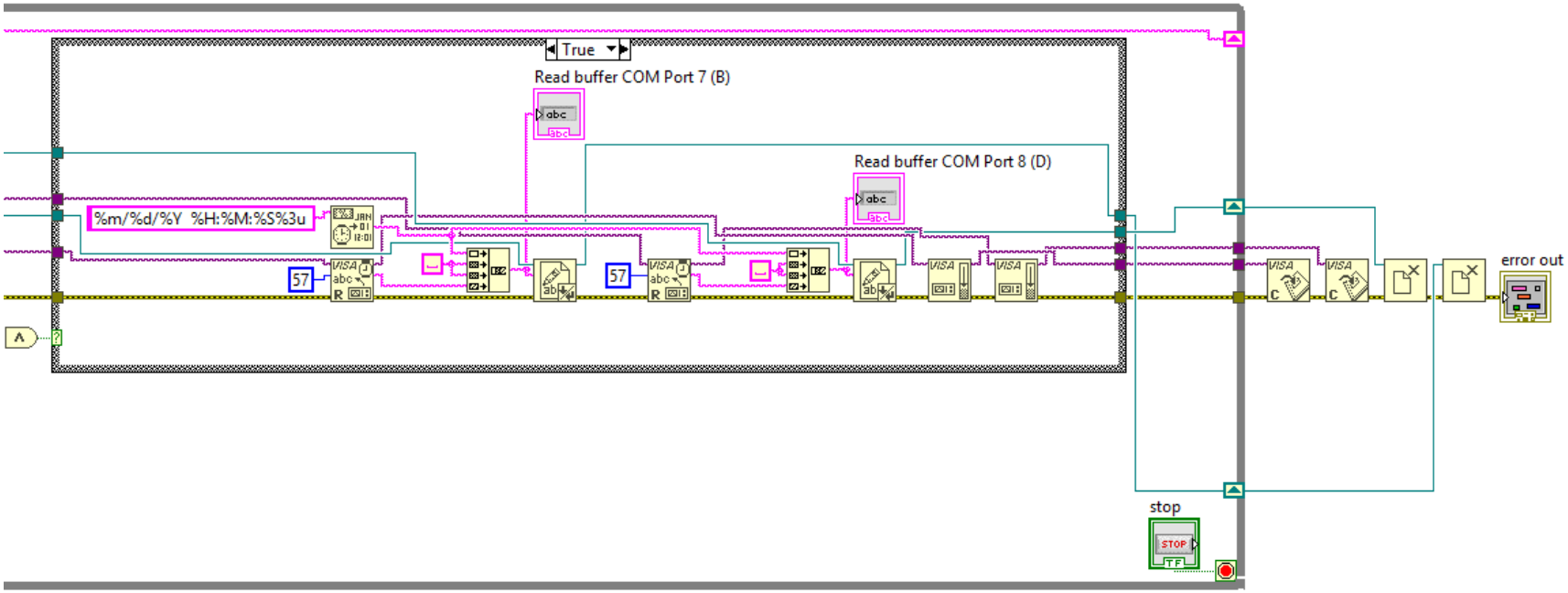

Figure C-7: LabVIEW block diagram, ultrasonic anemometers B & D, Part 3.

Appendix D

Validation Data

Table D-1: Deviations between numerical and measured results at all locations.

Location	Theta (°)	Speed (SDM) (m/s)	Speed (AM) (m/s)	CFD Speed (m/s)	Direction (SDM) (°)	Direction (AM) (°)	CFD Direction (°)	Difference Speed (SDM) (m/s)	Difference Speed (AM) (m/s)	Difference Direction (SDM) (°)	Difference Direction (AM) (°)
Free Stream Velocity 4 m/s											
A	0	4.56	5.60	3.31	8.98	6.83	348.00	-1.25	-2.29	-20.98	-18.83
A	90	3.14	3.67	4.09	114.15	112.97	98.10	0.95	0.42	-16.05	-14.87
A	180	3.17	3.23	2.94	203.97	201.20	185.00	-0.23	-0.29	-18.97	-16.20
A	270	3.17	2.99	2.31	287.19	289.34	266.00	-0.86	-0.68	-21.19	-23.34
B	0	4.15	4.70	1.24	351.53	350.57	337.00	-2.91	-3.46	-14.53	-13.57
B	90	4.02	4.22	4.09	86.29	88.93	92.20	0.07	-0.13	5.91	3.27
B	180	4.47	4.79	3.85	188.10	187.36	186.00	-0.62	-0.94	-2.10	-1.36
B	270	3.51	3.64	2.58	265.87	257.76	261.00	-0.93	-1.06	-4.87	3.24
D	90	2.67	3.10	3.42	105.14	100.15	94.20	0.75	0.32	-10.94	-5.95
D	180	5.43	5.43	3.33	194.00	190.16	175.00	-2.10	-2.10	-19.00	-15.16
D	270	3.67	4.25	2.61	282.27	280.97	266.00	-1.06	-1.64	-16.27	-14.97
Free Stream Velocity 5 m/s											
A	0	6.65	7.13	4.11	11.04	8.73	348.00	-2.54	-3.02	-23.04	-20.73
A	90	4.83	4.53	5.12	104.80	108.45	98.10	0.29	0.59	-6.70	-10.35
A	180	2.97	3.65	3.64	197.53	196.01	185.00	0.67	-0.01	-12.53	-11.01
A	270	3.04	3.40	2.87	280.21	284.95	265.00	-0.17	-0.53	-15.21	-19.95
B	0	4.77	6.17	1.62	339.95	350.40	338.00	-3.15	-4.55	-1.95	-12.40
B	90	4.93	4.95	5.13	79.94	83.19	92.30	0.20	0.18	12.36	9.11
B	180	4.67	5.81	4.8	185.85	185.51	186.00	0.13	-1.01	0.15	0.49
B	270	4.36	4.40	3.16	256.19	258.85	260.00	-1.20	-1.24	3.81	1.15

D	90	4.02	3.69	4.28	93.04	96.84	94.30	0.26	0.59	1.26	-2.54
D	180	5.65	6.18	4.18	191.07	187.34	175.00	-1.47	-2.00	-16.07	-12.34
D	270	4.76	4.74	3.28	280.94	281.70	266.00	-1.48	-1.46	-14.94	-15.70
Free Stream Velocity 6 m/s											
A	0	8.09	7.80	4.99	4.85	9.97	349.00	-3.10	-2.81	-15.85	-20.97
A	90	5.82	5.76	6.14	106.24	107.50	98.20	0.32	0.38	-8.04	-9.30
A	180	3.58	4.13	4.35	206.19	203.23	185.00	0.77	0.22	-21.19	-18.23
A	270	3.98	4.27	3.53	284.82	289.59	266.00	-0.45	-0.74	-18.82	-23.59
B	0	6.50	6.51	2.13	344.35	354.56	349.00	-4.37	-4.38	4.65	-5.56
B	90	6.33	6.21	6.14	80.12	81.17	92.40	-0.19	-0.07	12.28	11.23
B	180	5.27	6.79	5.76	190.64	190.48	186.00	0.49	-1.03	-4.64	-4.48
B	270	5.43	5.34	3.94	251.51	254.87	261.00	-1.49	-1.40	9.49	6.13
D	90	4.59	4.56	5.15	96.51	97.87	94.40	0.56	0.59	-2.11	-3.47
D	180	6.11	6.94	5.04	191.24	188.25	175.00	-1.07	-1.90	-16.24	-13.25
D	270	6.18	6.18	3.93	275.20	280.71	266.00	-2.25	-2.25	-9.20	-14.71

Table D-2: Percent error between the numerical and experimental speeds at all locations.

Location	Theta (°)	Speed (SDM) (m/s)	Speed (AM) (m/s)	CFD Speed (m/s)	% Error (SDM)	% Error (AM)
Free Stream Speed 4 m/s						
A	0	4.56	5.60	3.31	27.46	40.92
A	90	3.14	3.67	4.09	30.22	11.55
A	180	3.17	3.23	2.94	7.12	8.91
A	270	3.17	2.99	2.31	27.03	22.66
B	0	4.15	4.70	1.24	70.13	73.64
B	90	4.02	4.22	4.09	1.64	3.19

B	180	4.47	4.79	3.85	13.90	19.64
B	270	3.51	3.64	2.58	26.49	29.10
D	90	2.67	3.10	3.42	28.04	10.46
D	180	5.43	5.43	3.33	38.63	38.66
D	270	3.67	4.25	2.61	28.85	38.64
Free Stream Speed 5 m/s						
A	0	6.65	7.13	4.11	38.22	42.35
A	90	4.83	4.53	5.12	6.08	12.93
A	180	2.97	3.65	3.64	22.59	0.32
A	270	3.04	3.40	2.87	5.55	15.54
B	0	4.77	6.17	1.62	66.01	73.73
B	90	4.93	4.95	5.13	4.13	3.60
B	180	4.67	5.81	4.8	2.78	17.39
B	270	4.36	4.40	3.16	27.49	28.16
D	90	4.02	3.69	4.28	6.48	15.95
D	180	5.65	6.18	4.18	25.98	32.33
D	270	4.76	4.74	3.28	31.15	30.86
Free Stream Speed 6 m/s						
A	0	8.09	7.80	4.99	38.29	36.00
A	90	5.82	5.76	6.14	5.50	6.53
A	180	3.58	4.13	4.35	21.45	5.39
A	270	3.98	4.27	3.53	11.24	17.36
B	0	6.50	6.51	2.13	67.24	67.26
B	90	6.33	6.21	6.14	2.95	1.05
B	180	5.27	6.79	5.76	9.28	15.16
B	270	5.43	5.34	3.94	27.50	26.18
D	90	4.59	4.56	5.15	12.17	13.03
D	180	6.11	6.94	5.04	17.46	27.34
D	270	6.18	6.18	3.93	36.43	36.46

Turbulence Intensity Plots

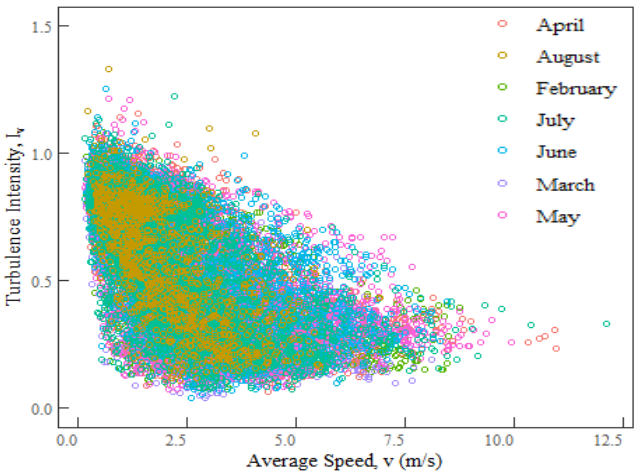

(a)

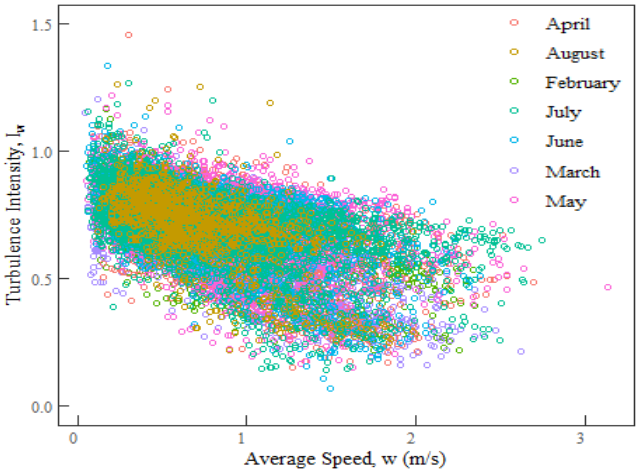

(b)

Figure D-1: 10 minute averaged turbulence intensity at location B for: (a) v −, (b) w −components.

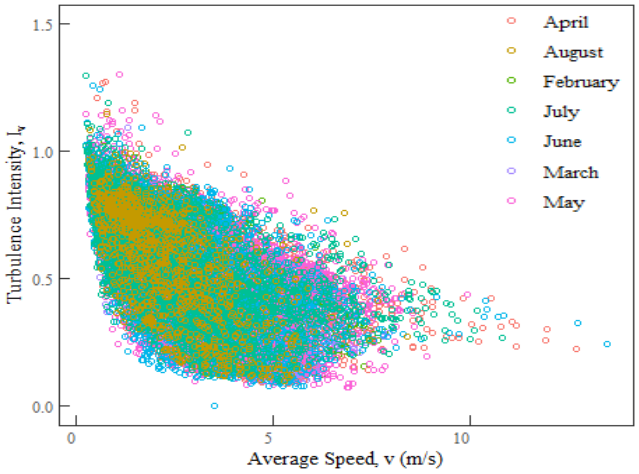

(b)

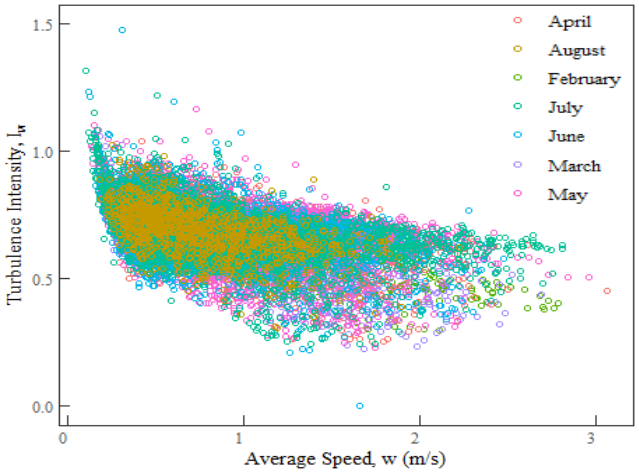

(c)

Figure D-2: 10 minute averaged turbulence intensity at location D for: (a) v −, (b) w −components.

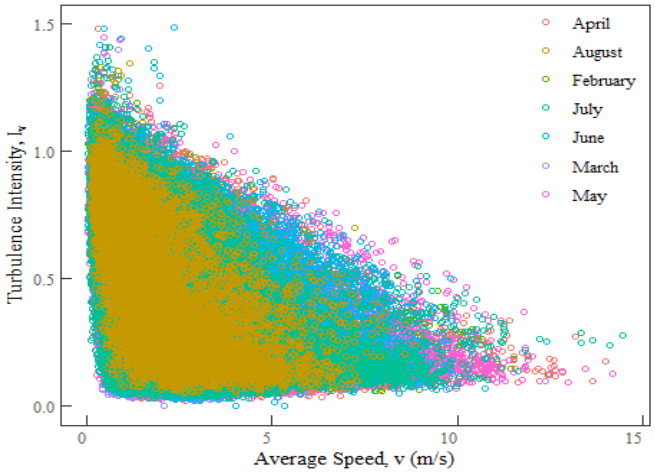

(b)

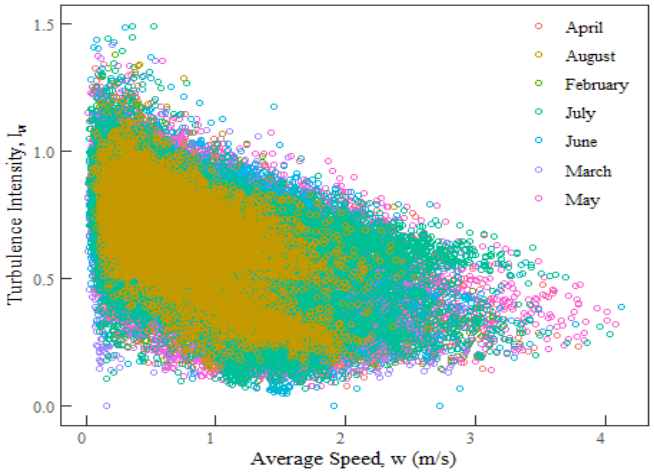

(c)

Figure D-3: 1 minute averaged turbulence intensity at location B for: (a) v −, (b) w −components.

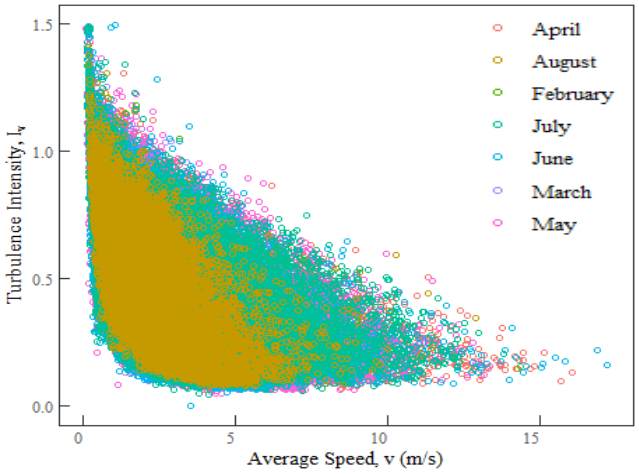

(b)

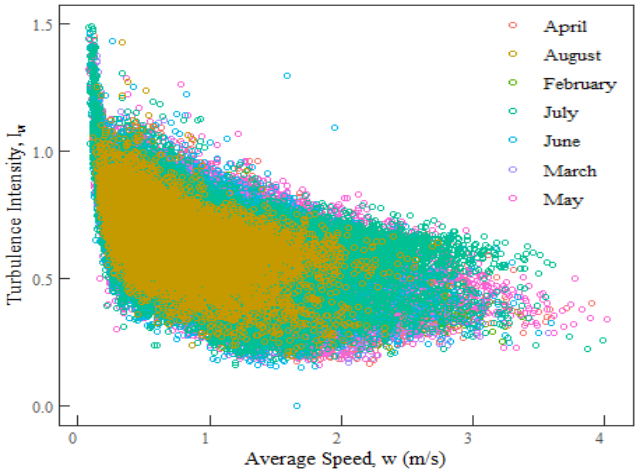

(c)

Figure D-4: 1 minute averaged turbulence intensity at location B for: (a) v −, (b) w −components.